Neutral Kaon Mixing from Lattice QCD

Ziyuan Bai

Submitted in partial fulfillment of the

requirements for the degree of

Doctor of Philosophy

in the Graduate School of Arts and Sciences

COLUMBIA UNIVERSITY

2018

Abstract

Neutral Kaon Mixing from Lattice QCD

Ziyuan Bai

In this work, we report the lattice calculation of two important quantities which emerge from second order, $K^0 - \bar{K}^0$ mixing : ΔM_K and ϵ_K. The RBC-UKQCD collaboration has performed the first calculation of ΔM_K with unphysical kinematics [1]. We now extend this calculation to near-physical and physical ensembles. In these physical or near-physical calculations, the two-pion energies are below the kaon threshold, and we have to examine the two-pion intermediate states contribution to ΔM_K, as well as the enhanced finite volume corrections arising from these two-pion intermediate states. We also report the first lattice calculation of the long-distance contribution to the indirect CP violation parameter, the ϵ_K. This calculation involves the treatment of a short-distance, ultra-violet divergence that is absent in the calculation of ΔM_K, and we will report our techniques for correcting this divergence on the lattice. In this calculation, we used unphysical quark masses on the same ensemble that we used in [1]. Therefore, rather than providing a physical result, this calculation demonstrates the technique for calculating ϵ_K, and provides an approximate understanding the size of the long-distance contributions.

Various new techniques are employed in this work, such as the use of All-Mode-Averaging (AMA), the All-to-All (A2A) propagators and the use of super-jackknife method in analyzing the data.

Contents

List of Tables **v**

List of Figures **x**

Acknowledgments **xvi**

1 Introduction **1**

2 Introduction to $K^0 - \bar{K}^0$ mixing **4**

2.1 Phenomenology of $K^0 - \bar{K}^0$ mixing and CP violation 4

2.1.1 The $K^0 - \bar{K}^0$ system 5

2.1.2 Formulae for ΔM_K and ϵ_K 7

2.2 Tree level perturbation theory calculation 10

2.3 Perturbative calculation at Next Leading Order 12

2.3.1 The conventional up quark subtraction 13

2.3.2 Our charm quark subtraction 14

2.4 Current status for the perturbative ϵ_K 16

3 $K^0 - \bar{K}^0$ mixing on the lattice **19**

3.1 Introduction of Lattice QCD 19

3.2 $\Delta S = 2$ process on the lattice 22

3.3 Operators and contractions 24

4 Measurement methods and data analysis **27**

4.1 Measurement methods 27

4.1.1 General measurement methods 27

4.1.2 Random source propagators and sparsening 30

4.1.3 Low mode deflation and All-to-All propagators 33

4.1.4 All Mode Averaging 37

4.2 Data analysis method 41

4.2.1 Fitting the two point function and meson energy 41

4.2.2 Fitting three point functions with multiple source-sink separations . . 42

4.2.3 Fitting four point functions with multiple source-sink separations . . 44

4.2.4 Jackknife and super-jackknife 46

5 ϵ_K on the lattice **52**

5.1 Lattice Evaluation of ϵ_K 55

5.2 Short distance divergence 59

5.3 Numerical results 65

5.3.1 Evaluation of X 66

5.3.2 Evaluation of Y 69

5.3.3 Fitting results for ϵ_K 71

5.4 Conclusion and outlook 83

6 ΔM_K from the $32^3 \times 64$ lattice **87**

6.1 Details of simulation 88

6.2 Results for $K_L - K_S$ mass difference 90

6.2.1 Treatment of vacuum and η state 90

6.2.2 Two-pion contribution to ΔM_K 93

6.2.3 The single pion contribution 94
6.2.4 $K_L - K_S$ mass difference 94
6.3 Finite volume corrections to ΔM_K 101

7 ΔM_K from the $64^3 \times 128$ lattice **103**
7.1 Details of simulation 103
7.2 Results and error breakdown 106
7.2.1 Meson state and three point functions 106
7.2.2 Results for ΔM_K 109
7.2.3 m_c dependence 111
7.2.4 Finite volume corrections 112
7.3 Conclusion 117

8 Conclusion **118**

Bibliography **120**

Appendix A All diagrams calculated on the lattice **123**
A.1 All four points diagrams 123
A.2 All three point diagrams 132
A.3 All K to $\pi\pi$ diagrams 135
A.4 All two point dagrams 136
A.5 All $\pi\pi$ scattering diagrams 137

Appendix B Contraction details **138**
B.1 Two point contractions 138
B.2 $\pi\pi$ scattering contractions 139
B.3 Three point contractions 139
B.4 $K \to \pi\pi$ contractions 145

B.5 Four point contractions 146
B.5.1 ΔM_K contractions 146
B.5.2 ϵ_K contractions 148

Appendix C Operator Mixing and the calculate the lattice Wilson coefficients with NPR **150**

C.1 NPR for ϵ_K on the 24^3 lattice 150
C.2 NPR on the 64^3 lattice 154
C.3 NPR on the 32^3 DSDR lattice 155

Appendix D Tests of the DWF formulation for heavy quarks **157**

D.1 Dispersion relations 157
D.2 Charmed meson masses 159
D.3 Pseudo-scalar decay constant 161

List of Tables

2.1 The value for the QCD correction terms η_i, calculated in NLO and NNLO. . 17

2.2 The value for ϵ_K from different input method for V_{cb}. We have also shown the deviation from the experimental value. 18

4.1 Test for sparsening on the 32^3 lattice. We have computed the type 3 diagrams contribution to ΔM_K, which is less noisy. We have separated the contribution from the four different combinations of $Q_i Q_j$. We have done the measurements 5 times, each time with 64 random hits, and the error is calculated based on these 5 measurements. 550 eigenvectors are used in the A2A propagators. . . 36

4.2 Test for sparsening on the 64^3 lattice. We have computed the both the 3 diagrams and the type 4 diagrams contribution to ΔM_K. We separated the results by the parity conserving part and the parity violating part. We have done the measurements 6 times, each time with 24 random hits, and the error is calculated based on these 6 measurements. 2000 eigenvectors are used in the A2A propagators. Other aspects and the conclusions are the same as in Table 4.1. 36

4.3 CG iteration number with different stopping conditions on the 32^3 lattice. For the light quark, we have used low mode deflation with 550 eigenvectors to accelerate the CG. 38

4.4 CG iteration number with different stopping conditions on the 64^3 lattice. For the light quark, we have used low mode deflation with 2000 eigenvectors to accelerate the CG. 38

5.1 Input parameters for the evaluation of Wilson coefficients. 66

5.2 The value for α_s for different energy scale and Λ_{QCD} with different active flavors. 66

5.3 $X^{i,j}$ for different space-time cutoff, with operator combination $Q_{i,j}$. The external momentum has scale $\mu = 1.41$ GeV. 67

5.4 Values of X for different momentum scales μ. The results have been multiplied by the Wilson coefficients. We have dropped statistical errors because they're less than 1%. 68

5.5 Numerical value for $\Delta Y(\mu_{RI})$, at the same scale we evaluate $X(\mu_{RI})$. 71

5.6 $X^{i,j}$ calculated using the external momentum scale $\mu = 2.11$ GeV, in lattice units. In the calculation of $X^{i,j}$, we only calculate $i < j$, since he value for $X^{i,j}$ with $i > j$ is the same and included in these coefficients. 72

5.7 Imaginary part of $M_{\bar{0}0}^{ut}$, before the subtraction of the short distance divergent part, with all the Wilson coefficients multiplied. We have included only type 1 and type 2 diagrams. All numbers are in units of 10^{-15} MeV. 72

5.8 Imaginary part of $M_{\bar{0}0}^{ut}$, after the subtraction of the short-distance, divergent part, with all the Wilson coefficients multiplied. We have included only type 1 and type 2 diagrams. All numbers are in units of 10^{-15} MeV. 72

5.9 Imaginary part of $M_{\bar{0}0}^{ut}$, after the subtraction of the short distance divergent part, and with all the Wilson coefficients multiplied. We have included all 5 types of diagrams. All numbers are in units of 10^{-15} MeV. 74

5.10 Contributions to Im $M_{\overline{00}}^{ut}$, in units of 10^{-15} MeV. The first column is before we remove the short distance divergence from our lattice result, and only includes the type 1 & 2 diagrams. The second column is after the removal of the short distance divergence. The third column is after removal of the divergence and includes all five types of diagrams. The last column is our final long distance correction to Im $M_{\overline{00}}^{ut}$, with the perturbative $RI \to \overline{MS}$ part included. We have chosen $\mu_{RI} = 2.11$ GeV. 75

5.11 The contributions to Im $M_{\overline{00}}^{ut}$ (in units of 10^{-15} MeV), and the corresponding contribution to ϵ_K as we vary μ_{RI}. The second column presents our results from the lattice calculation, after the removal of the short distance divergence. The third column is the perturbative part that involves ΔY. The fourth column is our final long distance correction to Im $M_{\overline{00}}^{ut}$, which is the sum of the previous two columns. The last column is the corresponding contribution to ϵ_K, in units of 10^{-3}. We have chosen to use B_K at $\mu = 2.11$ GeV. 76

5.12 Results similar to those in Table 5.11, but with only type 1 and 2 diagrams. 76

5.13 The different short distance contribution to ϵ_K. I have used a perturbative calculation in NLO and using the CKM parameters from the angle-only-fit (AOF)[2], exclusive V_{cb} [3]. The last two columns are our long distance correction to ϵ_K and the contribution from ξ quoted from the $K \to \pi\pi$ measurement in [4]. I have dropped the statistical error from the short distance calculation. 85

5.14 Input parameters used in short distance calculation. 86

6.1 The residual mass m_{res} for different choice of L_s with Möbius fermions. . . . 89

6.2 Effective masses for the pion, kaon, η, and two-pion states, in units of MeV. 92

6.3 The subtraction coefficients c_s, c_p, used for the operators Q_1 and Q_2 separately. 92

6.4 Kaon to two-pion matrix elements in lattice units. 94

6.5 The kaon to single pion matrix element $\langle\pi|Q_{1,2}|K\rangle$ (not including $\bar{s}d$) and the matrix element for the scalar operator $\langle\pi|\bar{s}d|K\rangle$, in lattice units. 94

6.6 ΔM_K and the individual contributions from different operator combinations, in the units of 10^{-12} MeV. We have varied the starting point of our fitting range between 6 and 8 time units. All numbers are multiplied by the appropriate Wilson coefficient computed in the (γ_μ, γ_μ) scheme. 95

6.7 Individual physical contribution to ΔM_K from the single-pion state and the two-pion state, in units of 10^{-12} MeV. The subtraction of $\bar{s}d$ and $\bar{s}\gamma_5 d$ is included. 95

6.8 Fitting results if we only include type 1/2 diagrams or type 3/4 diagrams for different m_c. $T_{min} = 8$ is used. 96

6.9 The $I = 0$ $\pi\pi$ contribution to ΔM_K, and the factors entering the finite volume correction. The last term is the finite volume correction to the $K_L - K_S$ mass difference ΔM_K^{FV}, in units of $10^{-12} MeV$. 102

7.1 Fitting results for meson mass and $\pi - \pi$ energy in both lattice units (top row) and MeV (bottom row). 107

7.2 The bare lattice results for K^0 to π matrix element and the K^0 to vacuum matrix element, without subtracting the $\bar{s}d$ operator. 108

7.3 The subtraction coefficients for the scalar and pseudo-scalar operator. 108

7.4 The bare lattice results for K to $\pi\pi$ matrix element for Isospin 0 and 2. The I=2 matrix element for Q_1 and Q_2 are the same because they are from the same three point diagrams. 109

7.5 Results for ΔM_K from different fitting method (in units of $10^{-12} MeV$). The pair of numbers separated by a colon in the first column gives the fitting range. 110

7.6 Contribution to ΔM_K from type 3 and type 4 diagrams (in units of $10^{-12}MeV$), with the error from the AMA correction or without the error from the AMA correction. 110

7.7 The result for ΔM_K and the type 4 diagrams contribution from the new method of using multiple source-sink separation and the old method using a single source-sink separation. In units of $10^{-12}MeV$. 111

7.8 Results for ΔM_K calculated from different charm quark masses. We used un-correlated fit with the fitting range 10:20. The charm quark masses are bare lattice numbers and the ΔM_K are in units of 10^{-12} MeV. 111

7.9 The jackknifed differences between ΔM_K calculated from different charm quark masses and ΔM_K from $m_c = 0.25$. We used un-correlated fit with the fitting range 10:20. The charm quark masses are bare lattice numbers and the ΔM_K are in units of 10^{-12} MeV. 112

7.10 The $\pi\pi_{I=0}$ contribution to ΔM_K, and the terms determining the corresponding finite volume correction. The last term is the finite volume correction to the $K_L - K_S$ mass difference $\Delta M_K(FV)$, in units of $10^{-12}MeV$. 112

C.1 The $\overline{MS}$ Wilson Coefficients, $RI/SMOM \to \overline{MS}$ matching matrix Δr, $lat \to RI$ matching matrix Z obtained using Z_q calculated in different schemes, and finally the lattice Wilson coefficient at the scale 3.0GeV. 1st row: $(\gamma_\mu, \not{q})$ scheme, 2nd row: (γ_μ, γ_μ). We do not show a statistical error because all are less than 1%. 156

List of Figures

2.1 Two types of diagrams contributing to the $K^0 - \bar{K}^0$ mixing process. On the left is the box diagram and on the right is the disconnected diagram. 10

3.1 Example diagram for $K^0 - \bar{K^0}$ mixing. The two weak Hamiltonians are integrated over the time interval $[t_a, t_b]$. The internal quark lines should be u-type quark, which in our 4-flavor theory can be either up or charm. 23

3.2 Five types of four point diagrams to calculate on the lattice. 26

4.1 Type 3 and 4 (only parity conserving part) diagrams using random volume source compared to A2A propagators with 550 eigenvectors. Both with 60 random hits, an operators Q_1Q_1 or Q_2Q_2 at two vertices. On the top: type 3 diagrams, on the bottom: type 4 diagrams. 39

4.2 The integrated correlator for ΔM_K with different operator combinations. We plot the result from 6 configurations. The blue line is the correlator with a $1e-8$ stopping condition, and the red line is the difference between $1e-8$ and $1e-4$ stopping conditions. 40

5.1 Type 1 and type 2 four point diagrams. The label c means a current-current operator, and p means a penguin operator. 58

5.2 Type 3 and type 4 four point diagrams. The label c means a current-current operator, and p means a penguin operator. 59

5.3 Type 5 four point diagrams. They have a current-current operator ar one vertex, and the other vertex must come from either a $(\bar{s}d)_{V-A}(\bar{d}d)_{V\pm A}$ operator or a $(\bar{s}d)_{V-A}(\bar{s}s)_{V\pm A}$ operator. 59
5.4 On the left: example diagram in ΔM_K calculation. On the right: Example diagram in ϵ_K calculation. 60
5.5 Illustration of the calculation of ΔY. 62
5.6 Some example diagrams that determine the short distance correction. The diagram on the left has the operator O_{LL}, and the two diagrams on the right have two $\Delta S = 1$ operators. Γ_μ stands for $\gamma_\mu(1-\gamma_5)$ and V+/-A stands for $\gamma_\mu(1\pm\gamma_5)$. The right hand vertex comes from operator $Q_{5,6}$. 64
5.7 The fitted results for $X(\mu_{RI})$, as a function of momentum scale μ from 3 gauge configurations. An uncorrelated logarithm fit is performed. 68
5.8 Integrated correlator including only type 1 and type 2 diagrams. We shown the result before and after we subtract the single pion state, and also after we subtracted the short distance part. The Wilson coefficients are not included. 78
5.9 Integrated correlator including only type 1 and type 2 diagrams. We shown the result before and after we subtract the single pion state, and also after we subtracted the short distance part. The Wilson coefficients are not included. 79
5.10 Integrated correlator including all five types of diagrams. We use a correlated fit with fitting range $T = 10 : 16$. The Wilson coefficients are not included. . 80
5.11 Integrated correlator including all five types of diagrams. We use a correlated fit with fitting range $T = 10 : 16$. The Wilson coefficients are not included. . 81
5.12 $\mathrm{Im}\, M_{\bar{0}0}^{ut,RI}$, $\mathrm{Im}\, M_{\bar{0}0}^{ut,RI\to\overline{MS}}$ and $\mathrm{Im}\, M_{\bar{0}0}^{ut,ld\,corr}$ for different μ_{RI}, in units of 10^{-15} MeV. On the left, all types of diagrams are included. On the right, only type 1 and type 2 diagrams are included. 82
5.13 Scale dependence of $\eta_3' S_0'(x_c, x_t)$, calculated using the four-flavor theory. . . . 85

6.1 Four types of four-point diagrams used in the calculation of the integrated correlator. 89
6.2 The Four types of diagrams which enter the calculation of $\langle\pi\pi|H_W|K\rangle$. . . . 90
6.3 The effective mass for the two-pion states with $I = 0$ (on the left) and $I = 2$ (on the right). 91
6.4 The effective mass for the η states. 92
6.5 The fitting of the ratio $\frac{\langle\eta|Q_i|K^0\rangle}{\langle\eta|\bar{s}d|K^0\rangle}$, for operators Q_1 and Q_2 separately and charm mass 750 MeV. We used the fitting method in Sec. 4.2.2, and the horizontal axis is separation δ between the operator and the η sink. 93
6.6 The kaon to two-pion subtraction diagrams $\langle\pi\pi|\bar{s}\gamma_5 d|K\rangle$. 93
6.7 Fitting plateaus for the kaon to two-pion matrix element, for the operators Q_1 and Q_2 separately and charm mass 750 MeV. The two-pion state can have isospin either 0 or 2. The x-axis is the separation between the weak operator $Q_{1,2}$ and the sink. We have included the χ^2 per degree of freedom of the fitting, and its statistical error. The horizontal dashed lines show the fitting range, the central value and errors obtained from the fit. 97
6.8 Plots of the integrated correlator and the effective slope plot for the three operator products Q_1Q_11, Q_1Q_2 and Q_2Q_2 The upper panel is from $m_c = 0.38$ (750 Mev), and the lower lanel is from $m_c = 0.3$ (592 MeV). $T_{min} = 8$ is used to obtain the fits shown. 98
6.9 Plots for the integrated correlator and the effective slope, for type 1/2 diagrams only. In the upper panel: $m_c = 750$ MeV, while in the lower panel: $m_c = 592$ MeV. $T_{min} = 8$ is used. 99
6.10 Integrated correlator and the effective slope, for type 3/4 diagrams only. The upper panel: $m_c = 750$ MeV, the lower paner: $m_c = 592$ MeV. $T_{min} = 8$ is used. 100

7.1 The effective mass plots for the $I = 0$ and $I = 2$ $\pi\pi$ states. On the left: I = 0, on the right, I = 2. The plots are symmetric about $T = 58$ since there's a separation of 6 between the two pions in the source and sink. 107

7.2 The effective mass plot for η states. It is dominated by disconnected diagrams and therefore has large statistical errors. 107

7.3 The $\langle\pi\pi|Q_i|K\rangle$ matrix element for various $\pi\pi$-operator separation δ. On the left: Q_1, on the right, Q_2. 113

7.4 $\frac{\langle\eta|Q_i|K\rangle}{\langle\eta|\bar{s}d|K\rangle}$ for various η-operator separations δ. On the left: Q_1, on the right, Q_2. 114

7.5 The fitting results for the integrated four point correlator. From left to right, top to bottom: All diagrams included, only type 1&2 diagrams included, and only type 3&4 diagrams included. From un-correlated fit using the range using the range 10:20. 115

7.6 The fitting results for the integrated four point correlator. From left to right, top to bottom: All diagrams included, only type 1&2 diagrams included, and only type 3&4 diagrams included. From correlated fit using the range 16:22. 116

A.1 Contractions for type 1 four point diagrams, all vertices have a V-A structure if no explicit notation is shown. Each diagram represents two different contractions depending on the vertex being marked is a $V - A$ or $V + A$ vertex. The dashed lines represent the contraction of color. 124

A.2 Contractions for type 2 four point diagrams, all vertex are V-A structure if no explicit notation is shown. Each diagram represents two different contractions depending on the vertex being marked is a $V - A$ or $V + A$ vertex. The dashed lines represent the contraction of color. 125

A.3 Contractions for type 3 four point diagrams, all vertex are V-A structure if no explicit notation is shown. Each diagram represents two different contractions depending on the vertex being marked is a $V-A$ or $V+A$ vertex. The dashed lines represent the contraction of color. 126
A.4 contractions for type 4 four point diagrams, all vertex are V-A structure if has no explicit notation. Each diagram represents two different contractions depending on the vertex being marked is a $V-A$ or $V+A$ vertex. The dashed lines represent the contraction of color. 127
A.5 Contractions for type 3 subtraction four point diagrams. Each diagram represents two different contractions depending on the vertex being marked is a $V-A$ or $V+A$ vertex. The dashed lines represent the contraction of color. 128
A.6 contractions for type 4 subtraction four point diagrams. Each diagram represents two different contractions depending on the vertex being marked is a $V-A$ or $V+A$ vertex. The dashed lines represent the contraction of color. 129
A.7 Contractions for type 5 four point diagrams, all vertex are V-A structure no explicit notation is shown. Each diagram represents two different contractions depending on the vertex being marked is a $V-A$ or $V+A$ vertex. The dashed lines represent the contraction of color. 130
A.8 Contractions for type 5 subtraction diagrams. Each diagram represents two different contractions depending on the vertex being marked is a $V-A$ or $V+A$ vertex. The dashed lines represent the contraction of color. 131
A.9 3 point diagrams. The dashed lines represent contraction of colors. Each diagram represents two different contractions depending on the vertex being marked is a $V-A$ or $V+A$ vertex. 132

A.10 3 point diagrams(continued). The dashed lines represent contraction of color. Each diagram represents two different contractions depending on the vertex being marked is a $V-A$ or $V+A$ vertex. 133
A.11 3 point diagrams(continued). The dashed lines represent contraction of colors. Each diagram represents two different contractions depending on the vertex being marked is a $V-A$ or $V+A$ vertex. 134
A.12 Contractions for $K \to \pi\pi$ diagrams. Only Q_1 and Q_2 are included. The vertex is a $V-A$ vertex. 135
A.13 Contractions for $K \to \pi\pi$ diagrams, continued. Only Q_1 and Q_2 are included. The vertex is a $V-A$ vertex. 136
A.14 2 point diagrams 137
A.15 $D(t)$,$C(t)$,$R(t)$,$V(t)$ for two pions 137

D.1 The dispersion relation for different charm quark masses and momenta. The x axis is the energy scale of the momenta p.This calculation is performed on the 32^3 Iwasaki lattice with $1/a = 2.38$ GeV. 10 gauge configurations are used. 158
D.2 The dispersion relation for different charm quark masses and momenta. The x axis is the energy scale of the momenta p. This calculation is performed on the 32^3 DSDR lattice with $1/a = 1.36$ GeV. 13 gauge configurations are used. 159
D.3 Results for m_{D_s} for different values of m_c. 18 configurations were used. The first point corresponds to the kaon. 160
D.4 Results for m_{η_c} for different m_c. 18 configurations were used. The first point corresponds to the pion and we note the pion is unphysically heavy on this ensemble. 160
D.5 Results for f_{D_s} for different values of m_c. The first point correspond to the kaon. 18 configurations were used. 161

D.6 Φ for different m_c. 18 configuration was used. Note physical, monotonic dependence on $\frac{1}{m_{\eta_c}}$ is seen in the vicinity of the physical value for $\frac{1}{m_{\eta_c}} = 0.336.162$

ACKNOWLEDGMENTS

I would like first thank my advisor Prof. Norman Christ for his continuous support and guidance through out my five years as a graduate student at Columbia. I benifited a lot from the weekly discussions with him are very impressed by his devotion to work and physics. I also would like to thank Prof. Bob Mawhinney for his guidance and helpful discussion. I would like to thank our collaborators at BNL, especially Chulwoo Jung and Christoph Lehner. Some important part of my projects are only possible with their software support. I'd also like to thank Prof. Chris Sachrajda, Prof Xu Feng and Amarjit Soni for theri helpful discussions. I'd like to thank my collegues: Prof. Luchang Jin,Yuran Chen, Zizhou Gong, Crhis Kelly, Jasper Lin, David Murphy, Greg McGlynn, Jiqun Tu, Bigeng Wang, Tianle Wang, Jianglei Yu, Jiechen Xu and Daiqian Zhang.

I espeically thank my family, including my parents and my girlfriend Tingting Wang for their kindness support and caring during and after my years at Columbia. It's my great pleasure to spend time with them. I also learned a lot from them in many aspects.

Chapter 1

Introduction

The Standard Model of particle physics is a successful theory describing the interactions of elementary particles. Quantum electrodynamics (QED), which is the theory describing electro-magnetic interactions, has lead to great success in predicting the anomalous magnetic dipole moment for electrons $(g-2)$, with an agreement with experiment up to precision of 10^{-9}. We believe we have fully understood the EM interactions of QED because of its simplicity (a single coupling constant of size 1/137). Quantum chromadynamics (QCD), which is the theory describing the strong interactions, is discovered about 40 years after QED. It took a few decades to fully establish the theory of QCD because of its complexity. It is a non-abelian SU(3) gauge theory where gluons can interact with each other, and its strong coupling α_s at low energy makes it very difficult for perturbation theory calculation to provide precise results at low energies. Various analytic QCD works are based on approximations such as symmetry analysis, instead of performing a first principle calculation. One of these examples is chiral perturbation theory, which is an effective field theory based on the approximate chiral symmetry of QCD.

The weak interaction is the least understood part of the Standard Model. Since many weak interaction processes involve mesons and baryons, the weak interaction is mixed with QCD interaction in complicated ways. The weak interaction is very interesting because of the

possibility of discovering new physics: It has built-in parity (P) violation as well as charge-parity (CP) violation, and 16 out of the 19 parameters in the Standard Model are closely related to weak interaction. Extensive tests have been done to find discrepancies in the Standard Model predictions for the weak interactions, since any discrepancy will imply the existence of new physics. Some promising example are the direct and indirect CP violation parameters ϵ' and ϵ. They have very small sizes and are related to the CP violating phase of the CKM matrix and hence are sensitive to new physics. Both these parameters have precise experimental values, making them good tests for the Standard Model.

The development of Lattice QCD provides a reliable way to calculate QCD interactions based on the Standard Model. Since the strong coupling α_s becomes large (on the order of one) at an energy scale close to Λ_{QCD}, perturbation theory is no longer effective. The Lattice QCD method solves QCD problems non-perturbatively. Recent developments in computer power as well as computer algorithms make lattice QCD very effective to determine various physical quantities. We are now able to perform a physical calculation for quantities such as the $K_L - K_S$ mass difference ΔM_K, instead of using unphysical kinematics and performing extrapolations. In this work, we report the calculation of two quantities emerging from neutral kaon mixing based on first principles: the $K_L - K_S$ mass difference ΔM_K, and the indirect CP violation parameter ϵ_K.

The mass difference ΔM_K has been observed in the K^0 oscillation experiments and has an precise experimental value of $3.483(6) \times 10^{-12}$ MeV. However, the Standard Model prediction of ΔM_K hasn't been precisely worked out since it is highly non-perturbative. The perturbation theory calculation in [5] gives about 36% discrepancy between the Next-Next-Leading-Order (NNLO) calculation and the Next-Leading-Order (NLO) calculation, and the NNLO calculation has 40% systematic errors. In the later article [6], a smaller systematic error was estimated for the NNLO calculation, but still has the size of 15%. Lattice QCD, on the other hand, can have all systematic errors controlled, provided we perform the calculation

on a large physical volume with physical quark masses. In this work, we present the first near-physical and physical calculation of ΔM_K with lattice QCD. The near physical calculation was performed on an ensemble that has inverse lattice spacing 1.38 GeV with 170 MeV pion masses, while the physical calculation was performed on an ensemble with inverse lattice spacing is 2.36 GeV and physical quark masses.

Indirect CP violation was observed in the kaon to two-pion decays, and the parameter describing the size of this CP-violation, ϵ_K, has an experimental value of $2.228(11) \times 10^{-3}$. Unlike the ΔM_K, ϵ_K receives most of its contribution from short-distance effects. Therefore the perturbation theory gives a more reliable estimation for the ϵ_K. However, if we want a complete calculation based on the Standard Model, the long distance must be included. The current discrepancy between the SM prediction and experiment [7] make the long-distance effect more interesting. We present the first calculation of the long-distance effects in ϵ_K. This work is however calculated with unphysical kinematics, so we can not make a direct comparison with experiment. This calculation demonstrates of the method as well as providing an understanding the size of the long-distance contributions. We note that the ϵ_K calculation is harder than that for ΔM_K, partly because of the short-distance divergence present in the ϵ_K calculation. We need to correct this unphysical divergence in our lattice calculation. Another reason is we have to include more lattice operators and compute more contractions.

In Chapter 2, we will briefly introduce the neutral kaon mixing system, and the current status of the perturbation theory calculation. In Chapter 3, we show the method we used to compute this second order mixing process on the lattice. In Chapter 4, we introduce the measurement methods we used as well as the data analysis methods. In the following three chapters, we will show the results of our calculation for ϵ_K, the near-physical ΔM_K calculation and finally the physical ΔM_K calculation.

Chapter 2

Introduction to $K^0 - \bar{K}^0$ mixing

2.1 Phenomenology of $K^0 - \bar{K}^0$ mixing and CP violation

The two neutral kaon states in nature, the K_L and K_S mesons, are the two time-evolution eigenstates of the $K^0 - \bar{K}^0$ mixing system. The subscripts specify their lifetimes, being long lived or short lived. The quantity ΔM_K, which is their mass difference, is defined as follows:

$$\Delta M_K = m_L - m_S, \tag{2.1}$$

where the m_L and m_S are the masses of the K_L and K_S respectively.

The $K \to \pi^+\pi^-$ experiment has observed CP violation in the neutral kaon decays. This is because the two pion state must be CP even, while the K_L meson, which was believed to have odd CP, can decay into the $\pi^+\pi^-$ state. This process is caused by two effects. The first is called indirect CP violation, which results because the K_L is actually not a pure CP odd state, and mixes with the CP even state. The parameter ϵ, is used to represent the strength of this indirect CP violation. The second is called the direct CP violation, which results from the CP odd component of K_L decays directly into the $\pi^+\pi^-$ state. People use ϵ' to denote the size of this direct CP violation. The direct CP violation is much more rare compared than

the indirect one, and it has been measured in experiment that $|\epsilon'/\epsilon| \sim 10^{-3}$[8]. Therefore, in our analysis of ϵ, we can ignore the direct CP violation and define the ϵ as:

$$\epsilon = \frac{\mathcal{A}(K_L \to \pi\pi(I=0)}{\mathcal{A}(K_S \to \pi\pi(I=0)}, \tag{2.2}$$

where the $I = 0$ denotes the two pion state with isospin 0. We note that there exist different definitions of ϵ, which all agree when we ignore the direct CP violation. The quantity ϵ is often referred to as ϵ_K to specify that it is observed in kaon decays.

Both ΔM_K and ϵ_K have precise experimental values [8], making them ideal test for the Standard Model:

$$\Delta M_K = 3.483(6) \times 10^{-12} \text{ MeV}, \tag{2.3}$$

$$\epsilon_K = 2.228(11) \times 10^{-3}. \tag{2.4}$$

2.1.1 The $K^0 - \bar{K}^0$ system

The K^0 and its anti-particle $\bar{K}^0$, mix with each other. Their mixing can be represented by:

$$i\frac{d}{dt}\begin{pmatrix} K^0(t) \\ \bar{K}^0(t) \end{pmatrix} = (M - \frac{i}{2}\Gamma)\begin{pmatrix} K^0(t) \\ \bar{K}^0(t) \end{pmatrix}. \tag{2.5}$$

Here M is the dispersive part which defines the masses of the neutral kaon states, and Γ is the absorptive part which defines decay widths of the mass eigenstates in the presence of the weak interaction. The states $|K^0\rangle$ and $|\bar{K}^0\rangle$ can be related by the phase convention:

$$\text{CP}|K^0\rangle = -|\bar{K}^0\rangle. \tag{2.6}$$

The state on both sides of Eq. 2.5 stands for $K^0(t)|K^0\rangle + \bar{K}^0(t)|\bar{K}^0\rangle$. In general, the Hermitian matrices M and Γ can be parameterized using the identity and the Pauli matrices as follows:

$$M = c_0^m I + \sum_{i=1}^{3} c_i^m \sigma_i, \tag{2.7}$$

$$\Gamma = c_0^\gamma I + \sum_{i=1}^{3} c_i^\gamma \sigma_i. \tag{2.8}$$

Under CP and time reversal, the matrix X transform as follows ($X = M, \Gamma$):

$$\text{CP:} \quad X \to \sigma_1 X \sigma_1, \tag{2.9}$$

$$\text{T:} \quad X \to X^\dagger. \tag{2.10}$$

Then it is clear that CPT symmetry requires $c_3 = 0$ for both M and Γ, and therefore they both have equal diagonal elements. If we have $c_2 = 0$, we will have CP symmetry and the eigenstate of the mixing system will be:

$$|K_1\rangle = \frac{1}{\sqrt{2}} \left(|K^0\rangle - |\bar{K}^0\rangle \right), \tag{2.11}$$

$$|K_2\rangle = \frac{1}{\sqrt{2}} \left(|K^0\rangle + |\bar{K}^0\rangle \right). \tag{2.12}$$

The eigenstates $|K_1\rangle$ and $|K_2\rangle$ are CP eigenstates, with $|K_1\rangle$ being CP even and $|K_2\rangle$ being CP odd. However, due to the existence of CP violation, we will have a small non-zero value for c_2. The $|K_1\rangle$ and $|K_2\rangle$ will not be the eigenstates of the mixing matrix. Instead, the physical eigenstate are:

$$|K_S\rangle = \frac{1}{\sqrt{1 + |\bar{\epsilon}^2|}} \left(|K_1\rangle + \bar{\epsilon} |K_2\rangle \right), \tag{2.13}$$

$$|K_L\rangle = \frac{1}{\sqrt{1 + |\bar{\epsilon}^2|}} \left(|K_2\rangle + \bar{\epsilon} |K_1\rangle \right). \tag{2.14}$$

Because of the small size of the CP violation, the real parts of the off-diagonal matrix elements of both M and Γ are much larger than the imaginary parts ($c_1 \gg c_2$). Therefore, we can write the following expression for the $\bar{\epsilon}$ in Eq. 2.13 and Eq. 2.14:

$$\bar{\epsilon} = \frac{i}{2}\frac{\mathrm{Im}\, M_{0\bar{0}} - i\,\mathrm{Im}\,\Gamma_{0\bar{0}}/2}{\mathrm{Re}\, M_{0\bar{0}} - i\,\mathrm{Re}\,\Gamma_{0\bar{0}}/2}. \tag{2.15}$$

The difference of eigenvalues of the mixing matrix is given by:

$$\begin{aligned} \Delta\lambda &= (m_L - m_S) - \frac{i}{2}(\Gamma_L - \Gamma_S) \\ &= 2\left(M_{0\bar{0}} - \frac{i}{2}\Gamma_{0\bar{0}}\right)^{\frac{1}{2}}\left(M_{\bar{0}0} - \frac{i}{2}\Gamma_{\bar{0}0}\right)^{\frac{1}{2}} \approx 2\,\mathrm{Re}\, M_{0\bar{0}} - i\,\mathrm{Re}(\Gamma_{0\bar{0}}) \end{aligned} \tag{2.16}$$

2.1.2 Formulae for ΔM_K and ϵ_K

We have shown in Eq. 2.16, that ΔM_K is the difference of the eigenvalues of the matrix M, and since the imaginary part of the off diagonal matrix elements of the mixing matrix M is much less than the real part (by a factor of $\mathcal{O}(10^3)$), we arrive at the formula:

$$\Delta M_K = 2\,\mathrm{Re}\, M_{0\bar{0}}. \tag{2.17}$$

We work to second order in of the weak Hamiltonian H_W, which is equivalent to the second order in the Fermi coupling constant G_F. We can then write the matrix element $M_{0\bar{0}}$ as follows:

$$M_{0\bar{0}} = \langle K^0|H_W|\bar{K}^0\rangle + \mathcal{P}\sum_n \frac{\langle K^0|H_W|n\rangle\langle n|H_W|\bar{K}^0\rangle}{m_K - E_n}. \tag{2.18}$$

The $\mathcal{P}$ denotes the principal value of the generalized summation over all the intermediate states $|n\rangle$. We have adopted an normalization for the wave function that $\langle K(p_n)|K(p'_n)\rangle = \delta_{n,n'}$, so that our formula Eq. 3.15 is different from the common formula by a factor of $2m_K$.

This choice of normalization will make our finite volume lattice calculation easier.

Now we discuss how we relate the ϵ_K defined in Eq. 2.2 and the $\bar{\epsilon}$ defined in Eq. 2.15. We first define the isospin amplitude A_I and the phase factor ξ_I and δ_I as follows ($I = 0, 2$):

$$\begin{aligned} \mathcal{A}(K^0 \to \pi\pi(I)) &= A_I e^{i\delta_I} = |A_I| e^{i\xi_I} e^{i\delta_I}, & (2.19) \\ \mathcal{A}(\bar{K}^0 \to \pi\pi(I)) &= -A_I^\dagger e^{i\delta_I} = -|A_I| e^{-i\xi_I} e^{i\delta_I}. & (2.20) \end{aligned}$$

We can derive similar expressions for the CP eigenstates $|K_1\rangle$ and $|K_2\rangle$:

$$\begin{aligned} \mathcal{A}(K_1 \to \pi\pi(I)) &= \sqrt{2}\,\mathrm{Re}\,(A_I) e^{i\delta_I}, & (2.21) \\ \mathcal{A}(K_2 \to \pi\pi(I)) &= i\sqrt{2}\,\mathrm{Im}\,(A_I) e^{i\delta_I}. & (2.22) \end{aligned}$$

Using Eq. 2.13 and Eq. 2.14, we can derive the following expression for ϵ_K from Eq. 2.2:

$$\begin{aligned} \epsilon_K &= \frac{i\,\mathrm{Im}\,A_0 + \bar{\epsilon}\,\mathrm{Re}\,A_0}{\mathrm{Re}\,A_0 + i\bar{\epsilon}\,\mathrm{Im}\,A_0} \\ &= \frac{\bar{\epsilon} + i\xi_0}{1 + i\bar{\epsilon}\xi_0} \\ &\approx \bar{\epsilon} + i\xi_0. \end{aligned} \tag{2.23}$$

The quantity $\xi_0 = \frac{\mathrm{Im}\,A_0}{\mathrm{Re}\,A_0}$ is the ratio of the imaginary part of A_0 over the real part. It has been calculated with lattice QCD in [4] and it is smaller than $\bar{\epsilon}$ by an order of 10^{-2}. We have dropped higher order terms in the last line.

Next we try to simplify Eq. 2.15. Because the neutral kaon decay final states are dominated by the two-pion states with $I = 0$, we can arrive at the following approximation:

$$\frac{\mathrm{Im}\,\Gamma_{0\bar{0}}}{\mathrm{Re}\,\Gamma_{0\bar{0}}} = \xi_0. \tag{2.24}$$

We define the phase angle θ such that

$$\tan\theta = \frac{2\,\mathrm{Re}\,M_{0\bar{0}}}{\mathrm{Re}\,\Gamma_{0\bar{0}}}, \tag{2.25}$$

and we can use θ to write Eq. 2.15 as follows:

$$\bar{\epsilon} = \mathrm{e}^{i\theta}\sin\theta\left(\frac{\mathrm{Im}\,M_{0\bar{0}}}{\Delta M_K} - i\xi_0\cot\theta\right). \tag{2.26}$$

Substituting this into Eq. 2.23, we finally find:

$$\epsilon_K = \mathrm{e}^{i\theta}\sin\theta\left(\frac{-\,\mathrm{Im}\,M_{\bar{0}0}}{\Delta M_K} + \xi_0\right). \tag{2.27}$$

We have added a minus sign on the numerator and changed $\mathrm{Im}\,M_{0\bar{0}}$ to $\mathrm{Im}\,M_{\bar{0}0}$ for convenience. To calculate ϵ_K from the Standard Model, we will calculate the $\mathrm{Im}\,M_{0\bar{0}}$, then use the experimental value for ΔM_K in the denominator. The angle θ is close to $45°$, and more precise measurements gives:

$$\theta = 43.52(5)°. \tag{2.28}$$

In the following two sections, we discuss the procedure used in the past to carry out the Standard Model calculation of ΔM_K and ϵ_K from perturbation theory. We will see that the perturbation theory calculation for ΔM_K is very unreliable because of the large size of higher order corrections, and only calculation from the lattice can give reliable results. On the other hands, the perturbation theory calculation ϵ_K is more reliable. In section 2.4, we summarize the current status for the perturbative calculation of ϵ_K, and we can see that the increase in the precision of the short-distance, perturbative calculation and its difference from the experimental value makes the lattice calculation of the long distance part also necessary.

2.2 Tree level perturbation theory calculation

Two types of diagrams contribute to the process of $K^0 - \bar{K}^0$ mixing. They are shown in Fig. 2.1. The external legs of these diagram correspond to the incoming and outgoing kaons, and the two internal quark lines represent a sum over all the up type flavors. The lowest order, short distance calculation treats the box diagram as a coefficient times a local $\Delta S = 2$ operator $O_{LL} = (\bar{s}d)_{V-A}(\bar{s}d)_{V-A}$, and this calculation was first carried out in [9]. The subscript $V - A$ means a left handed vertex which has a spin structure of $\gamma_\mu(1 - \gamma_5)$. The coefficient multiplying the local operator is often referred to as an Inami-Lim function.

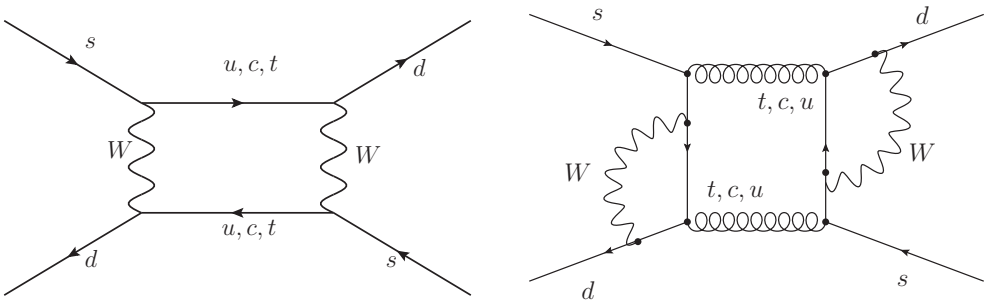

Figure 2.1: Two types of diagrams contributing to the $K^0 - \bar{K}^0$ mixing process. On the left is the box diagram and on the right is the disconnected diagram.

In this lowest order perturbative calculation where we have a sum of three up-type flavors, one uses a unitary condition of the CKM matrix:

$$\lambda_u + \lambda_c + \lambda_t = 0, \tag{2.29}$$

where $\lambda_i = V_{i,d}V_{i,s}^*$, and writes the sum as two terms. The usual choice is to eliminate the λ_u and subtract an up quark from all the internal quark lines. This procedure can be illustrated using the free field propagator formula:

$$\sum_{i=u,c,t} \frac{\lambda_i \not{p}}{p^2 + m_i^2} = \lambda_c \left\{ \frac{\not{p}}{p^2 + m_c^2} - \frac{\not{p}}{p^2 + m_u^2} \right\} + \lambda_t \left\{ \frac{\not{p}}{p^2 + m_t^2} - \frac{\not{p}}{p^2 - m_u^2} \right\}. \tag{2.30}$$

After the subtraction of the up quark, the up mass is set to be zero, which is a very good approximation due to the small mass of the up quark. Finally the $\Delta S = 2$ effective Hamiltonian is written as in Eq.2.31, where S_0 is the Inami-Lim function introduced above. We show the formula for the Inami-Lim functions wirtten for different values for its arguments in Eq. 2.32 - Eq. 2.34, where $x_i = \frac{m_i^2}{M_W^2}$.

$$H_{eff}^{\Delta S=2} = \frac{G_F^2}{16\pi^2} M_W^2 \left[\lambda_c^2 S_0(x_c) + \lambda_t^2 S_0(x_t) + 2\lambda_c\lambda_t S_0(x_c, x_t)\right] O_{LL} + H.c. \tag{2.31}$$

$$S_0(x_c) = x_c, \tag{2.32}$$

$$S_0(x_t) = \frac{4x_t - 11x_t^2 + x_t^3}{4(1-x_t)^2} - \frac{3x_t^3 \ln x_t}{2(1-x_t)^3}, \tag{2.33}$$

$$S_0(x_c, x_t) = x_c \left[\ln \frac{x_t}{x_c} - \frac{3x_t}{4(1-x_t)} - \frac{3x_t^2 \ln x_t}{4(1-x_t)^2}\right] \tag{2.34}$$

We note that this lowest order calculation is very imprecise because first order QCD corrections can be 50%. However, we can examine the size of the different terms to understand their contribution ΔM_K and ϵ_K. Among the Inami-Lim functions, $S_0(x_c)$ has the smallest size, being $\sim 10^{-4}$. The second case $S_0(x_c, x_t)$ is one order larger due to the existence of the large logarithm. The third case $S_0(x_t)$ is the largest with the size of order 1. The contribution to ΔM_K is only relevant to the real part of $H_{eff,SD}$, and because the real part of λ_c is about 1000 times larger than its imaginary part and both the real and imaginary part of λ_t, we can see that the major contribution to ΔM_K is from the first term. However, for the ϵ_K, we want to evaluate $\mathrm{Im}\, M_{\bar{0}0}$, so we are interested in the imaginary part of H_{eff}. By looking at the sizes of the imaginary part of each term, we can then confirm that the contribution from this three term are more nearly of the same order, with the λ_t^2 term having the largest contribution.

2.3 Perturbative calculation at Next Leading Order

The conventional approach to this perturbative calculation involves using the CKM unitary relation and subtract the up quark from each of the two internal quark lines in the box diagram. This was introduced in the previous section. In this section, we introduce the Next Leading Order (NLO) calculation. First we will present the result with the conventional treatment subtracting the up quark, then we will introduce our unconventional method of subtracting the charm quark from the two internal quark lines. We choose to subtract the charm quark because we will then have three terms in the H_{eff}: a term proportional to λ_u^2, a term proportional to λ_t^2, and a term proportional to $\lambda_u\lambda_t$. The first term does not receive an imaginary part from its CKM matrix element, and the second term is purely short distance dominated by the heavy top quark. So our lattice calculation for the ϵ_K can focus only on the last term. This greatly simplify our calculation.

The NLO calculation for the term with λ_t^2 begins by integrating out the top quark and the W boson, we then obtain a coefficient multiplied by the local $\Delta S = 2$ operator. Next we use renormalization group running to obtain this coefficient at a scale μ_c, which is a few GeV where we can evaluate the matrix element $\langle K^0|O_{LL}|\bar{K}^0\rangle$. The NLO calculation for the other two terms follows a common procedure. We first integrate out the top quark and W boson and obtain a bi-local structure, which is a product of two $\Delta S = 1$ operators. For the term that has a λ_t factor so there is an internal top quark, there will also be a local part in which has the $\Delta S = 2$ operator appears. One then goes to a low scale μ_c using renormalization group running, at which they the charm quark is integrated out and the product of two $\Delta S = 1$ operator is treated as a coefficient multiplying the $\Delta S = 2$ local operator. Thus, the final expression is an effective Hamiltonian made up of a single $\Delta S = 2$ local operator O_{LL}, defined at a scale μ_c. In the last step, the matrix element $\langle K^0|O_{LL}|\bar{K}^0\rangle$ is evaluated.

2.3.1 The conventional up quark subtraction

Using the conventional up quark subtraction method, one will arrive at an effective Hamiltonian shown in Eq. 2.35. We have added the subscription SD to show that this is a result coming from a short distance approximation in which the charm quark is integrated out and the bi-local structure of the box diagram is treated as a local operator multiplied by a Wilson coefficient. We will show in later chapters that this short distance calculation is unable to control systematic errors from long distance effect , so we need a non-perturbative lattice calculation combined with a perturbative matching to continuum. This approach will improve the accuracy of this short distance calculation.

$$H_{eff,SD}^{\Delta S=2} = \frac{G_F^2}{16\pi^2} M_W^2 \left[\lambda_c^2 \eta_1 S_0(x_c) + \lambda_t^2 \eta_2 S_0(x_t) + 2\lambda_c \lambda_t \eta_3 S_0(x_c, x_t)\right] O_{LL} + H.c. \qquad (2.35)$$

The result for each term in Eq. 2.35could be found in [10]. The η terms are called the 'QCD corrections', which include all the one-loop QCD effect. The fact that the η are not close to one demonstrate the importance of the QCD corrections. We note that the NLO calculation of the term proportional to λ_c^2 is accurate to order $\mathcal{O}(\alpha_s)$. That is, the α_s terms in the result are correct. However, the NLO calculation for the term proportional to $\lambda_c\lambda_t$ will be accurate to order $\mathcal{O}(\alpha_s \ln \mu/M_W)$. This is because we have a logarithmic divergence when the two effective $\Delta S = 1$ operators are close to each other, and this divergence indicate the existence of the large logarithm in the Inami-Lim function. Therefore, the Leading Order (LO) will be accurate to order $\mathcal{O}(\ln \mu/M_W)$. This logarithm is roughly on the size of $1/\alpha_s$, so we call the LO part has an accuracy $\mathcal{O}(1/\alpha_s)$. The NLO part will then be of order $\alpha_s \ln \mu/M_W$, or order $\mathcal{O}(1)$. We will discuss the details of this logarithmic divergence in later chapters where we discuss our calculation of ϵ_K.

We should note that having a higher order of accuracy does not mean the result is more

reliable. The result for the term η_2 is most reliable and it can be calculated most precisely with the smallest systematic error from the perturbation theory at short distance. This is because the term it evaluates corresponds to a structure of $(t-u)\times(t-u)$ in the two internal quark lines of the box diagram. The top quark makes it purely short distance dominated. The term η_3 is less accurate because it is evaluating a structure $(t-u)\times(c-u)$. This term will receive both short distance and long distance contributions. The η_1 is least accurate because it evaluates a structure $(c-u)\times(c-u)$, which receive most of its contributions from the charm energy scale, so the long distance effect can be very important. In [7], it has been shown that the NLO result of η_1 is 1.43(23) and the NNLO result is 1.72(27), raising questions if perturbation theory for this term converges. Because ΔM_K is dominated by this term, its perturbative calculation is very unreliable and ΔM_K must be evaluated using a non-perturbative method. On the other hand, ϵ_K receives more contribution from the λ_t^2 term and η_2, so its perturbative calculation is more reliable. However, although the contribution from the other two terms is smaller, both are on the same order and neither can not be ignored. Therefore the long distance calculation is also very important. We will see in section 2.4 that there is some discrepancy between the SM prediction and experiment, making the long distance calculation very interesting.

2.3.2 Our charm quark subtraction

As explained earlier, instead of subtracting an up quark in the internal quark line of the box diagram, we do a charm quark subtraction. Our effective Hamiltonian will then have three terms: a term proportional to λ_u^2 with internal quark line structure $(u-c)\times(u-c)$, a term proportional to λ_t^2 with a structure $(t-c)\times(t-c)$, and a term proportional to $\lambda_u\lambda_t$ with a

structure $(t-c)\times(u-c)$. We can write our effective Hamiltonian as follows:

$$H_{eff,SD}^{\Delta S=2} = \frac{G_F^2}{16\pi^2}M_W^2\left[\lambda_u^2\eta_1' S_0(0,0,x_c)+\lambda_t^2\eta_2' S_0(x_t,x_t,x_c)\right. \\ \left.+2\lambda_u\lambda_t\eta_3' S_0(x_t,0,x_c)\right]O_{LL}+H.c. \tag{2.36}$$

We have used a different notation to represent the Inami-Lim function and QCD corrections. We write the Inami-Lin function showing all three argument $S_0(x_1,x_2,x_3)$, which represents the internal quark structure $(q_1-q_3)\times(q_2-q_3)$, with the last argument indicating the flavor been subtracted. We have used $x_u=0$. For the η_i which represent the QCD corrections, we have added a prime to make the distinction. Now the term proportional to $\lambda_u\lambda_u$ is purely real and does not receive an imaginary part from its CKM factor, so it does not contribute to $\mathrm{Im}\, M_{\bar{0}0}$. The remaining two terms have contributions nearly of the same order. This is because $S_0(x_t,0,x_c)=O(10^{-3})$, $S_0'(x_t,x_t,x_c)=O(1)$, and $\lambda_t/\lambda_u\approx 0.0016$. The term proportional to $\lambda_t\lambda_t$ can be calculated in perturbation theory with very high precision since it is short-distance dominated. One might think that this term also has a contribution coming from two internal charm quark which includes long distance effect, but this term is suppressed by λ_t/λ_u , compared to the long distance effects in the $\lambda_u\lambda_t$ term. The term with $\lambda_u\lambda_t$ has a long distance contribution which is not suppressed by the CKM matrix, and therefore this is the only term we must calculate with lattice QCD. By comparing the conventional formula in Eq. 2.35 to our Eq. 2.36, we can find the equations that relate the quantities in our new notation (with a prime) with those in the old ones:

$$S_0(x_c) - S_0(x_c, x_t) = S_0(x_t, 0, x_c) \tag{2.37}$$

$$\eta_1 S_0(x_c) - \eta_3 S_0(x_c, x_t) = \eta_3' S_0(x_t, 0, x_c) \tag{2.38}$$

$$S_0(x_t) + S_0(x_c) - 2S_0(x_c, x_t) = S_0(x_t, x_t, x_c) \tag{2.39}$$

$$\eta_2 S_0(x_t) + \eta_1 S_0(x_c) - 2\eta_3 S_0(x_c, x_t) = \eta_2' S_0(x_t, x_t, x_c) \tag{2.40}$$

2.4 Current status for the perturbative ϵ_K

We have shown in previous sections that the perturbation theory calculation for ΔM_K give unreliable results. In this section, we will summarize the current status of the perturbation theory calculation of ϵ_K. Here we follow the usual convention of subtracting the up quark and separating the contribution into three terms. The current status of the short distance calculation has been summarized in [11]. We have two major source of uncertainties in this short distance calculation. One is from the parameters in the CKM matrix element, and the other is from the evaluation of the η term from perturbation theory.

We first introduce the Wolfenstein parametrization for the CKM matrix elements. With the Wolfenstein parametrization, we can express the CKM matrix with four independent parameters: λ, A, ρ, and η. The Wolfenstein parametrization is an approximation, and the CKM matrix for accuracy of order $\mathcal{O}(\lambda^3)$ is given in Eq. 2.16 of [10]. For accuracy to order$\mathcal{O}(\lambda^5)$, we have:

$$\lambda_u = \lambda - \frac{\lambda^3}{2} - \frac{\lambda^5}{8} \tag{2.41}$$

$$\lambda_c = -\lambda + \frac{\lambda^3}{2} + \frac{\lambda^5}{8} + A^2\lambda^5(1-\bar{\rho}) - i\eta A^2\lambda^5 \tag{2.42}$$

$$\lambda_t = -A^2\lambda^5(1-\bar{\rho}) + i\eta A^2\lambda^5 \tag{2.43}$$

The value for V_{cb} is commonly used to describe the uncertainty for ϵ_K, and this is done by using $|V_{cb}| = A\lambda^2 + \mathcal{O}(\lambda^8)$ to eliminate the A in the above equations.

The QCD corrections in Eq. 2.35 have been calculated in P.T. in NLO and NNLO. For the term η_2, because it is very accurate in P.T., the NLO calculation is enough, while the other two terms η_1 and η_3 has been calculated through NNLO. We have listed the results in Table 2.1.

η_1^{NLO}	η_1^{NNLO}	η_2^{NLO}	η_3^{NLO}	η_3^{NNLO}
1.43(23)	1.72(27)	0.5765(65)	0.47(4)	0.496(47)

Table 2.1: The value for the QCD correction terms η_i, calculated in NLO and NNLO.

Substituting Eq. 2.35 into Eq.2.27, we get the following formula for the perturbative calculation of ϵ_K:

$$\epsilon_K = e^{i\theta}\sqrt{2}\sin(\theta)\left(C_\epsilon B_K X + \frac{\xi_0}{\sqrt{2}}\right), \tag{2.44}$$

$$C_\epsilon = \frac{G_F^2 F_K^2 m_{K^0} M_W^2}{6\sqrt{2}\pi^2 \Delta M_K}, \tag{2.45}$$

$$X = \mathrm{Im}\,\lambda_t\left[\mathrm{Re}\,\lambda_c\eta_1 - \mathrm{Re}\,\lambda_t\eta_2 S_0(x_t) - (\mathrm{Re}\,\lambda_c - \mathrm{Re}\,\lambda_t\eta_3 S_0(x_c, x_t))\right]. \tag{2.46}$$

The quantity B_K in the above equation is the 'kaon bag parameter', defined by:

$$\langle \bar{K}^0|O_{LL}|K^0\rangle = \frac{4}{3}B_K F_K^2 m_K^0. \tag{2.47}$$

Substituting the values for the η_i terms into Eq.2.27, and using the CKM matrix parameter λ, $\bar{\eta}$ and $\bar{\rho}$, we can find the current results for the perturbative calculation of ϵ_K. In [11], the authors took the value for the CKM parameters from the CKMfitter [8], and used both the inclusive value and exclusive value for V_{cb} from [8]. The final results for ϵ_K is given are Table. 2.2.

We can see a 2.7 σ discrepancy between experiment if the exclusive value for V_{cb} is

input method for V_{cb}	inclusive	exclusive
ϵ_K	2.31(23)	1.73(18)
dev from ϵ_K^{EXP}	-0.34 σ	2.7 σ

Table 2.2: The value for ϵ_K from different input method for V_{cb}. We have also shown the deviation from the experimental value.

used, while using the inclusive value we get a result consistent with experiment. We note that in the above perturbative calculation, the long distance contribution is not treated correctly. The charm quark has been integrated out at scale $\mu \sim m_c$, and the long distance contribution is represented as a local operator multiplied by a coefficient. This process is problematic since m_c is not heavy, and the long distance, low energy contribution at charm scale cannot be correctly included. Also, in order to integrate out the charm, one must work at scale μ at or below the charm quark mass, where the perturbative calculation is no longer reliable due to the large α_s. Therefore, to check the correctness of this Standard Model calculation, and possibly understand the current inconsistency between the theoretical calculation and experiment, the long distance contribution to ϵ_K must be included, which can only be calculated using lattice QCD.

Chapter 3

$K^0 - \bar{K}^0$ mixing on the lattice

3.1 Introduction of Lattice QCD

Lattice QCD is the only known method to solve QCD problems non-perturbatively. We have discussed the non-perturbative characteristic of the kaon mixing problem, now we will give a brief general introduction to the lattice QCD method.

We work in Euclidean space, and write the path integral partition function as:

$$Z = \int D[q]D[\bar{\psi}]D[\psi]\langle O\rangle e^{-S_G[q]-S_F[q,\psi,\bar{\psi}]}, \tag{3.1}$$

where S_G is the gauge action and S_F is the fermion action. To calculate any Green function O, we must integrate out the fermion degrees of freedom, then perform the average over gauge configurations. Assuming the fermion action takes the form $S_F = \bar{\psi}\tilde{K}\psi$, we have:

$$\begin{aligned} \langle O[q,\psi,\bar{\psi}]\rangle &= \frac{\int D[q]D[\bar{\psi}]D[\psi]\langle O\rangle e^{-S_G[q]-S_F[q,\psi,\bar{\psi}]}}{\int D[q]D[\bar{\psi}]D[\psi]e^{-S_G[q]-S_F[q,\psi,\bar{\psi}]}} \\ &= \frac{\int D[q]\langle O\rangle_{S_F} e^{-S_{eff}[q]}}{\int D[q]e^{-S_{eff}[q]}}, \end{aligned} \tag{3.2}$$

where

$$\langle O\rangle_{S_F} = \frac{\int D[\bar{\psi}]D[\psi]O[q,\psi,\bar{\psi}]e^{-S_F[q,\psi,\bar{\psi}]}}{\int D[\bar{\psi}]D[\psi]e^{-S_F[q,\psi,\bar{\psi}]}} \tag{3.3}$$

$$S_{eff}[q] = S_G[q] - \ln \det\tilde{K}[q] \tag{3.4}$$

The quantity $\langle O[q,\psi,\bar{\psi}]\rangle$ in Eq. 3.3 can be calculated by averaging over a large number of gauge configurations. We first discretize space-time by introducing a four dimensional grid (the lattice), and then create the gauge configuration using a Hybrid Monte Carlo (HMC) method [12] before we perform this measurement. We perform N measurement on N different gauge configurations, and then find $\langle O[q,\psi,\bar{\psi}]\rangle = \frac{1}{N}\sum_{i=1}^{N} O[q,\psi,\bar{\psi}]$.

We represent the fermion field as a Grassman number on each site of the four dimensional lattice, and associate the links connecting the lattice sites as our gauge field. The gauge field is represented as an $SU(3)$ matrix $U_\mu(n)$, connecting the n^{th} site and its next neighbor in the μ^{th} direction. The relationship between these link variables to the continuum gauge field A is given by

$$U_\mu(n) = e^{ig_0 aA_\mu(n)}, \tag{3.5}$$

We first introduce the gauge action. The simplest version, the Wilson action is defined as follow:

$$S_G^W(U) = -\sum_{x,\mu<\nu}\frac{\beta}{3}\mathrm{ReTr}\{U_P(x,\mu,\nu)\}. \tag{3.6}$$

Taking $\beta = \frac{6}{g^2}$, the above action can reproduce the continuum limit:

$$S_G^{cont} = \frac{1}{4}\int d^4x F_{\mu\nu}F_{\mu\nu}. \tag{3.7}$$

The gauge configurations we used in this work use the improved gauge action, the Iwasaki action [13], which also contains the 1×2 plaquettes:

$$S_G^R(U) = \beta \sum_{x,\mu<\nu} (1 - \frac{c_0}{3}) \mathrm{ReTr}\{U_P(x,\mu,\nu)\} + \beta \sum_{x,\mu\neq\nu} (1 - \frac{c_1}{3}) \mathrm{ReTr}\{U_R(x,\mu,\nu)\}, \tag{3.8}$$

$$c_1 = -0.331,\ c_0 = 1 - 8c_1. \tag{3.9}$$

The SU(3) product $U_R(x,\mu,\nu)$ is the rectangle plaquette:

$$U_R(x,\mu,\nu) = U_\mu(n) U_\mu(n+\hat{\mu}) U_\nu(n+2\hat{\mu}) U_\mu^\dagger(n+\hat{\mu}+\hat{\nu}) U_\mu^\dagger(n+\hat{\nu}) U_\nu^\dagger(n). \tag{3.10}$$

The fermion action on the space-time lattice is more complicated, since the naive discretization fails because of the fermion doubling problem [14]. We want to have a fermion action that can solve the doubling problem and allow us to retain chiral symmetry. The domain wall fermion formulation is one of these choices. It introduces an extra dimension, the fifth dimension, labelled by s, in addition to the 4 dimensional space-time labeled by x, y, z, t. With a choice of the 'Domain Wall Height', the M, we can have the left-handed field exponentially bound to the $s = 0$ domain wall, while the right-handed field is bound to the $s = L_s - 1$ wall. The integer L_s is the size of the fifth dimension. The DWF action is given as follows:

$$S_F^{DWF} = - \sum_{n,s;n',s'} \bar{\psi}(n,s) D^{DWF}(n,s;n',s') \psi(n',s'), \tag{3.11}$$

$$D^{DWF}(n,s;n',s') = \delta_{s,s'} D^{\parallel}_{n,n'} + \delta_{n,n'} D^{\perp}_{s,s'}\ . \tag{3.12}$$

$$D^{\parallel}_{n,n'} = \frac{1}{2} \sum_\mu \left((1-\gamma_\mu) U_\mu(n) \delta_{n+\hat{\mu},n'} + (1+\gamma_\mu) U_\mu^\dagger(n') \delta_{n-\hat{\mu},n'} \right) + (M-4)\delta_{n,n'}, \tag{3.13}$$

$$D^{\perp}_{s,s'} = \frac{1}{2}[(1-\gamma_5)\delta_{s+1,s'} + (1+\gamma_5)\delta_{s-1,s'} - 2\delta_{s,s'}] - \frac{m}{2}[(1-\gamma_5)\delta_{s,L_s-1}\delta_{0,s'} + (1+\gamma_5)\delta_{s,0}\delta_{L_s-1,s'}], \tag{3.14}$$

With the introduction of the fifth dimension, we will have an increase in the computational cost by a factor of L_s, both in inverting the Dirac operator to solve the quark propagator and in solving the eigenvectors of the Dirac operator. We can reduce this extra cost by using Mobius fermions, which allow us to reduce the fifth dimension while having negligible effect on the results from the Green functions we compute. Mobius fermions are used in our measurements for ΔM_K using the 32^3 and the 64^3 ensembles. More information about the Mobius fermions can be found in [15].

3.2 $\Delta S = 2$ process on the lattice

We evaluate ΔM_K and ϵ_K from Eq. 2.17 and Eq. 2.27, and we therefore have to calculate $M_{0\bar{0}}$ on the lattice, using the formula introduced in the previous section:

$$M_{0\bar{0}} = \langle K^0 | H_W | \bar{K}^0 \rangle + \mathcal{P} \sum_n \frac{\langle K^0 | H_W | n \rangle \langle n | H_W | \bar{K}^0 \rangle}{m_K - E_n}. \tag{3.15}$$

We call the first part of Eq. 3.15 a local structure, which is produced by a local $\Delta S = 2$ operator in H_W, and the second part a bi-local structure, which is produced by the product of two $\Delta S = 1$ operator in H_W. We work in the four flavor theory with a valence charm quark. In the ΔM_K calculation, because there is no divergence when the two local operators are close to each other due to the GIM cancellation (more details in Chapter 6), we will not have a $\Delta S = 2$ counterterm in the H_W so we only use the second term on the right-hand side of Eq. 3.15. In the ϵ_K calculation, we will have a divergence due to the absence of a full-GIM cancellation (more details in Chapter 5), and we therefore have both a $\Delta S = 2$ local operator and the $\Delta S = 1$ operators in our H_W. The contribution of the local operator to $M_{0\bar{0}}$ can be calculated by evaluating the kaon bag parameter B_K defined by:

$$M_{0\bar{0}} = \langle K^0 | H_W | \bar{K}^0 \rangle = \frac{4}{3} B_K m_K F_K^2, \tag{3.16}$$

where the F_K is the kaon decay constant and m_K the kaon mass. In this work, we focus on the second half of Eq. 3.15, which is produced by a product of two $\Delta S = 1$ operator and contains the long distance contribution.

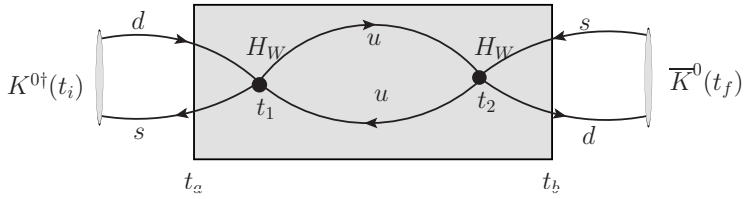

Figure 3.1: Example diagram for $K^0 - \bar{K}^0$ mixing. The two weak Hamiltonians are integrated over the time interval $[t_a, t_b]$. The internal quark lines should be u-type quark, which in our 4-flavor theory can be either up or charm.

We then evaluate a four point Green function represented in Fig. 3.1. We call this a four point function because it involves the initial state, the final state, and the two weak operators. It has the initial state and final state being K^0 or $\bar{K}^0$ at the times t_i and t_f, and the two weak Hamiltonian inserted at the times t_1 and t_2. By integrating the time-ordered product of the two $\Delta S = 1$ operator, we can obtain the integrated correlator for this $\Delta S = 2$ process. The integrated correlator is defined as:

$$\mathcal{A} = \frac{1}{2} \sum_{t_2=t_a}^{t_b} \sum_{t_1=t_a}^{t_b} \langle 0 | T \left\{ \overline{K}^0(t_f) H_W(t_2) H_W(t_1) \overline{K}^0(t_i) \right\} | 0 \rangle \,. \tag{3.17}$$

If we insert a complete set of intermediate states, we find:

$$\mathcal{A} = N_K^2 e^{-M_K(t_f - t_i)} \left\{ \sum_n \frac{\langle \bar{K}^0 | H_w | n \rangle \langle n | H_w | K^0 \rangle}{M_K - M_n} \left(-T + \frac{e^{(M_K - M_n)T} - 1}{M_K - M_n} \right) \right\} . \tag{3.18}$$

The term proportional to T can be related to $M_{0\bar{0}}$:

$$M_{0\bar{0}} = \sum_n \frac{\langle \bar{K}^0 | H_w | n \rangle \langle n | H_w | K^0 \rangle}{M_K - M_n} \,. \tag{3.19}$$

We have dropped the principal sum because we are not performing an integral.

The general approach we use to evaluate the $M_{0\bar{0}}$ is to calculate the integrated correlator Eq. 3.17 for various integration box size T, and then fit the linear part of Eq. 3.18. To do this, we need to find all the matrix element $\langle n|H_W|K^0\rangle$ for those intermediate states $|n\rangle$ that have energies lighter than the kaon, since for these terms, the exponential factor $e^{(m_K-m_n)T}$ may interfere with the determination of the linear-term. We then directly subtract the contributions of these exponential terms. For intermediate states heavier than the kaon, we will choose the length T our integration box large enough that the exponential term will be highly suppressed. Finally we can perform a correlated χ^2 linear fit to find the coefficient of the linear term which then determines $M_{0\bar{0}}$.

3.3 Operators and contractions

Now we introduce the relevant $\Delta S = 1$ operators in our weak Hamiltonian and the different contractions we get from inserting two $\Delta S = 1$ operator between in the kaon initial and final states. We have two current-current operators, denoted by Q_1 and Q_2, and are defined as follows:

$$Q_1^{qq'} = (\bar{s}_i d_i)_{V-A}(\bar{q}_j q'_j)_{V-A} \tag{3.20}$$

$$Q_2^{qq'} = (\bar{s}_i d_j)_{V-A}(\bar{q}_j q'_i)_{V-A}\,. \tag{3.21}$$

Because we work in four flavor theory, the q and q' in the current-current operators can be either the up quark or the charm quark, and the $V-A$ means the left handed projection $(\gamma_\mu(1-\gamma_5))$ is contracted with the two spinor field. The indices i and j are color indices.

We also have the QCD penguin operators $Q_{3,4,5,6}$. They are defined as follows:

$$Q_3 = (\bar{s}_i d_i)_{V-A} \sum_{q=u,d,s,c} (\bar{q}_j q_j)_{V-A}, \tag{3.22}$$

$$Q_4 = (\bar{s}_i d_j)_{V-A} \sum_{q=u,d,s,c} (\bar{q}_j q_i)_{V-A}, \tag{3.23}$$

$$Q_5 = (\bar{s}_i d_i)_{V-A} \sum_{q=u,d,s,c} (\bar{q}_j q_j)_{V+A}, \tag{3.24}$$

$$Q_6 = (\bar{s}_i d_j)_{V-A} \sum_{q=u,d,s,c} (\bar{q}_j q_i)_{V+A}. \tag{3.25}$$

The sum of all relevant flavors includes both the up-type flavors (up and charm) as well as the down type flavors (down and strange). Unlike the current-current operators, we now have both operators with two left handed vertices (Q_3, Q_4) and operators with one left handed vertex and one right handed vertex (Q_5, Q_6). We call the operators $Q_{1,3,5}$ color diagonal operators because their color indices are contracted in the same way as the spin indices, and conversely, we call the operators $Q_{2,4,6}$ color mixed operators. For a color mixed operator with two left handed vertices, we can use the Fierze symmetry and rewrite it as a color diagonal one:

$$(\bar{s}_i d_j)_{V-A}(\bar{q}_j q'_i)_{V-A} = (\bar{s}_i q'_i)_{V-A}(d_j \bar{q}_j)_{V-A}. \tag{3.26}$$

However, we should note this does not apply to the operators with a right handed vertex.

Inserting these $\Delta S = 1$ operators between the kaon initial and final states will produce the 5 types of four point diagrams shown in Fig. 3.2. Here we did not specify the type of the internal quarks because that will depend on which operators we have on the vertices. The vertex on the left side of the type 5 diagram must be a penguin operator, being either $(\bar{s}d)(\bar{s}s)$ or $(\bar{s}d)(\bar{d}d)$.

In our measurement, we also want to determine matrix elements such as $\langle \pi | Q_i | K^0 \rangle$ or $\langle \pi\pi | Q_i | K^0 \rangle$. We do so by measuring some three point functions. We call them three point

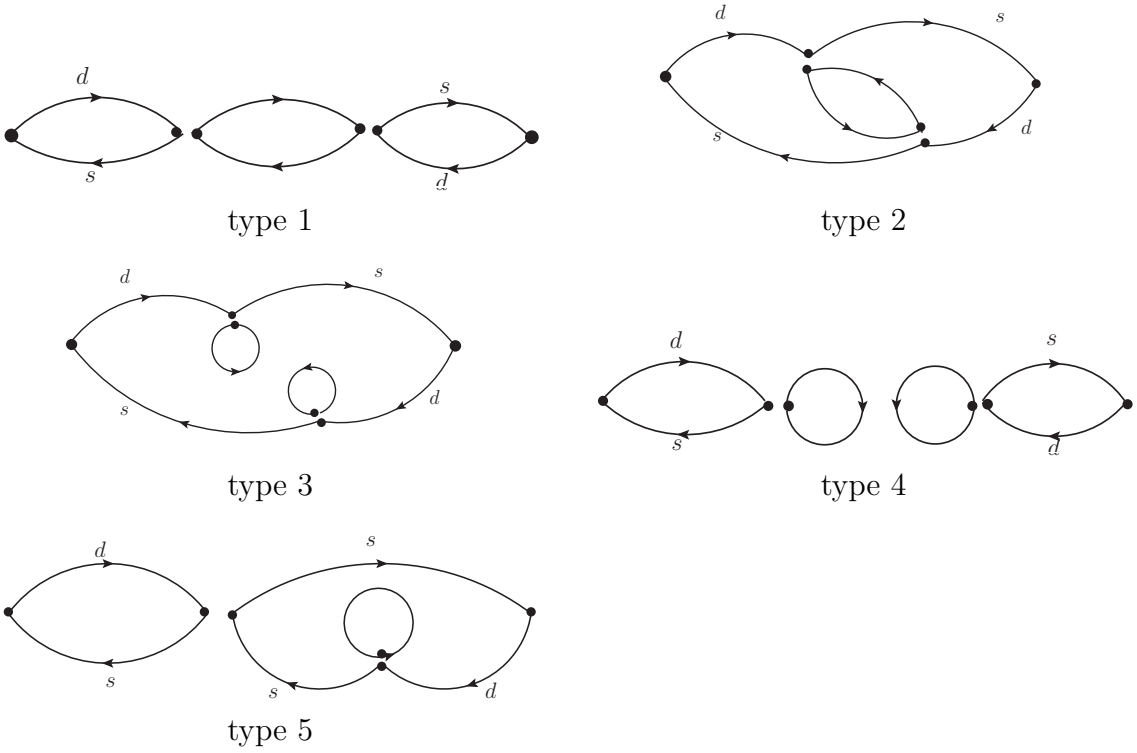

Figure 3.2: Five types of four point diagrams to calculate on the lattice.

functions because they only have an initial state, a final state and one weak operator. All the three point functions are shown in Appendix A. To obtain the energy of different meson such as pion and kaon, we must also evaluate two point functions such as $\langle \pi(t) | \pi(0) \rangle$. We also show the list of two point functions that we have calculated in Appendix A.

Chapter 4

Measurement methods and data analysis

4.1 Measurement methods

We now describe how we solve for the quark propagators and construct the Green functions we introduced in the previous chapter. We have three types of quark propagators to calculate on the lattice: the light quark, the strange quark, and the charm quark. We have treated the up and down quark the same as their mass are very close, and they are often referred to as the light quark.

4.1.1 General measurement methods

The measurements we have to perform require us to determine the two-point, three-point, and four-point Green functions that we will use in the analysis. This is achieved by computing the quark propagators and then contracting the spin and color indices. Ideally, we would compute a propagator $S(x; y)$, where the quark propagates from space-time point y (source)

to space-time point x (sink). This can be calculated by inverting the Dirac operator:

$$S(x;y) = D^{-1}(x;y). \tag{4.1}$$

This is unrealistic because inverting the huge matrix D is impossible. We therefore use another method which is to put a source 1 at point y, and then solving the linear equation

$$DS(x;y) = \eta(y), \tag{4.2}$$

where $\eta(y)$ is a vector with all entries 0 and the entry corresponding to y be 1. We call the propagator $S(x;y)$ computed this way a point source propagator. This equation can be solved using a standard iteration method called Conjugate Gradient (CG). Solving this equation with CG will be the most time consuming part of the measurement. Once we have solved this linear equation, we can find the propagator from the single source point y to any sink point x in the entire lattice. However, due to the computation cost, it is unrealistic to solve Eq. 4.2 for every source point y, because that will be the same as inverting the Dirac matrix. We therefore have to find a way to define our source so that we can solve the physics problem without having to do too many CG inversions.

In the Green functions we calculate, there is a source and/or sink corresponding to a kaon state. We used a Coulomb gauge fixed wall source for the kaon. A wall source means we set the source for all the space-time points at a specific time t to be 1, and set the source for all the other points to be 0. We therefore can construct a kaon source at time t_i by solving both the wall source light quark propagator and the strange quark propagator once. We solve this wall source propagators for all time slices t. We are then able to construct propagators for all the kaon sources and sinks. In the type 1 and 2 four point diagrams (Fig. 3.2), we have two internal vertices that are summed over the space-time volume. Since it is unrealistic to find a point propagator for each point of the space-time volume, we choose to solve a single

point source propagator for each time slice t at a single space point of our choice. We can then arrange for the other vertex to be at the sink point for each of the four propagators which are joined to it. This may require using γ_5 Hermiticity $S(x;y) = \gamma_5 S^\dagger(y;x)\gamma_5$. The second vertex can then be easily summed over any desired region. To show an example of the type 1 diagram contraction, we have the #1 of the type 1 four point Green functions in Fig. A.1 Appendix A:

$$\begin{aligned} \#1^{tp1}(t_i, t_x, t_y, t_f) &= V_{3D} \sum_{\vec{y}} \mathrm{Tr}\left[S_s^\dagger(x;t_i)\gamma_5\gamma_\mu(1-\gamma_5)S_d(x;t_i)\right] \\ &\quad \mathrm{Tr}\left[\gamma_\mu(1-\gamma_5)\gamma_5 S_u^\dagger(y;x)\gamma_5\gamma_\nu(1-\gamma_5)S_u(y;x)\right] \mathrm{Tr}\left[S_s^\dagger(y;t_f)\gamma_5\gamma_\nu(1-\gamma_5)S_d(y;t_f)\right]. \end{aligned} \tag{4.3}$$

We have only used a single point x for the time slice t_x so we multiply the result by the 3D volume V_{3D}. However, the second point y is treated as a sink and is summed over the full 3D volume. In the measurement, we want to extract the greatest statistics from the measurement on each Monte Carlo trajectory (each gauge configuration). We therefore want to solve this Green function for each kaon source time t_i, and then we perform a time translation average, since this Green function will only depend on how far the vertex and sink are separated from the source:

$$\#1^{tp1}(t_x, t_y, \Delta) = \sum_{t_i=0}^{T-1} \frac{\#1(t_i, t_i + t_x, t_i + t_y, t_i + \Delta)}{T}, \tag{4.4}$$

where T is the dimension of our lattice in the time-direction. When a point has crossed the time boundary, our periodic or anti-periodic boundary condition in the time direction will be applied. We note that the boundary condition are on the propagators, and when we have the product of two propagators, the minus sign from the anti-periodic boundary condition will cancel, so we end up can treat anti-periodic boundary condition the same as periodic boundary condition.

4.1.2 Random source propagators and sparsening

We have described in the previous section about how we obtain the type 1 and 2 four point functions. For the other types of four point functions, we will have to solve the vacuum polarization diagram, which we refer to the "self loop". It represent the propagator from a space-time source point x which ends at the same point. Since we cannot evaluate this for all source point x, and we cannot treat one vertex as a sink as we did in the type type 1 and 2 diagrams, we must find an efficient way to calculate these self-loop diagrams.

This can be accomplished by using the random source propagators. We define a set of N random vector η_i that have a random number at each space-time point, where $i = 1, 2, ...N$. Here N is the number of random vectors we use for each gauge configuration (number of random hits). The random vectors are choose such that

$$\langle \eta_i(x)\eta_i^\dagger(y)\rangle = \delta(x, y). \tag{4.5}$$

The angular bracket means are average over different random vectors and gauge configurations. The most obvious choice for the random vector is a vector of -1 and 1. We call these the Z_2 random numbers. We can imagine that when the number of random hits N gets large, Eq. 4.5 will be satisfied. We then solve the linear equation:

$$DS_i(x) = \eta_i. \tag{4.6}$$

The solution S will be the propagator from the random vector to any sink x. Specifically, we can write the solution from the above equation as:

$$S_i(x) = \sum_y \eta_i(y)S(x; y). \tag{4.7}$$

If we want to find the propagator from a specific point y to a sink x, we will have to multiply

the above quantity by the random source at y and then sum over all random vectors:

$$S(x;y) = \frac{1}{N}\sum_{i=1}^{N} S_i(x)\eta_i^\dagger(y). \tag{4.8}$$

To find the self loop that appears in the type 3 & 4 diagrams (Fig. 3.2), we can use:

$$S(x;x) = \langle S_i(x)\eta_i^\dagger(x)\rangle. \tag{4.9}$$

To show one example, we can look at contraction #1 of the type 3 four point functions in Fig. A.3 of Appendix A:

$$\begin{aligned}\#1^{tp3}(t_i,t_x,t_y,t_f) &= \sum_{\vec{x}}\sum_{\vec{y}} \mathrm{Tr}\left[\gamma_\mu(1-\gamma_5)S_d(x;t_i)S_s^\dagger(y;t_i)\gamma_5\gamma_\nu(1-\gamma_5)S_d(y;t_f)S_s^\dagger(x;t_f)\gamma_5\right] \\ &\quad \mathrm{Tr}\left[\gamma_\mu(1-\gamma_5)S(x;x)\right]\mathrm{Tr}\left[\gamma_\nu(1-\gamma_5)S(y;y)\right]\end{aligned} \tag{4.10}$$

However, if we simply apply Eq. 4.9 in the above formula, we will get an extra term that we don't want (ignoring the gamma matrices):

$$\begin{aligned}&\mathrm{Tr}\left[\frac{1}{N}\sum_{i=1}^{N} S_i(x)\eta_i^\dagger(x)\right]\mathrm{Tr}\left[\frac{1}{N}\sum_{i=1}^{N} S_i(y)\eta_i^\dagger(y)\right] \\ =\ &\frac{N(N-1)}{N^2}\mathrm{Tr}\left[S(x;x)\right]\mathrm{Tr}\left[S(y;y)\right] + \frac{1}{N^2}\sum_{i=1}^{N}\mathrm{Tr}\left[S_i(x)\eta_i^\dagger(x)\right]\mathrm{Tr}\left[S_i(y)\eta_i^\dagger(y)\right].\end{aligned} \tag{4.11}$$

We have the second term because we used the same set of random numbers for $S(x)$ and $S(y)$, and it is problematic because it can produce a term $\mathrm{Tr}\left[S_i(x;y)\right]\mathrm{Tr}\left[S_i(y;x)\right]$. Although this term is suppressed by $1/N$, it will make our results biased. One way to deal with it is to use different random numbers for $S(x)$ and $S(y)$, but this will increase the time cost by a factor of 2. (We now have to solve $2N$ propagators.) We therefore use another method: after we have calculated the contraction above in Eq. 4.10, we also calculate the contraction by

using the $S(x;x)$ and $S(y;y)$ only from the same random hit, which actually calculates the contribution of the second term. Then we subtract the contribution of this unwanted term. However, one difficulties is in Eq. 4.10, we only have to calculate this contraction once using the self loop at x and y both averaged from N random vectors, while we have to do this calculation for the unwanted term N times, each time using the self-loop both from random hit $i, (i = 1, 2, ..., N)$. Although the contraction is not as costly as solving for the propagators with CG, it will cost us some time. Fortunately, since this term is suppressed by a factor of $1/N$, we do not have to calculate it very precisely, and we can just do a small number of calculations (6 for example) and multiply it by a factor $(N/6)$ to obtain an estimate of this unwanted term.

Sparsening is a method that we might used to reduce the statistical noise from using the random source propagators. When we use a random volume source to calculate $S(x;x)$, we actually calculate $S(x;y)\eta(y)\eta^{\dagger}(x)$. This will converge to $S(x;x)$ when we average large number of random vectors. For a finite N, we will include a statistical noise from this term. To reduce this noise, some points y may be made to have a source 0, and therefore not to contribute to the noise. Because the quark propagator are suppressed for longer space-time separation, the most effective approach is to set the source to 0 for some points y close to x. This is the reasoning behind sparsening the random source vector. We define a sparsening factor M, such that we only have a single random point for each M^4 cube. If we have large M, we will have a smaller statistical error according to the mechanism discussed above. However we can then only obtain the $X(x;x)$ for V_{4D}/M^4 lattice sites for each inversion. If we fix the total number of hits N, the number of random vectors for each lattice site will be smaller by a factor of $1/M^4$, possibly increasing the error because of fewer sampling.

We have tested sparsening, and we compared some numerical results with or without sparsening when using the method of All-to-All propagators introduced in the following section. The results will be shown in the following section. We have chosen to perform a

random sparsening, where we randomly choose a single source point at each M^4 cube where we introduce a random source, and all other point inside the M^4 cube have source 0. If we don't choose the point have nonzero source randomly, then we will need to sample every point regularly in the M^4 cube in order to have unbiased results, and we will have to solve at least M^4 inversions with different random vectors, which can be very expensive for large M. Since our four-point functions will be a function of t_x, t_y, we choose to pick points regularly in the time direction, such that each time slice in the lattice has an equal amount of statistics. For each random vector $i, (i = 1, 2, ..., N)$, we choose a point in the M^4 cube:

$$x_0 = rand()\%M,\ y_0 = rand()\%M,\ z_0 = rand()\%M,\ t_0 = i\%M, \tag{4.12}$$

where each rand() represent an independent random integer. Then we will move this point periodically through the entire lattice, such that each point (x, y, z, t) satisfying the following condition will have a random source:

$$(x - x_0)\%M = 0,\ (y - y_0)\%M = 0,\ (z - z_0)\%M = 0,\ (t - t_0)\%M = 0. \tag{4.13}$$

4.1.3 Low mode deflation and All-to-All propagators

When we invert the Dirac operator to compute the quark propagator, we use an iteration method called Conjugate Gradient (CG). The final iteration number required to do this inversion will depend on a 'condition number' of the matrix D. The condition number is defined as the largest eigenvalue divided by the smallest. Therefore, for a larger quark mass m, the condition number will be smaller because the smallest eigenvalue will be large, while a smaller mass will be much harder to invert. In our measurement, solving for the charm quark propagator will be most efficient because of its heavy mass, while solving for the light quark propagator will be the most time consuming.

To accelerate the inversion of the light quark propagators, we can use the method of 'low

mode deflation'. We calculate N_e eigenvector with the smallest eigenvalues (the low modes) of the Dirac matrix, and project them out of the original Dirac matrix. Then we will be solving a easier problem because the condition number of the new matrix will be smaller. The reason we choose to find the smallest eigenvectors instead of the largest eigenvectors is because the distribution of eigenvalues is less dense when the eigenvalues are small. So deflating using the smallest eigenvectors will be more effective. The algorithm we use to find those eigenvectors are call the 'Lanczos algorithm'. It is originally used to find the largest eigenvalues and eigenvectors of a matrix. However, applying a 'Chebyshev filter', we can use it to find the smallest eigenvalues and the corresponding eigenvectors of the Dirac matrix. The 'Chebyshev filter' is a complicated polynomial of the Dirac Matrix, and it will suppress the larger eigenvalues and make the smaller eigenvalues larger.

When computing the light quark propagator for any source vector $|\eta\rangle$, the way we perform low mode deflation can be understood from the following equation ($|n\rangle$ is the nth eigenvector):

$$D^{-1}|\eta\rangle = \sum_{n=1}^{N_e} \frac{1}{\lambda_n}|n\rangle\langle n|\eta\rangle + D_{defl}^{-1}|\eta\rangle, \tag{4.14}$$

$$D_{defl} = D - \sum_{n=1}^{N_e} \lambda_n |n\rangle\langle n|. \tag{4.15}$$

We can solve all the light quark propagators using this low mode deflation method. For the self-loop propagators that involve the random sources to achieve a volume average, we use an improved method, called 'All-to-All' propagators (A2A)[16][17]. The reasoning is since we already have the low mode eigenvectors, we can find the low mode part of the self-loop accurately, without the use of random numbers. The All-to-All propagators for the self-loops are defined as follows:

$$S(x;x) = \sum_{n=1}^{N_e} \frac{1}{\lambda_n}\langle x|n\rangle\langle n|x\rangle + \langle x|D_{defl}^{-1}|\eta\rangle\eta^\dagger(x). \tag{4.16}$$

The noise from the random numbers enter only the high modes part, while the more important low mode parts will be accurate.

We have done a simple test of the A2A propagators on the $32^3 \times 64$ lattice we used in Chapter 6. We used 10 gauge configurations, and calculated the integrated correlator for the type 3 and type 4 diagrams. The result with error are shown in Fig. 4.1. We can see the errors are smaller by at least a factor of 2. We have done the calculation in Chapter 6 twice, the first time using random volume source with 60 hits. (Note the random number generator used in this first calculation had incorrect correlations. We believe these correlations do not significantly affect this comparison.) The second time we used A2A propagators and have observed a factor of 2 in the improvement of the error.

We also tested the method of sparsening. The benefit from sparsening will be less if we use A2A propagators. This is because the errors from the self-loop $S(x;x)$ using random source propagators are caused by the propagators from points y that are close to x, since such propagators are suppressed for longer source-sink separation by a factor related to the mass of lightest possible state (the pion state). If we used A2A propagators, this random propagator will have only the high modes part, correspond to states heavier than the pion. So these propagators from other source points y will fall off more rapidly than those which involve the pion state. Since sparsening is used to suppress the potential noise from such propagators, its benefit will be correspondingly less.

We have tested the effect of sparsening on the 32^3 lattice we used in Chapter 6 and the 64^3 lattice we used in Chapter 7. The results for different sparsening factor are shown in Table 4.1 and Table 4.2. In this test, we used only one gauge configuration, so that we do not have gauge noise. We ran the measurement a few times, each time with N_{hits} random hits and using different random numbers. Then we calculate the average and error from these of measurements, we can therefore see the statistical error only caused by the random numbers. The sparsening factor $N = 1$ corresponds to not using any sparsening, while for a

N larger than one we are using sparsening and for each random hit, we only have one source point in each N^4 cube. Since the two vertices in the integrated correlator are summed over space, we will expect a loss in the sample size of the self-loop propagators with sparsening, which is compensated by the self-loop propagator being measured more accurately. In those two tables, we do not see a benefit using sparsening. For the sparsening factor $N = 4$, the error is similar in size compared to no sparsening, while $N = 8$ and $N = 16$ is becoming worse. Therefore, we did not use sparsening in our calculation. However, sparsening might be useful in future calculations, especially if we do not have many eigenvectors to construct the A2A propagators.

	N=1	N = 4	N = 8	N = 16
type3 Q_1Q_1	-1.3341 ± 0.4000	-0.8633 ± 0.3044	-1.7596 ± 0.4136	1.6420 ± 6.5888
type3 Q_2Q_2	-1.5921 ± 0.3745	-2.1259 ± 0.5388	-2.5772 ± 0.7307	-10.1243 ± 4.6365
type3 Q_1Q_2	-1.4199 ± 0.2894	-1.7524 ± 0.3561	-1.9604 ± 0.3777	-4.9477 ± 4.8819
type3 Q_2Q_1	-1.4297 ± 0.4174	-1.3654 ± 0.2220	-1.7582 ± 0.5907	-0.0928 ± 6.6230

Table 4.1: Test for sparsening on the 32^3 lattice. We have computed the type 3 diagrams contribution to ΔM_K, which is less noisy. We have separated the contribution from the four different combinations of Q_iQ_j. We have done the measurements 5 times, each time with 64 random hits, and the error is calculated based on these 5 measurements. 550 eigenvectors are used in the A2A propagators.

	N=1	N = 4	N = 8
type3(pc)	-6.53 ± 0.99	-5.67 ± 0.72	-1.57 ± 3.04
type3(pv)	8.05 ± 1.49	7.67 ± 1.46	4.24 ± 2.89
type4(pc)	-3.79 ± 5.84	-2.14 ± 7.02	11.7 ± 9.9
type4(pv)	72.7 ± 78.8	32 ± 94	-31 ± 104

Table 4.2: Test for sparsening on the 64^3 lattice. We have computed the both the 3 diagrams and the type 4 diagrams contribution to ΔM_K. We separated the results by the parity conserving part and the parity violating part. We have done the measurements 6 times, each time with 24 random hits, and the error is calculated based on these 6 measurements. 2000 eigenvectors are used in the A2A propagators. Other aspects and the conclusions are the same as in Table 4.1.

4.1.4 All Mode Averaging

We also use all Mode Averaging (AMA) [18] to reduce the computational cost. In each measurement, the most time consuming part is solving the quark propagators with CG. The CG is an iterative method used to solve the linear equation $Dx = b$ and its cost depends on the final stopping condition we set. The stopping condition is defined as the norm of the difference between the vector DX^{sol} and the source vector b. A tight stopping condition will require that more iterations be done and therefore will cost more time, while a loose condition may require fewer iterations but the result might not be accurate. With AMA, we will use a looser stopping condition most of the time, and then use a tighter stopping condition to compute the same quantity (exact results) a few times and find the difference from the loose stopping condition results. We use this difference as a correction to the results from the loose stopping condition (the sloppy results). If the correction is very small or the error on the correction is very small, we can safely do the sloppy calculation for most of the time, and correct it at the end. However, if the error on the correction is very large, we cannot use AMA because we need a lot of measurements to calculate the correction precisely.

We used AMA in the 64^3 calculation of ΔM_K. on 5/6 of the configurations, and then do both the exact and sloppy calculation on about 1/6 of the configurations to find the correction. Then we use the super-jackknife method explained in Sec. 4.2.4 to combine those data. Before we performed the expensive 64^3 calculation of ΔM_K, we tested the effect of AMA on the 32^3 lattice. The cost of CG for different stopping condition are shown in Table 4.3. We tested the effect of using $1e-4$ and $1e-8$ as the stopping condition, and the integrated correlator for ΔM_K is plotted in Fig. 4.2, together with the difference between $1e-4$ and $1e-8$. We can see the difference (AMA correction) is very small and has small errors, so we can use $1e-4$ as the stopping condition for the CG, and then correct using $1e-8$ from only a few measurements. We also list the cost of CG with different stopping condition for the 64^3 lattice in Table 4.4.

stop residual	1e-3	1e-4	1e-8
strange wall src	226	375	945
light wall src	261	496	1321
light rand Src	72	280	1107
light point Src	91	319	1143

Table 4.3: CG iteration number with different stopping conditions on the 32^3 lattice. For the light quark, we have used low mode deflation with 550 eigenvectors to accelerate the CG.

.

stop residual	1e-4	1e-8
strange wall src	444	1162
light wall src	367	970
light rand Src	196	819
light point Src		805

Table 4.4: CG iteration number with different stopping conditions on the 64^3 lattice. For the light quark, we have used low mode deflation with 2000 eigenvectors to accelerate the CG.

.

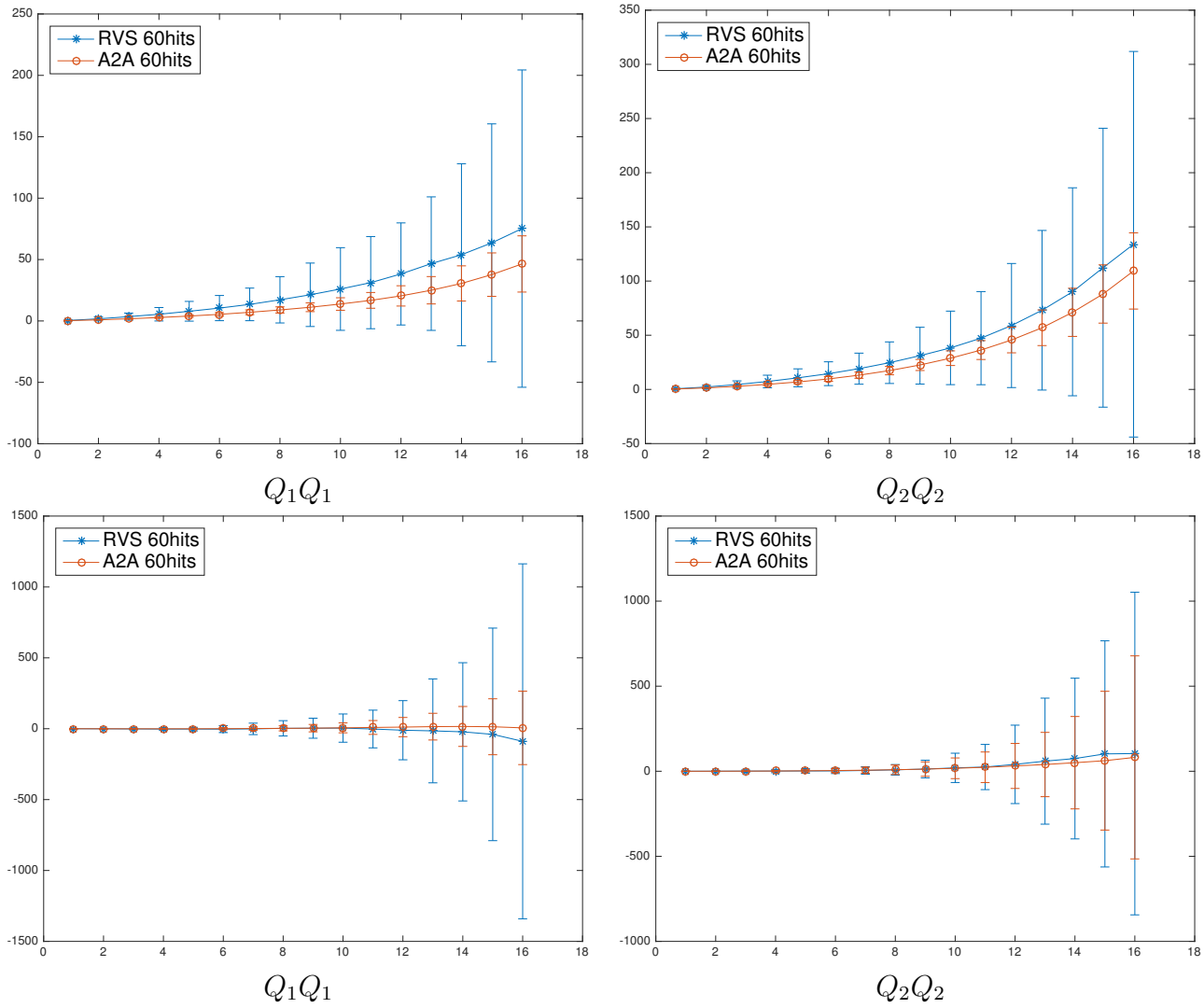

Figure 4.1: Type 3 and 4 (only parity conserving part) diagrams using random volume source compared to A2A propagators with 550 eigenvectors. Both with 60 random hits, an operators Q_1Q_1 or Q_2Q_2 at two vertices. On the top: type 3 diagrams, on the bottom: type 4 diagrams.

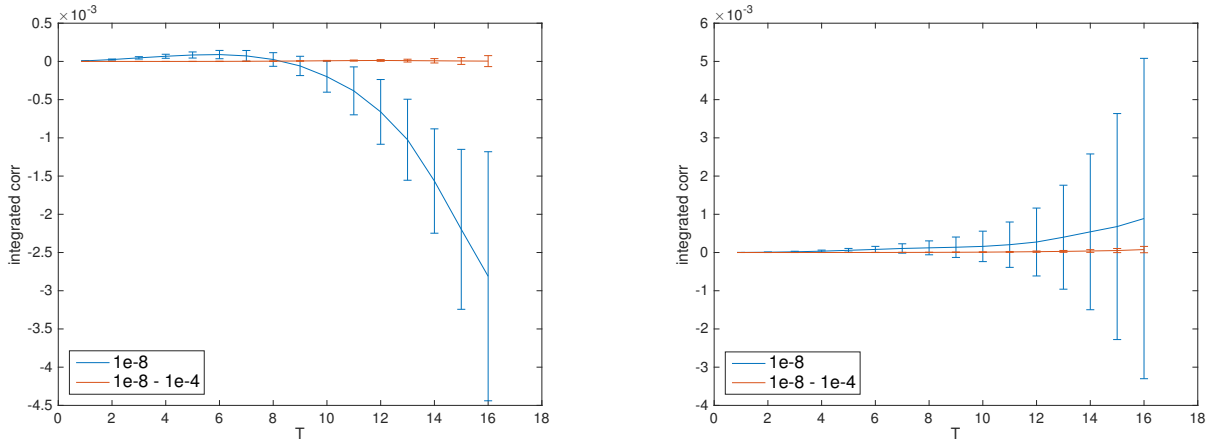

Q_1Q_1 Q_2Q_2

Figure 4.2: The integrated correlator for ΔM_K with different operator combinations. We plot the result from 6 configurations. The blue line is the correlator with a $1e-8$ stopping condition, and the red line is the difference between $1e-8$ and $1e-4$ stopping conditions.

4.2 Data analysis method

In this section, we discuss how we calculate the physical quantities from the Green functions we measured on the lattice. We'll discuss how we use the two-point function to find the meson energy, and how we find the kaon decay matrix element $\langle n|H_W|K^0\rangle$ from three point functions. Finally, we discuss how we fit the four point function to find the kaon mixing matrix element $M_{0\bar{0}}$.

4.2.1 Fitting the two point function and meson energy

Fitting the two point function will give us the meson energy we interested in. The two point functions we measure on the lattice are shown in Appendix A. To give an example, suppose we use a Coulomb gauge fixed wall source propagator for the kaon, then the operator we use for the kaon will be:

$$O_{K^0}(t) = \sum_{\vec{x},\vec{y}} i\bar{d}(\vec{x},t)V(\vec{x},t)\gamma_5 s(\vec{y},t)V(\vec{y},t). \tag{4.17}$$

We have a sum over 3D space because it is a wall source propagator. Here the V transform the gauge links in the spacial hyperplane at time t into Coulomb gauge. We then measure the two point correlation function $C(t)$:

$$\begin{aligned} C(t) &= \langle 0|O^\dagger_{K^0}(t)O_{K^0}(0)|0\rangle & (4.18)\\ &= \langle 0|e^{Ht}O^\dagger_{K^0}(t)e^{-Ht}O_{K^0}(0)|0\rangle & (4.19)\\ &= \sum_n \langle 0|O^\dagger_{K^0}(0)e^{-Ht}|n\rangle\langle n|O_{K^0}(0)|0\rangle & (4.20)\\ &= \sum_n |\langle n|O^\dagger_{K^0}(0)|0\rangle|^2 e^{-E_n t}. & (4.21) \end{aligned}$$

The sum over n is all the states generated by this operator. For large enough t, the above quantity will be dominated by the ground state, which is the single kaon state. Therefore,

we will measure the quantity $C(t)$ for various sink-source separation t, and then choose a fitting range such that t is sufficiently large to reduce the excited states, and then fit an exponential function to get the energy as well as the normalization factor $|\langle K^0|O^\dagger_{K^0}(0)|0\rangle$. However, since we have a finite size lattice, and if we used periodic or anti-periodic boundary condition for the quark propagators, we will have another term in the correlator $C(t)$, which is caused by a source located at $t = T$, where T is the dimension in time direction. Therefore, the above function will have another term $e^{-E_n(T-t)}$, and we correspondingly have to use a cosh function to fit the data.

4.2.2 Fitting three point functions with multiple source-sink separations

Fitting the three point function will give us the matrix element $\langle n|H_W|K^0\rangle$ we interested in. The intermediate state $|n\rangle$ can be the vacuum state, the single / double pion state, and the η state. We list all the three point diagrams we calculate in Appendix A. The kaon to pion and vacuum matrix element are less noisy since all the three point diagrams are connected, such as the #1 in the 3 point diagrams in Appendix A. The kaon to η matrix element will be very noisy since it includes disconnected diagrams, such as #29. The kaon to $\pi\pi$ state with isospin $I = 2$ matrix elements are also less noisy since it is all from connected diagrams, while the $I = 0$ state has contribution from disconnected diagrams. An example of connected $K \to \pi\pi$ diagram will be the #1 in the $K \to \pi\pi$ three point diagrams in Appendix A, while an example of disconnected diagrams will be #9.

Let's look at an simple example of calculating the kaon to single pion matrix element $\langle \pi^0|Q_i|K^0\rangle$, where Q_i is one of the operators we introduced in section 3.3. We define O_{K^0} as the operator to create a kaon and O_{π^0} as the operator to create a pion. We compute the following three point correlator, where Δ is the separation of the kaon source and the pion

sink, and t is the separation between the kaon and the weak operator Q_i.

$$\begin{aligned} C(\Delta,t) &= \langle 0|O^{\dagger}_{\pi^0}(\Delta)Q_i(t)O_{K^0}(0)|0\rangle & (4.22)\\ &= \sum_n\sum_m \langle 0|e^{H\Delta}O^{\dagger}_{\pi^0}(0)e^{-H\Delta}|n\rangle\langle n|e^{Ht}Q_i(0)e^{-Ht}|m\rangle\langle m|O_{K^0}(0)|0\rangle & (4.23)\\ &= \langle 0|O^{\dagger}_{\pi^0}|\pi\rangle\langle\pi|Q_i|K^0\rangle\langle K^0|O_{K^0}|0\rangle e^{-E_\pi(\Delta-t)}e^{-E_{K^0}t} & (4.24) \end{aligned}$$

We have dropped the excited states in the above formula. To find the matrix element $\langle\pi|Q_i|K^0\rangle$, we can fix the source-sink separation Δ, and use the two point functions to find the pion and kaon masses as well as their normalization factors. We divide by the normalization factors and the exponential terms, and then fit a plateau as we vary $t = 0, 1, ..., \Delta$, and we want to choose the fitting range of t such that it cannot be too close to the source or sink, in order to reduce the excited states contamination.

However, for some noisy matrix elements, such as those which involve the disconnected diagrams, we want to use a better method to reduce the error. For a disconnected diagram, such as the #29 in the 3 point diagrams in Appendix A, we can see the kaon and the weak operator are always connected by fermion lines, while the operator and the sink are disconnected. Therefore, the noise will increase if we increase the separation δ between the sink and operator ($\delta = \Delta - t$), while its less affected by the separation between the kaon source and the operator (t). We therefore want to measure multiple source-sink separation Δ and make use of more data points when the separation δ is small. We achieve this in the following way:

1. We measure $C(\Delta, t)$ for multiple Δ, and for each Δ, we measure this quantity for all possible t.

2. For each Δ, we use the meson mass and normalization factor to normalize the correlator $C(\Delta, t)$, and then we obtain the matrix element $\langle\pi|Q_i|K^0\rangle$. Although now this matrix element is theoretically independent of Δ and t, we know its more accurate for small δ and

less accurate for larger δ.

3. For each $\delta = 0, 1, ..., \Delta$, we find the error weighted mean of $\langle \pi | Q_i | K^0 \rangle$ measured for that δ. Meanwhile, we want to keep a minimum separation t_{min} from the kaon source and the operator to reduce excited states. We can imagine that for $\delta = 0$, we can find this average using the data of $\Delta = t_{min}, t_{min}+1, t_{min}+2, ..., \Delta_{max}$, and for $\delta = 1$, we can find this average using the data of $\Delta = t_{min}+1, t_{min}+2, ..., \Delta_{max}$. Therefore, for the smaller δ, the average is obtained using more data points.

4. Using the matrix element obtained above for different δ, we vary δ and fit a plateau. We should choose a reasonable fitting range of δ: the starting point should be large enough to reduce excited states, but not so large because the smaller δ give more accurate result.

In the above example, I used kaon to pion matrix element, but in reality this quantity is measured very accurately, and the above procedure is used to find $K \to \pi\pi$ matrix element and $K \to \eta$ matrix element.

4.2.3 Fitting four point functions with multiple source-sink separations

We calculate the four point function defined as follow:

$$\begin{aligned} G(t_f, t_2, t_1, t_i) &= \langle 0 | T \left\{ O_{K^0}(t_f) H_W(t_2) H_W(t_1) O_{K^0}(t_i) \right\} | 0 \rangle \\ &= |\langle K^0 | O_{K^0} | 0 \rangle|^2 e^{-M_K(t_f - t_i)} \sum_n \langle \bar{K}^0 | H_W | n \rangle \langle n | H_W | K^0 \rangle e^{(E_K - m_n)|t_2 - t_1|} \end{aligned} \tag{4.25}$$

Then we integrate t_1 and t_2 over the integration box with size T and fix the source-sink separation $t_f - t_i$ to get Eq. 3.18. We perform a time translation average so we sample all the possible t_i. We can use the two point function to find the kaon mass and normalize factor in Eq. 3.18, and then use the three point functions to find the matrix elements $\langle n | H_W | K^0 \rangle$ for all the intermediate states $|n\rangle$ that have energy lighter than or similar to the kaon, then

subtract their contribution to the exponential term in Eq. 3.18. Finally, we fit a linear function of T which gives us the final result for the long distance contribution for $M_{0\bar{0}}$, as defined in Eq. 3.15. Since we are performing a discrete sum, we drop the principal component $\mathcal{P}$.

However, we can use a better method to obtain more statistics like we did in the previous section. The reasoning is that for the four point functions, the type 4 diagrams (Fig. 3.2) have the largest error since the two operators are disconnected. We want to make use of more data when the two operator are close to each other in order to sample this quantity more precisely, and we can achieve this by using the data from more than one source-sink separation $t_f - t_i$. We perform the data analysis using the following steps:

1. Measure the time translated four point Green function $G(t_f, t_2, t_1, t_i)$. To reduce excited states contamination, we keep a minimum separation between each operator and the two kaons Δ_{min}. Since time translation has performed, this quantity will only depend on $t_f - t_i$, $t_1 - t_i$ and $t_2 - t_i$. We define $\Delta = t_f - t_i$, and call this quantity $G(\Delta, t_2, t_1)$, where t_1 and t_2 are now the relative separation from the source. We do the measurement for various values of Δ, and Δ should be always larger than or equal to $2\Delta_{min}$.

2. Normalize this quantity by dividing normalize factor and the exponential term $e^{-M_K(t_f-t_i)}$ in Eq 4.25. After we normalized this four point function, it only be a function of $\delta = t_2 - t_1$. We call this normalized four-point function $G(t_1, t_2)$, where t_1 and t_2 are the relative separation to the kaon source. We use the data for all possible Δ and find its error weighted average. For example, for $\delta = 0$, we can use the data for $\Delta = 2\Delta_{min}, 2\Delta_{min} + 1, ..., \Delta_{max}$, where Δ_{max} is the maximum Δ we measured. For $\delta = \pm 1$, we can use the data for $\Delta = 2\Delta_{min} + 1, 2\Delta_{min} + 2, ..., \Delta_{max}$. Therefore the smaller operator separation are averaged using more data point. After we perform this error weighted average, we get the four point function $G(\delta)$.

3. Find the integrated correlator $\mathcal{A}$:

$$\mathcal{A} = \sum_{t_1=0}^{T}\sum_{t_2=0}^{T} G(t_1,t_2) \tag{4.26}$$

$$= \sum_{\delta=-T}^{T} G(\delta)(T+1-|\delta|), \tag{4.27}$$

where the $(T+1-|\delta|)$ is a counting factor.

4. Proceed with the remaining previously described step: subtracting the exponential growing terms and then performing a linear fit.

We only use the above step for type 4 diagrams for two important reasons: The first is that the type 4 diagram is the only disconnected diagram that has very large error when the two operator separation are large, and the second being the computational cost. Measuring the four point function with all possible Δ is very costly, while it is free for the type 4 diagrams because we can save the left and right part separately, and then compute the contraction on workstation in the final analysis step. We can only do this for type 4 diagram because it can be separated in the following way:

$$G^{tp4}(t_f,t_2,t_1,t_i) = G^{left}(t_f,t_2)\times G^{right}(t_i,t_1). \tag{4.28}$$

4.2.4 Jackknife and super-jackknife

The jackknife method provides us with a convenient way to perform fitting of our data as well as estimating the statistical uncertainty from the fitting. A general discussion of jackknife and super-jackknife could be found in [19].

Suppose we have performed measurements from N configurations. We want to estimate parameter θ, such that the theoretical function $f(\theta,x)$ describes the observable $Y(x)$. In a simple example is x is the size of the integration box in Eq. 3.18, and $Y(x)$ is the integrated correlator, which should be a linear function of x. The parameter θ will be two dimensional,

and corresponds to the slope and intercept in the linear fit.

For each measurement $i(i = 1, 2, ..., N)$, we have measured $Y_i(x)$ for various value of x. We then define the jackknifed average $\bar{Y}_i(x)$:

$$\bar{Y}_i(x) = \frac{1}{N-1} \sum_{j \neq i} Y_j(x). \tag{4.29}$$

We then fit a parameter $\bar{\theta}_i$ for each jackknifed average $\bar{Y}_i$, and the mean of the parameter can be found using:

$$\hat{\theta} = \frac{1}{N} \sum_{i=1}^{N} \bar{\theta}_i, \tag{4.30}$$

with the uncertainty:

$$\sigma^2_{\hat{\theta}} = \frac{N-1}{N} \sum_{i=1}^{N} (\bar{\theta}_i - \hat{\theta})^2. \tag{4.31}$$

We note that the function $f(\theta, x)$ can correspond to multiple, complicated non-linear functions and we can obtain the parameter θ from a complex fitting method. The jackknife method will still work.

To find the $\bar{\theta}_i$ from each jackknifed block, we can perform a uncorrelated fit or a correlated fit. The uncorrelated fit will minimize the following quantity:

$$\chi^2_i = \sum_x \frac{\left[f(\bar{\theta}_i, x) - \bar{Y}_i(x)\right]^2}{\sigma^2(x)}, \tag{4.32}$$

$$\text{where } \sigma^2(x) = \sum_i \frac{\left[\bar{Y}_i(x) - \bar{Y}(x)\right]^2}{N}. \tag{4.33}$$

The above method will minimize an error weighted residual, but it does not take advantage of the correlation between different x. Since in one measurement, the value for $Y(x)$ and $Y(x+1)$ might be very correlated, we should prefer a fitting method that exploits this correlation.

The correlated fit will minimize the following quantity:

$$\chi_i^2 = \sum_{x,x'} \left[f(\bar{\theta}_i, x) - \bar{Y}_i(x)\right] \left[f(\bar{\theta}_i, x') - \bar{Y}_i(x')\right] C^{-1}(x, x'), \tag{4.34}$$

$$\text{where } C(x, x') = \frac{N-1}{N} \sum_i \left[\bar{Y}_i(x) - \bar{Y}(x)\right] \left[\bar{Y}_i(x') - \bar{Y}(x')\right]. \tag{4.35}$$

The C is the correlation matrix has the dimension of the vector x. In the above formula, we have used the same correlation matrix for each jackknife block i. This is called a frozen correlated fit and might not give a reliable jackknife estimate of the error. A consistent jackknife approach uses an unfrozen correlated fit with a different covariance matrix for each different jackknife block i:

$$C^i(x, x') = \frac{N-2}{N-1} \sum_{j \neq i} \left[\tilde{Y}_j^i(x) - \bar{Y}(x)\right] \left[\tilde{Y}_j^i(x') - \bar{Y}(x')\right], \tag{4.36}$$

$$\text{where } \tilde{Y}_j^i(x) = \frac{N\bar{Y}(x) - Y_i(x) - Y_j(x)}{N-2}. \tag{4.37}$$

After minimizing the χ^2, we can define the χ^2 per degree of freedom (χ^2/dof) as a test for the goodness for the fit. Usually, a χ^2/dof equal to one means we have represented the data well, a χ^2 too large means we are unable to represent the data well with our fitting function, and a χ^2 too small will indicate a potential over-fitting problem.

The super-jackknife method is used when we have more than one set of measurement. One example is when we perform the measurement for type 1&2 diagrams on one set of configurations, and we measure the type 3&4 diagrams in other set of configurations. We want to combine the data before we perform the fitting of parameter θ. In the super-jackknife method, suppose we have measured the observable Y_i on the first set of configurations $i = 1, 2, ..., N_1$, and we have measured another observable Z_i on another set of configurations $i = 1, 2, ..., N_2$. We want to estimate a parameter θ from some fitting method, and the result will depend on both Y and Z.

We combine the data into $N_1 + N_2$ measurements. In the first N_1 measurements, we use the regular jackknifed $\bar{Y}_i$, but use the mean value for Z. In the second N_2 measurements, we use the mean value for Y and the regular jackknifed value for Z:

$$\bar{Y}_i = \frac{1}{N_1 - 1} \sum_{j=1(j\neq i)}^{N_1} Y_j(x)\,, i = 1, 2, .., N_1, \tag{4.38}$$

$$\bar{Y}_i = \frac{1}{N_1} \sum_{j=1}^{N_1} Y_j(x)\,, i = N_1 + 1, .., N_1 + N_2, \tag{4.39}$$

$$\bar{Z}_i = \frac{1}{N_2} \sum_{j=1}^{N_2} Z_j(x)\,, i = 1, 2, ..., N_1, \tag{4.40}$$

$$\bar{Z}_i = \frac{1}{N_2 - 1} \sum_{j=1(j\neq i-N_1)}^{N_2} Z_j(x)\,, i = N_1 + 1, .., N_1 + N_2. \tag{4.41}$$

We then fit the parameter θ for each of those super-jackknifed blocks using the method described before and get $\bar{\theta}_i = \Theta(\bar{Y}_i, \bar{Z}_i)$, where the Θ stands for any complicated functions or fitting methods to get θ. The final estimation for parameter θ is given by:

$$\hat{\theta} = \frac{1}{N_1 + N_2} \sum_{i=1}^{N_1+N_2} \bar{\theta}_i, \tag{4.42}$$

with the uncertainty:

$$\sigma^2_{\hat{\theta}} = \frac{N_1 + N_2 - 1}{N_1 + N_2} \sum_{i=1}^{N_1+N_2} (\bar{\theta}_i - \hat{\theta})^2. \tag{4.43}$$

For the ΔM_K calculation on the 64^3 lattice, we have used All Mode Averaging (AMA) and we have measured the Green functions using a sloppy stopping condition CG on one set of configurations and the correction term, which is the difference between the Green functions from an accurate CG and a sloppy CG, on another set of configurations. If we call the sloppy Green functions A, and the correction term ΔA, we can use the method above to perform super-jackknife analysis. The function we fit will be a $A + \Delta A$. We therefore can define the χ^2 in the super-jackknifed data:

$$\chi_i^2 = \sum_{x,x'} \left[f(\bar{\theta}_i, x) - \left(\bar{A}_i(x) + \overline{\Delta A}_i(x)\right)\right] \left[f(\bar{\theta}_i, x') - \left(\bar{A}_i(x') + \overline{\Delta A}_i(x')\right)\right] C_i^{-1}(x, x'). \quad (4.44)$$

The covariance matrix will be calculated as the covariance matrix for $A + \Delta A$, which will be the sum of the covariance matrix for A and ΔA, based on the assumption of uncorrelated measurements. This can be shown as follows (we look at the simpler frozen case and ignoring $1/N$ effects):

$$\begin{aligned} C(t,t') &= \sum_{i=1}^{N_1+N_2} \left[\bar{A}_i(t) + \overline{\Delta A_i}(t) - \bar{A}(t) - \overline{\Delta A}(t)\right] \quad (4.45) \\ &\qquad \left[\bar{A}_i(t') + \overline{\Delta A_i}(t') - \bar{A}(t) - \overline{\Delta A}(t)\right] \\ &= \sum_{i=1}^{N_1} \left[\bar{A}_i(t) - \bar{A}(t)\right] \left[\bar{A}_i(t') - \bar{A}(t')\right] \quad (4.46) \\ &\qquad + \sum_{i=N_1+1}^{N_1+N_2} \left[\overline{\Delta A_i}(t) - \overline{\Delta A}(t)\right] \left[\overline{\Delta A_i}(t') - \overline{\Delta A}(t')\right] \\ &= C_A(t,t') + C_{\Delta A}(t,t'). \quad (4.47) \end{aligned}$$

One might think since ΔA is not varying among the first N_1 configurations and A is not varying among the last N_2 configurations, we should use only the covariance matrix for A in the first N_1 configuration and only the covariance matrix for ΔA for the last N_2. This is incorrect since we are fitting a function of $A + \Delta A$. In the first N_1 configurations, although ΔA is not varying among those N_1 configurations, it does contribute to the variance of the fitted function. Therefore, we also need to take its covariance matrix into consideration.

We note both the jackknife and super-jackknife method require that the measurements from different configurations are uncorrelated. In the case that we might have a correlation between our measurements (when we measure on Monte Carlo trajectories too close to each other), the jackknife and super-jackknife method might give an incorrect estimate for the

error. In these cases, binning the data before we perform the jackknife analysis is preferred.

Chapter 5

ϵ_K on the lattice

In this chapter, we first introduce how we perform the calculation for the long distance contribution to ϵ_K, and then we report the first lattice QCD calculation. While the short distance contribution to ϵ_K is accurately known, the long-distance part is only approximately estimated at $\approx 5\%$ of the total. The determination of this small but phenomenologically important contribution to ϵ_K is formulated as a problem suitable for lattice calculation and a complete exploratory calculation presented. This includes the consistent theoretical and numerical treatment of the logarithmic divergences that appear when such a calculation is performed using the effective four-Fermi theory required for a low-energy, lattice calculation. The exploratory calculation uses an unphysical light quark mass corresponding to a 339 MeV pion mass and an unphysical charm quark mass of 968 MeV, expressed in the $\overline{\text{MS}}$ scheme at 2 GeV. The necessary Wilson coefficients are determined to next-leading order (NLO) in QCD perturbation theory and all relevant diagrams are evaluated. This calculation demonstrates that future work, carried out using a smaller lattice spacing and larger physical volume, should determine this long distance contribution from first principles with a controlled error of 10% or less.

Different from the calculation of ΔM_K, ϵ_K is dominated by short distance contributions arising from the energy scale of the W boson or top quark masses with a long distance

contribution estimated to be only a few percent [20]. All previous calculations of ϵ_K involve integrating out the charm quark and treating the bi-local structure of the weak Hamiltonian as a local operator O_{LL} multiplied by a coefficient (Eq. 2.35), and then evaluating the matrix element $\langle \bar{K^0} | O_{LL} | K^0 \rangle$. We have summarized the conventional short distance calculation in NLO in section 2.3. This method does not allow us to control the systematic error from perturbation theory for the long distance, low energy part contribution. Previous calculations are summarized in section 2.4, where we see a 2.7σ discrepancy between the experimental value and the Standard Model (SM) prediction using the exclusive V_{cb}, and this discrepancy disappear when we use the inclusive value of V_{cb}. Currently the largest uncertainty of the SM prediction of ϵ_K comes from the value of V_{cb}. However, with more precise measurement of the input parameters, an accurate results for the long distance contribution becomes necessary in order to obtain more reliable SM prediction value.

Compared with the lattice QCD calculation of ΔM_K, we are expecting more difficulties here. First, because we are evaluating the imaginary part of the kaon mixing matrix element $M_{\bar{0}0}$, the top quark contribution can no longer be neglected. We therefore have to include all the QCD penguin operators in our calculation. Furthermore, all the diagrams we calculate will have a logarithm divergence which has a cutoff proportional to the inverse lattice spacing $1/a$, and this unphysical divergence has to be corrected in order to get a physical result. We don't have this difficulty in the ΔM_K calculation due to the "GIM mechanism" which makes all the diagrams finite. We correct the unphysical divergence using the "Rome-Southampton" method, in which we go to a Regularization Independent (RI) scheme by introducing an energy scale μ_{RI}, and then match to the perturbation theory calculation where everything is evaluated in the $\overline{MS}$ scheme. To be more concrete about our approach, we calculate the contribution below the energy scale μ_{RI} from the lattice, and this is achieved by using a non-perturbative method which removes the divergent part of the calculation with energy scale higher than μ_{RI} on the lattice. Then we do a continuum perturbative calculation which

involve energy scale from μ_{RI} up to the physical scale proportional to W boson mass. This perturbative calculation represents the effective Hamiltonian as a coefficient Y multiplied by a local operator O_{LL}. In the conventional short distance calculation, one performs a similar perturbative calculation treating the effective Hamiltonian that include all relevant energy scales as a coefficient Y_0 multiplied by a local operator O_{LL}. So we define a ΔY as the difference between our perturbative calculation and the conventional short-distance perturbative calculation, and then we present our results as a combination of three terms: the lattice calculation below μ_{RI}, the perturbative calculation involving ΔY, and the conventional short-distance calculation. We call the first two terms our "long distance correction" to ϵ_K. The scale μ_{RI} should be relatively large (compared to Λ_{QCD}), such that perturbation theory can work reliably, but not too large (compared to inverse lattice spacing $1/a$), such that we can control the lattice discretization error. After we have made this correction and combined the lattice calculation with the perturbative calculation, our final result should not depend on the artificial scale μ_{RI}, and this consistency check is performed at the end of this work.

This calculation is done on a $2+1$ flavor, $24^3 \times 64$ lattice, with the Domain Wall Fermion (DWF) action and the Iwasaki gauge action, and the inverse lattice spacing $1/a$ is 1.78 GeV. The pion mass is 339 MeV and the kaon is 592 MeV. We have included a valence charm quark with mass $m_c^{\overline{MS}}(2\text{ GeV}) = 968$ MeV. As we introduced in Section 3.3, we have five types of four point diagrams to calculate on the lattice. We use Coulomb gauge fixed wall source propagators for the two kaon sources, and a point source propagator at each time slice for the internal quark lines in the type 1&2&5 four point diagrams. For all of the self loops in type 3&4 four point diagrams, we use a random volume source propagator with 80 random hits for the high mode part, and 450 eigenvectors to construct low mode part of the self-loop. The eigenvectors are obtained from the Lanczos algorithm, which we run in double precision and then save them in single precision. By using this All-to-All style

propagator [16][17] for the self loop, the low mode part of the propagator will be exact, and the fluctuations from the random numbers will only occur in the high mode part. 200 gauge configurations are used in this analysis.

5.1 Lattice Evaluation of ϵ_K

As we have discussed in section 2.3, we use a different method to exploit the CKM unitarity than is conventionally done. We have defined the short distance Hamiltonian as in Eq. 2.36 and separated the contribution to three terms. We only have to perform a lattice calculation for the term proportional to $\lambda_u\lambda_t$.

Now we begin the discussion of the $\lambda_u\lambda_t$ contribution to $\mathrm{Im}\, M_{\bar{0}0}$. The term proportional to $\lambda_u\lambda_t$ in Eq. 2.36 is calculated by first integrating out the W boson and the top quark, resulting in a bi-local structure with two $\Delta S = 1$ operators. One then uses renormalization group running to run from the W boson scale down to the charm quark scale, with the charm quark as a active flavor. When performing the conventional short distance calculation, one then integrate out the charm quark and converts the bi-local structure to a local operator O_{LL} multiplied by the coefficients in Eq. 2.36. We note this procedure is not very reliable because the charm quark is not very heavy, and integrating out the charm quark must be performed at a scale well below the charm quark mass($\sim$ 1GeV), where perturbation theory become unreliable due to the large coupling α_s. Therefore, we perform a calculation which includes the charm quark as an active flavor, and this can be performed at a scale above the charm quark mass. Instead of integrating out the charm quark, we evaluate the bi-local structure resulting from two $\Delta S = 1$ weak Hamiltonians directly on the lattice. The term proportional to $\lambda_u\lambda_t$ has a $t-c$ propagator and a $u-c$ propagator in the two internal quark lines, and we can separate this structure into two parts: $t\times(u-c)$, and $c\times(c-u)$. The first part is short distance dominated due to the large mass of the top quark, and a perturbative calculation can give reliable results. However, there is a second QCD penguin contribution

which we include in our lattice calculation. The term with $c \times (c - u)$ has a long distance contribution because it does not have a very heavy flavor in either of the two internal quark lines, and we use lattice QCD to evaluate the bi-local structure at a scale above the charm quark mass. We begin with the Hamiltonian $H^{\Delta S=1}$ that change the strangeness by one.

$$H^{\Delta S=1} = \frac{G_F}{\sqrt{2}}\Big(\sum_{q,q'=u,c} V^*_{q',s}V_{q,d}\sum_{i=1,2} C_i Q_i^{q',q} - \lambda_t \sum_{i=3}^{6} C_i Q_i\Big) \tag{5.1}$$

The $Q_{1,2}$ are the current-current operators, and the $Q_{3,4,5,6}$ are the QCD penguin operators. They are introduced in section 3.3 We have dropped the electro-weak penguin operators. The current-current operators have the structure $Q_i^{q,q'}$, where q, q' can be any combination of the up quark and the charm quark. The QCD penguin operators involve a sum over all the relevant flavors in our calculation. The $V - A$ stands for a left-handed vertex, and $V + A$ stands for a right-handed vertex. To calculate a second order process, we integrate the product of two H_W over a time interval $[t_a, t_b]$, and obtain the integrated correlator as shown in Eq. 3.17. Then we perform the familiar process of inserting a complete set of intermediate states and obtain Eq. 3.18, from which explains how a linear fit to the integrated correlator and the use of Eq. 3.19 will determine the long distance contribution to $M_{\bar{0}0}$.

To fit $M_{\bar{0}0,ld}$ from our integrated correlator, we use the same method we used in the ΔM_K calculation [21] and [1]. We identify each intermediate state $|n\rangle$ that has energy less than the kaon, which results in an exponential increasing amplitude in the integrated correlator, and we explicitly remove its contribution. For the intermediate states that have energies higher than the kaon, our choice of integration region T is large enough that their contribution is exponentially suppressed. In this current analysis, where the two-pion state is heavier than the kaon, the only intermediate states that we need to consider are the single pion state and the vacuum state.

We note that in Eq. 3.17, we keep only the terms in the product of two H_W that have

a factor $\lambda_u\lambda_t$, and for the factor λ_c, we will use the unitary condition of the CKM matrix element and convert λ_c to $-\lambda_u - \lambda_t$. We then obtain the second order non-local weak Hamiltonian that change strangeness by two units given in Eq. 5.2. Its bi-local part is what we will use in Eq. 3.17. The T in Eq. 5.3 and Eq. 5.4 means time ordering.

$$H_{eff,ut}^{\Delta S=2} = \frac{G_F^2}{2}\lambda_u\lambda_t \sum_{i=1,2}\left\{\sum_{j=1}^{6} C_i C_j \sum_{x,y}[Q_i Q_j(x,y)] + C_{7i} O_{LL}\right\} \tag{5.2}$$

$$\begin{aligned}[Q_i Q_j(x,y)] &= \frac{1}{2}T\{2Q_i^{cc}(x)Q_j^{cc}(y) - Q_i^{uc}(x)Q_j^{cu}(y) - Q_i^{cu}(x)Q_j^{uc}(y) \\ &\quad -Q_i^{cc}(x)Q_j^{uu}(y) - Q_i^{uu}(x)Q_j^{cc}(y)\}, \quad (j=1,2)\end{aligned} \tag{5.3}$$

$$\begin{aligned}[Q_i Q_j(x,y)] &= \frac{1}{2}T\{[(Q_i^{cc}(x) - Q_i^{uu}(x)]\, Q_j(y) \\ &\quad +Q_j(x)\,[Q_i^{cc}(y) - Q_i^{uu}(y)]\}, \quad (j=3,...,6)\end{aligned} \tag{5.4}$$

The C_i $(i = 1, 2, ..., 7)$ are the Wilson coefficients. Note that when the two operators in $[Q_iQ_j(x,y)]$ are close to each other, we will have a logarithmic divergence, and the product is not well defined. The operator O_{LL} is a pure local operator and with a properly chosen coefficient will cancel this logarithmic divergence. We should note that the definition of O_{LL} is different from [10] and we absorb the additional factors to C_7. In the lattice calculation, we will also have a short distance, ultra-violet divergence when the $[Q_iQ_j(x,y)]$ are close to each other, and the high energy part is cutoff by a energy scale proportional to the inverse lattice spacing $1/a$. We must find a corresponding coefficient of the local operator O_{LL} to absorb the divergence from the lattice calculation, and this process is discussed in Section 5.2.

To calculate the long distance contribution to $M_{\bar{0}0}$, we will use bi-local structure of Eq. 5.2 in our integrated four point correlator Eq. 3.17, and we have five types of four point diagrams to calculate on the lattice. The type 1 and 2 diagrams are shown in Fig. 5.1. Note that if both of the two operators are current-current operators, we have a single charm quark propagator in one internal quark line, and a charm minus up propagator difference in the

other. If one of the operator is a current-current operator, and the other is a QCD penguin operator, we will have both internal quark lines with the charm quarks, minus the same diagram with both internal quark lines the up quarks. The type 3 and 4 diagrams are shown in Fig. 5.2. If both of the two operators are current-current operators, we have a single charm quark self-loop at one of the vertex and a charm minus up quark difference at the other. If one of the vertices is a QCD penguin operator, we have a single charm quark in one self-loop and a sum over all four flavors in the other self-loop. The type 5 diagrams are shown in Fig. 5.3. The type 5 diagrams are absent in the ΔM_K calculation, because one of the vertices of type 5 diagram must be a penguin operator. We have two types of type 5 diagram, emerging from the $(\bar{s}d)_{V-A}(\bar{d}d)_{V\pm A}$ operator or the $(\bar{s}d)_{V-A}(\bar{s}s)_{V\pm A}$ operator in the penguin operators $Q_{3,4,5,6}$.

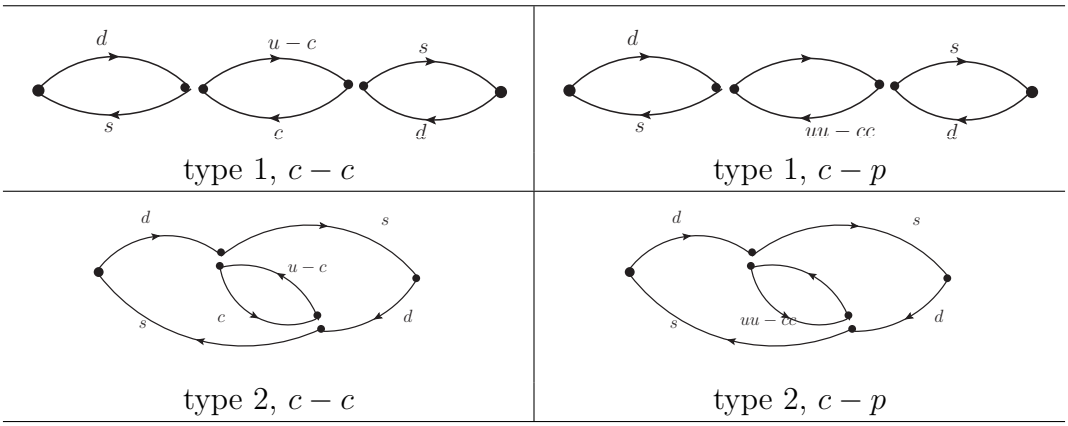

Figure 5.1: Type 1 and type 2 four point diagrams. The label c means a current-current operator, and p means a penguin operator.

In all of the five types of diagrams, we used a wall source propagator for the kaon. The two kaon wall sources have a fixed distance $\Delta_{KW} = 28$, and each of the two weak vertex has a minimum separation 6 from each wall, to reduce excited-state contamination. Therefore, when we integrate the two vertices, the size of the integration box T can go from 0 to 16. In the calculation of the type 1 and type 2 diagrams, we used a point source propagator at each time slice for one of the vertices, and the other vertex is summed over space-time volume as

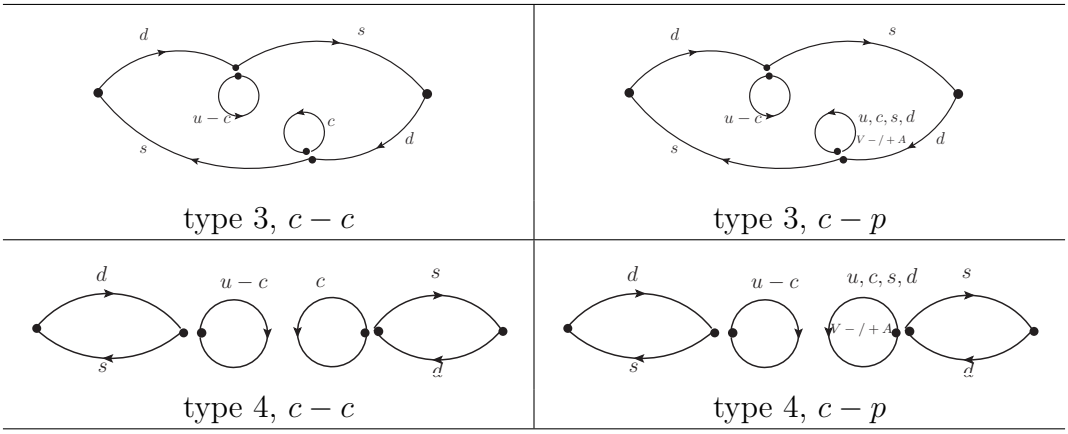

Figure 5.2: Type 3 and type 4 four point diagrams. The label c means a current-current operator, and p means a penguin operator.

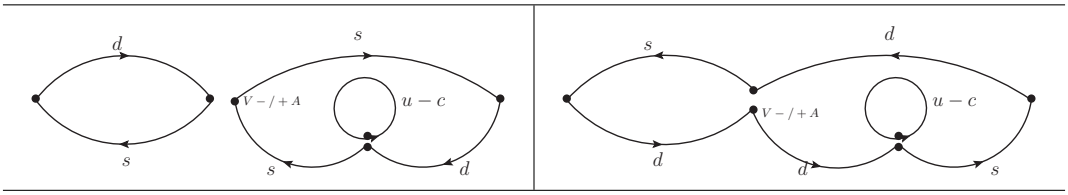

Figure 5.3: Type 5 four point diagrams. They have a current-current operator ar one vertex, and the other vertex must come from either a $(\bar{s}d)_{V-A}(\bar{d}d)_{V\pm A}$ operator or a $(\bar{s}d)_{V-A}(\bar{s}s)_{V\pm A}$ operator.

a sink. The point source are fixed at $(4t, 4t, 4t, t)$, where periodic boundary conditions are used when an (x, y, z) component go across the lattice boundary. Thus, we place the point source on the time slice t at the point $(4t \text{ mod } L, 4t\text{mod}L, 4t\text{mod}L)$.In the calculation of the type 3 and type 4 diagrams, we used All-to-All propagators for the self-loop. For the type 5 diagram, we used the same point source as we used for the type 1 and 2 diagrams for the self-loop, and the other vertex is treated as a sink for the four propagators and summed over the space-time integration box.

5.2 Short distance divergence

In the ϵ_K calculation, all of our type 1 and type 2 diagrams will have a logarithmically ultraviolet divergence. This can be illustrated if we compare the diagrams with the diagrams in

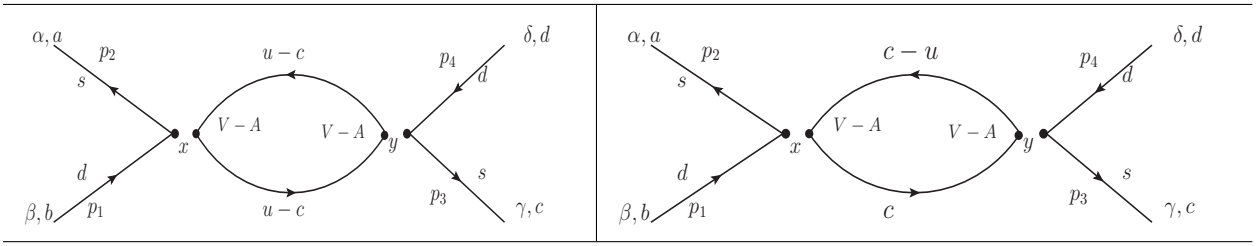

Figure 5.4: On the left: example diagram in ΔM_K calculation. On the right: Example diagram in ϵ_K calculation.

the ΔM_K calculation. We have shown two typical diagrams in Fig. 5.4. To study the ultra-violet behavior, we can ignore the momentum in the four external quark lines, and write down the free field propagator. The corresponding expression for the ϵ_K example diagram is given in Eq. 5.5, and the expression for the ΔM_K example diagram is given in Eq. 5.6,

$$\begin{aligned} &\int d^4p \gamma^\mu (1-\gamma^5)(\frac{\not{p}-m_c}{\not{p}^2+m_c^2} - \frac{\not{p}-m_u}{\not{p}^2+m_u^2})\gamma^\nu(1-\gamma^5)(\frac{\not{p}-m_c}{\not{p}^2+m_c^2}) \\ =&\int d^4p \gamma^\mu (1-\gamma^5)\frac{\not{p}(m_c^2-m_u^2)}{(\not{p}^2+m_u^2)(\not{p}^2+m_c^2)}\gamma^\nu(1-\gamma^5)(\frac{\not{p}}{\not{p}^2+m_c^2}). \end{aligned} \tag{5.5}$$

$$\begin{aligned} &\int d^4p \gamma^\mu (1-\gamma^5)(\frac{\not{p}-m_c}{\not{p}^2+m_c^2} - \frac{\not{p}-m_u}{\not{p}^2+m_u^2})\gamma^\nu(1-\gamma^5)(\frac{\not{p}-m_c}{\not{p}^2+m_c^2} - \frac{\not{p}-m_u}{\not{p}^2+m_u^2}) \\ =&\int d^4p \gamma^\mu (1-\gamma^5)\frac{\not{p}(m_c^2-m_u^2)}{(\not{p}^2+m_u^2)(\not{p}^2+m_c^2)}\gamma^\nu(1-\gamma^5)(\frac{\not{p}(m_c^2-m_u^2)}{(\not{p}^2+m_u^2)(\not{p}^2+m_c^2)}). \end{aligned} \tag{5.6}$$

By counting the power of momentum in Eq. 5.5, we can recognize the logarithmic ultra-violet divergence. On the other hand, the expression for the ΔM_K calculation is ultra-violet finite because we have subtracted charm from up quark in both quark lines. On the lattice, this ultra-violet divergence is cutoff the inverse lattice spacing $(1/a)$, and we should identify and correct this unphysical divergent piece to get physical results. We use the "Rome-Southampton" method [22] to perform the short distance correction. The short distance

part of our integrated correlator can be represented by a single local operator O_{LL} multiplied by some coefficient that we need to determine, and the steps we correct the divergence is illustrated by:

$$\mathcal{A} \rightarrow \mathcal{A} - \mathcal{A}_{SD}^{lat} + \mathcal{A}_{SD}^{cont}, \tag{5.7}$$

$$\mathcal{A}_{SD}^{lat} = \sum_{t=t_a}^{t_b} \langle \overline{K^0}(t_f) X O_{LL}(t) \overline{K^0}(t_i) \rangle. \tag{5.8}$$

$$\mathcal{A}_{SD}^{cont} = \sum_{t=t_a}^{t_b} \langle \overline{K^0}(t_f) Y O_{LL}(t) \overline{K^0}(t_i) \rangle. \tag{5.9}$$

The coefficient X represents the short distance part of our lattice calculation, which is unphysical, and we remove it in Eq. 5.7 and then add a coefficient Y to match to the continuum. To be more concrete, we define our intermediate, Regularization Independent (RI) scheme as follows:

$$[Q_i Q_j]^{RI} = Z_i^{lat \to RI}(\mu_{RI}, a) Z_j^{lat \to RI}(\mu_{RI}, a) \left\{ [Q_i Q_j]^{lat} - X^{i,j}(\mu_{RI}, a) O_{LL}^{lat} \right\}, \tag{5.10}$$

$$[Q_i Q_j]^{RI} = Z_i^{\overline{MS} \to RI}(\mu, \mu_{RI}) Z_j^{\overline{MS} \to RI}(\mu, \mu_{RI}) \left\{ [Q_i Q_j]^{\overline{MS}} - Y^{i,j}(\mu, \mu_{RI}) O_{LL}^{\overline{MS}} \right\}. \tag{5.11}$$

The RI scheme is defined by imposing an RI condition that these operator combinations vanish when inserted in a Landau gauge-fixed Green's function evaluated at off-shell momenta with a scale μ_{RI}. We find a different coefficient for each different operator combination $[Q_i Q_j]$. The coefficient $X^{i,j}(\mu_{RI}, a)$, when multiplied by the operator O_{LL} and subtracted converts the bi-local lattice operator into an RI-normalized operator. The coefficient $Y^{i,j}(\mu, \mu_{RI})$ corrects from RI to $\overline{MS}$. This step is similar to the method we used in the rare kaon calculations [23]. The coefficient $Y^{i,j}(\mu, \mu_{RI})$ should be calculated in perturbation theory, and we perform a Next Leading Order (NLO) calculation in this work. We note that the Leading Order (LO) in the ϵ_K calculation is a large logarithm ($\mathcal{O}(\ln \frac{\mu}{M_W})$), and the NLO will be of order $\mathcal{O}(1)$, or order $\mathcal{O}(\alpha_s \ln \frac{\mu}{M_W})$. In the calculation of $Y^{i,j}(\mu, \mu_{RI})$, we insert

an external momentum with energy scale μ_{RI}, and perform the integration in the internal quark lines and equate the bi-local operator Green's function with the Green's function containing the local operator O_{LL}. In the conventional calculation of ϵ_K [10], this calculation is also performed but at zero external momentum. We therefore define a quantity $\Delta Y^{i,j}$, which is the difference of $Y^{i,j}(\mu, \mu_{RI})$ evaluated at our off-shell momentum at μ_{RI}, minus the $Y^{i,j}(\mu, 0)$ evaluated at zero external momentum. The $\Delta Y^{i,j}(\mu_{RI}) = Y^{i,j}(\mu, \mu_{RI}) - Y^{i,j}(\mu, 0)$ is therefore a quantity that is both ultra-violet and infra-red finite in four dimensions, and is independent of the $\overline{MS}$ scale μ. The calculation of $\Delta Y^{i,j}$ is illustrated in Fig. 5.5.

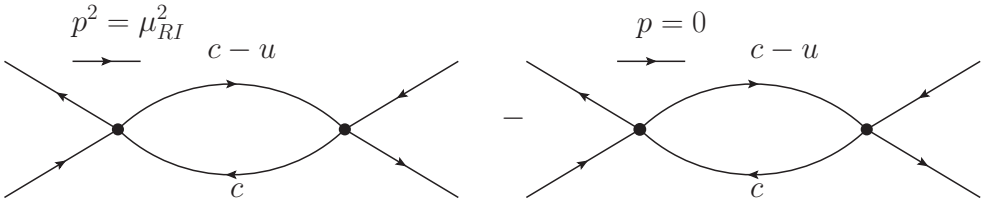

Figure 5.5: Illustration of the calculation of ΔY.

Finally, we can write our $\Delta S = 2$ effective Hamiltonian as follows

$$
\begin{aligned}
H_{eff,ut}^{\Delta S=2} \;=\; & \sum_{i=1}^{2}\sum_{j=1}^{6}\Big\{C_i^{lat}(\mu)C_j^{lat}(\mu)\left([Q_iQ_j]^{lat} - X^{i,j}(\mu_{RI})O_{LL}^{lat}\right) \\
& + C_i^{\overline{MS}}(\mu)C_j^{\overline{MS}}(\mu)\left[Y_{\overline{MS}}^{i,j}(\mu,\mu_{RI}) - Y_{\overline{MS}}^{i,j}(\mu,0)\right]Z^{lat\to\overline{MS}}O_{LL}^{lat} \\
& + \left[C_i^{\overline{MS}}(\mu)C_j^{\overline{MS}}(\mu)Y_{\overline{MS}}^{i,j}(\mu,0) + C_7^{\overline{MS}}(\mu)\right]Z^{lat\to\overline{MS}}O_{LL}^{lat}\Big\}.
\end{aligned}
\tag{5.12}
$$

The first line of Eq. 5.12 involve the lattice operators and the coefficient $X^{i,j}$ determined from non-perturbative renormalization (NPR). We call this term the "contribution below μ_{RI}", which include the long distance part, and use $\mathrm{Im}\, M_{\bar{0}0}^{ut,RI}(\mu_{RI})$ to denote its contribution to the kaon mixing matrix element. The C^{lat} are the lattice Wilson coefficients, which are obtained from the $\overline{MS}$ Wilson coefficients matched to those of the lattice operators. The second line involves the coefficient s $\Delta Y_{\overline{MS}}^{i,j}(\mu_{RI})$ calculated from perturbation theory, and we call this term "perturbative RI to $\overline{MS}$ correction", and use $\mathrm{Im}\, M_{\bar{0}0}^{ut,RI\to\overline{MS}}(\mu_{RI})$ to denote its

contribution to the kaon mixing matrix element. The last term is the conventional Standard Model calculation, and we call it the "conventional short distance result". The combination of the first two terms is our "long distance correction" to the SM calculation of ϵ_K, and it should be independent of the RI scale μ_{RI} we introduced, up to corrections of order $\mathcal{O}(\alpha_s)$ or higher.

To calculate the coefficient $X^{i,j}$, we need to perform a non-perturbative calculation, and this is achieved by introducing an external momentum μ_{RI} which should be relatively high compared to Λ_{QCD} and the charm quark mass m_c, computing the amputated Green's function (shown in Eq. 5.15) at this momentum scale, and then requiring the result to be zero after the subtraction of the Green's function of the local operator O_{LL} multiplied by the coefficient $X^{i,j}$ (shown in Eq. 5.16).

$$\left(\Gamma^{amp,i,j}_{\alpha,\beta,\gamma,\delta}(p) - X^{i,j}(\mu^2_{RI})\Gamma^{amp,SD}_{\alpha,\beta,\gamma,\delta}(p)\right) P_{\alpha,\beta,\gamma,\delta} = 0 \tag{5.13}$$

Here the $\Gamma^{amp,i,j}_{\alpha,\beta,\gamma,\delta}(p)$ is amputated Green's function with weak bi-local operator combination $[Q_iQ_j]$, and $\Gamma^{amp,SD}_{\alpha,\beta,\gamma,\delta}(p)$ is the amputated Green's function with the local operator $O^{\Delta S=2}_{LL}$. As is conventional, amputation means that we have removed the propagators corresponding to the four external legs. All of these are projected to a complex number using the the projection operator $P_{\alpha,\beta,\gamma,\delta}$, with the spin color structure:

$$P_{\alpha,\beta,\gamma,\delta} = \sum_{\mu}(\bar{s}_i(1-\gamma_5)\gamma_\mu d_i)_{\alpha,\beta}(\bar{s}_j(1-\gamma_5)\gamma_\mu d_j)_{\gamma,\delta} \tag{5.14}$$

$$\Gamma^{i,j}_{\alpha\beta\gamma\delta}(p) = \langle s_\alpha(p_1)\bar{d}_\beta(p_2)\int d^4x_1\int d^4x_2[Q_i(x_1)Q_j(x_2)]s_\gamma(p_3)\bar{d}_\delta(p_4)\rangle. \tag{5.15}$$

$$\Gamma^{\mathrm{SD}}_{\alpha\beta\gamma\delta}(p) = \langle s_\alpha(p_1)\bar{d}_\beta(p_2)\int d^4xO_{LL}(x)s_\gamma(p_3)\bar{d}_\delta(p_4)\rangle. \tag{5.16}$$

When the energy scale of the external momentum is high enough (compared to the charm mass), our integrated correlator will be purely dominated by short distance contributions.

We will test this statement in Section 5.3. Fig. 5.6 illustrates some example diagrams we used to determine this short distance correction. The diagram on the left represents the calculation of $\Gamma^{SD}_{\alpha,\beta,\gamma,\delta}$, using the local operator O_{LL}, and the diagram on the right represents the calculation of $\Gamma^{i,j}_{\alpha,\beta,\gamma,\delta}$, from two $\Delta S = 1$ operators. The diagram shown will correspond to the operator combination $Q_1 Q_1$ if both the vertices are $V - A$, and the internal quark lines are $c \times (c - u)$. The diagram will correspond to $Q_1 Q_3$ if both vertices are $V - A$, but the internal quark lines are $c \times c - u \times u$. The diagran will correspond to $Q_1 Q_5$ if it has one $V - A$ vertex and one $V + A$ vertex, and the internal quark lines $c \times c - u \times u$. We can also obtain the diagrams with the operators $Q_{2,4,6}$ by making one or both of the vertices color mixed.

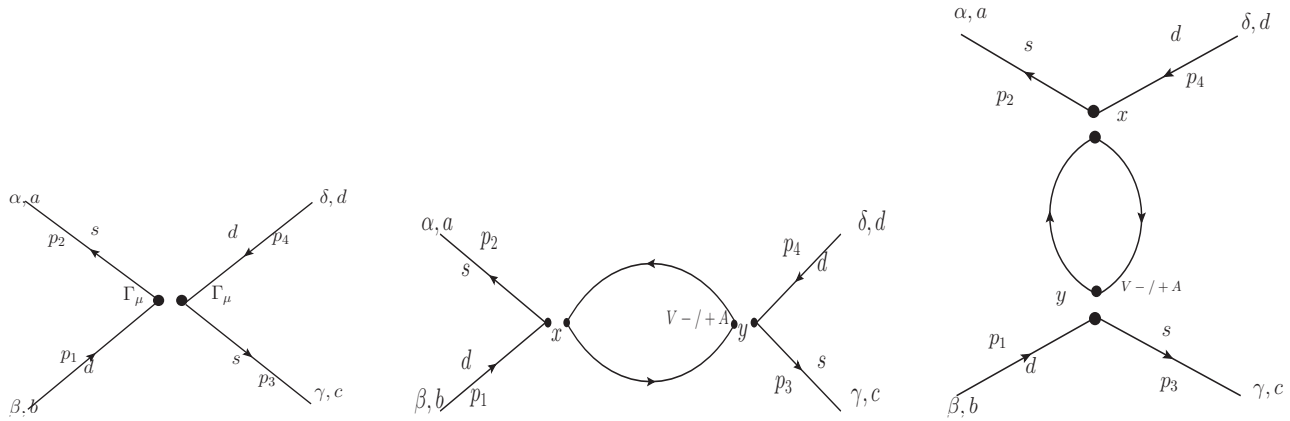

Figure 5.6: Some example diagrams that determine the short distance correction. The diagram on the left has the operator O_{LL}, and the two diagrams on the right have two $\Delta S = 1$ operators. Γ_μ stands for $\gamma_\mu(1 - \gamma_5)$ and V+/-A stands for $\gamma_\mu(1 \pm \gamma_5)$. The right hand vertex comes from operator $Q_{5,6}$.

We choose the momentum such that the total momentum flow is zero:

$$p_1 + p_4 = p_2 + p_3, \tag{5.17}$$

and all the momenta have the same energy scale μ_{RI}. Our choice of the momentum has the

form:

$$
\begin{aligned}
p_1 &= \frac{2\pi}{La}(M, M, 0, 0) \\
p_2 &= \frac{2\pi}{La}(M, 0, M, 0) \\
p_3 &= \frac{2\pi}{La}(0, M, 0, M) \\
p_4 &= \frac{2\pi}{La}(0, 0, M, M).
\end{aligned}
\tag{5.18}
$$

When M is not an integer, we use twisted boundary conditions to get the fermion propagator with non-lattice momentum.

We have done a similar study for the other three types of diagrams with four external quark lines. However, their short distance divergence is much smaller than that of the type 1&2 diagrams and is consistent with 0 within statistical errors. Therefore, we perform this short distance correction only for the type 1&2 diagrams.

5.3 Numerical results

Before we present the numerical results from our lattice calculation, we will give a brief introduction to how we define our operators on the lattice and their corresponding Wilson coefficients. We can find the $\overline{MS}$ value of the Wilson coefficients by using Eq. (12.43) - Eq. (12.61) in [10]. The strong coupling α_s is evaluated using Eq. (3.19) in [10]. To get the Λ_{QCD}, we use $\alpha_s(M_Z) = 0.1184$ to find Λ^5_{QCD} in five flavor theory, and then by requiring $\alpha_s(M_b)$ to be the same evaluating in five flavor theory and four flavor theory, we can find the Λ^4_{QCD} in four flavor theory. The input parameters are summarized in Table 5.1, and Λ^4_{QCD} and α_s are summarized in Table 5.2. We renormalize our operators at 2.15 GeV and the six Wilson coefficients are listed in Eq. 5.19.

m_t	M_W	M_Z	$\alpha_s(M_Z)$	m_b
172.2 GeV	80.4 GeV	91.1876 GeV	0.1184	4.19 GeV

Table 5.1: Input parameters for the evaluation of Wilson coefficients.

$\alpha_s(m_b)$	$\alpha_s(\mu)$	Λ^5_{QCD}	Λ^4_{QCD}
0.2265	0.2974	231 MeV	330 MeV

Table 5.2: The value for α_s for different energy scale and Λ_{QCD} with different active flavors.

$$C^{\overline{MS}}(2.15\text{ GeV}) = (-0.2967, 1.1385, 0.0217, -0.0518, 0.0102, -0.0671). \tag{5.19}$$

Note that for the current-current operators $Q_{1,2}$, we have multiple flavor structure depending on qq'. However, operators with different flavor structure have the same Wilson coefficients, and hence a common value for both C_1 and C_2. By requiring

$$\sum_{i=1}^{6} C_i^{\overline{MS}} Q_i^{\overline{MS}} = \sum_{i=1}^{6} C_i^{lat} Q_i^{lat}, \tag{5.20}$$

and applying the non-perturbative renormalization (NPR) procedure described in the appendix, with an intermediate $(\gamma_\mu, \not{q})$ scheme at the same energy scale, we can find the six lattice Wilson coefficients C^{lat} given in Eq. 5.19, where the numbers in the parenthesis are the statistical errors.

$$C^{lat} = (-0.2219(1), 0.6448(2), 0.0134(8), -0.0266(11), 0.0103(9), -0.0302(9)) \tag{5.21}$$

5.3.1 Evaluation of X

To correct the unphysical short distance divergence present in our lattice calculation, we must calculate the short distance artifact represented by $X(\mu_{RI})$ from the lattice. Our method to

correct the short distance artifact rely on the statement that the major contribution of our integrated correlator will be come from the short distance part, when the external momenta have a scale relatively high compared to the charm quark mass. To test the correctness of this statement, in our calculation of $X(\mu_{RI})$, we can introduce space-time cutoff R for the integration, such that when we do the summation over the position of both vertices in Eq.5.15, we only sum the points x_1, x_2 that satisfy $(x_1 - x_2)^2 \leq R^2$. The amputated Green's function will now depend on the cutoff R, as shown in Eq. 5.22.

$$\Gamma^{R,i,j}_{\alpha\beta\gamma\delta}(p) = \langle s_\alpha(p_1)\bar{d}_\beta(p_2) \int_{(x_1-x_2)^2\leq R^2} d^4x_2 d^4x_1 Q_i(x_1)Q_j(x_2)s_\gamma(p_3)\bar{d}_\delta(p_4)\rangle. \tag{5.22}$$

We then use Eq. 5.13 to find the $X^{i,j}$ for different cutoff radii R and different operator combinations. The results are shown in Table 5.3 for an external momentum scale $\mu = 1.41$ GeV. We have dropped the statistical errors because they are very small in this calculation. We can see that for $R \geq 5$, the results are very close to those without the cutoff, indicating a very small contribution from large distances. This conclusion will become stronger at larger momentum.

cutoff	3	4	5	6	7	none
$X^{1,1}$	-0.0491	-0.0530	-0.0534	-0.0533	-0.0533	-0.0533
$X^{1,2}$	-0.0240	-0.0254	-0.0255	-0.0254	-0.0254	-0.0254
$X^{2,2}$	-0.0140	-0.0148	-0.0148	-0.0148	-0.0148	-0.0148
$X^{1,3}$	-0.1098	-0.1222	-0.1237	-0.1233	-0.1229	-0.1226
$X^{1,4}$	-0.0258	-0.0275	-0.0275	-0.0274	-0.0273	-0.0272
$X^{1,5}$	0.1340	0.1370	0.1371	0.1372	0.1374	0.1375
$X^{1,6}$	0.0547	0.0561	0.0561	0.0562	0.0564	0.0567
$X^{2,3}$	-0.0258	-0.0275	-0.0275	-0.0273	-0.0273	-0.0273
$X^{2,4}$	-0.0302	-0.0324	-0.0325	-0.0323	-0.0322	-0.0322
$X^{2,5}$	0.0357	0.0364	0.0364	0.0364	0.0364	0.0363
$X^{2,6}$	0.0444	0.0451	0.0451	0.0451	0.0451	0.0448

Table 5.3: $X^{i,j}$ for different space-time cutoff, with operator combination $Q_{i,j}$. The external momentum has scale $\mu = 1.41$ GeV.

By summing over these coefficient multiplied by the lattice Wilson coefficients, we can find $X(\mu_{RI})$ for each of our different choices of momentum scale μ_{RI}. To obtain results with a non-integer momentum, we have used twisted boundary conditions. We show the quantity $X(\mu_{RI}) = \sum_{i,j} C_i^{lat} C_j^{lat} X^{i,j}(\mu_{RI})$ in Table 5.4. Because this is a logarithm divergence, we can fit the result $X(\mu_{RI})$ to a logarithm function of energy scale μ_{RI}. The fitted results are shown in Fig. 5.7. Our momentum range is limited on this lattice ensemble with $1/a = 1.78$ GeV, because a energy scale that is too high will introduce large discretization errors. So a linear fit might also well represent this relationship.

μ (GeV)	1.47	1.54	1.60	1.67	1.73	1.79	1.86	1.92	1.99
$X(\times 10^{-3})$	-5.5788	-5.3028	-5.0661	-4.8582	-4.6607	-4.4588	-4.2453	-4.0362	-3.8439
μ (GeV)	2.05	2.11	2.18	2.24	2.31	2.37	2.43	2.50	2.56
$X(\times 10^{-3})$	-3.6596	-3.4741	-3.2959	-3.1340	-2.9859	-2.8489	-2.7225	-2.6045	-2.4904

Table 5.4: Values of X for different momentum scales μ. The results have been multiplied by the Wilson coefficients. We have dropped statistical errors because they're less than 1%.

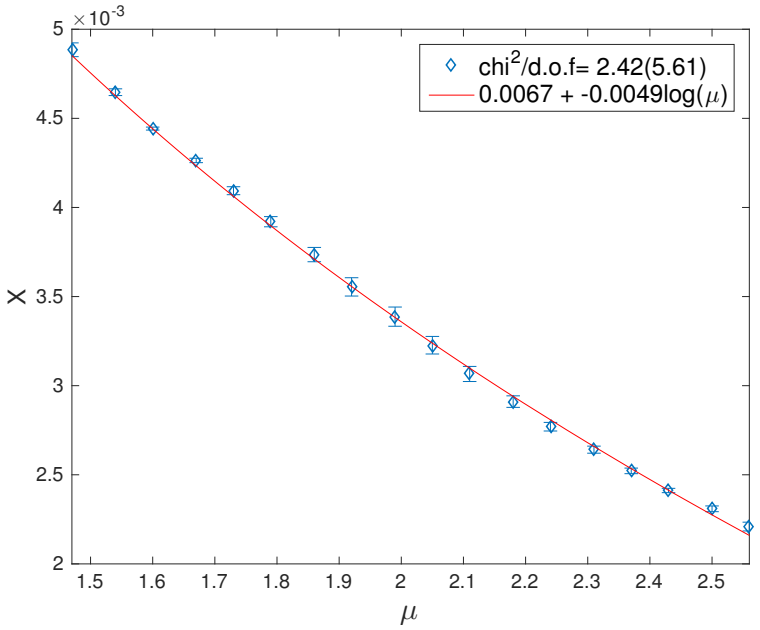

Figure 5.7: The fitted results for $X(\mu_{RI})$, as a function of momentum scale μ from 3 gauge configurations. An uncorrelated logarithm fit is performed.

5.3.2 Evaluation of Y

As explained earlier, instead of evaluating $Y(\mu, \mu_{RI})$, which depends on both the $\overline{MS}$ scale μ and the RI scale μ_{RI}, we evaluate the $\Delta Y(\mu_{RI})$. The quantity $\Delta Y(\mu_{RI})$ is ultra-violet convergent in dimension four, enabling us to simply perform the one loop calculation in perturbation theory without the use of dimensional regularization and the introdution of the scale μ. The calculation of $Y(\mu, 0)$ with zero momentum on the external legs can be found in [10], and we have listed the result in Eq. 5.23 - Eq. 5.27, where μ is the $\overline{MS}$ scale introduced when the dimensional regularization is performed. We have made some modification of these formulae so that we can use it in our charm quark subtraction case. We note that in our NLO calculation, we do not need to take the scale dependence of the charm quark mass into consideration. This is because that scale dependence is of order $\mathcal{O}(\alpha_s)$, while our NLO calculation is only accurate to order $\mathcal{O}(\alpha_s) \ln \frac{\mu}{M_W}$. So we use a fixed charm quark mass, given by our lattice input quark mass (0.363) converted to $\overline{MS}$: $m_c = 0.363 \times 1.78 \times 1.498 = 968$ MeV, where 1.78 is the inverse lattice spacing, 1.498 is the mass renormalization factor $Z_m^{lat \to \overline{MS}}(2\text{GeV})$ taken from [24], and 0.363 is the input lattice charm quark mass.

$$Y^{i,j}(\mu, 0) = \frac{m_c^2}{8\pi^2} r_{i,j}(\mu) \tag{5.23}$$

$$r_{i,j} = \begin{cases} (-4\ln(\mu/m_c) + 2)\tau_{i.j}, & j = 1, 2, \\ (-8\ln(\mu/m_c) + 4)\tau_{i.j}, & j = 3, 4, \\ (8\ln(\mu/m_c) - 4)\tau_{i.j}, & j = 5, 6, \end{cases} \tag{5.24}$$

$$\tau_{1,1} = \tau_{1,3} = \tau_{1,5} = 3 \tag{5.25}$$

$$\tau_{1,2} = \tau_{1,4} = \tau_{1,6} = 1 \tag{5.26}$$

$$\tau_{2,j} = 1, \text{ for any j.} \tag{5.27}$$

The result for $\Delta Y(\mu_{RI})$ is given in Eq. 5.28 - Eq. 5.32. We have done this calculation in two ways: one is to analytically perform the Fyenman integral over the internal quark loop, and the other is to do a numerical calculation, using the same projector as in Eq. 5.13. We have checked that they give the same result with the same the values for μ_{RI} and m_c. Also this final result will only depend on the energy scale of the external momentum μ_{RI}, independent of how we arrange the four component of the four external momentum in Eq. 5.18, as long as they have the same energy scale and the momentum conservation Eq. 5.17 is satisfied.

$$\Delta Y^{i,j}(\mu_{RI}) = \frac{m_c^2}{8\pi^2}\Delta r_{i,j}(\mu_{RI}) \tag{5.28}$$

$$\Delta r_{i,j} = \begin{cases} \left[\frac{\mu_{RI}^2+m_c^2}{m_c^2} \times c(m_c,\mu_{RI}) - b(m_c,\mu_{RI}) - 1\right]\tau_{i.j}, & j=1,2, \\ -\left[\frac{\mu_{RI}^2}{m_c^2} \times d(m_c,\mu_{RI}) + 2\times b(m_c,\mu_{RI})\right]\tau_{i,j}, & j=3,4, \\ 4b(m_c,\mu_{RI})\tau_{i.j}, & j=5,6, \end{cases} \tag{5.29}$$

$$b(m_c,\mu_{RI}) = \int_0^1 \mathrm{dx} \ln \frac{m_c^2}{x(1-x)\mu_{RI}^2 + m_c^2} \tag{5.30}$$

$$c(m_c,\mu_{RI}) = \int_0^1 \mathrm{dx} \ln \frac{x(1-x)\mu_{RI}^2 + m_c^2}{x(1-x)\mu_{RI}^2 + (1-x)m_c^2} \tag{5.31}$$

$$d(m_c,\mu_{RI}) = \int_0^1 \mathrm{dx} \ln \frac{x(1-x)\mu_{RI}^2}{x(1-x)\mu_{RI}^2 + m_c^2} \tag{5.32}$$

We also show the numerical values of $\Delta Y(\mu_{RI})$ in Table 5.5, for the same set of energy scales we used to calculated the $X(\mu_{RI})$. The values shown are multiplied by the $\overline{MS}$ Wilson coefficients $\Delta Y(\mu_{RI}) = \sum_{i,j} C_i^{\overline{MS}} C_j^{\overline{MS}} \Delta Y^{i,j}(\mu_{RI})$. We note that these values and the values for $X(\mu_{RI})$ in Table 5.4 are not directly comparable because the $X(\mu_{RI})$ are multiplied by a lattice operator while the $\Delta Y(\mu_{RI})$ are multiplied by an $\overline{MS}$ operator.

μ (GeV)	1.47	1.54	1.60	1.67	1.73	1.79	1.86	1.92	1.99
$\Delta Y(\times 10^{-2})$	2.3032	0.9698	1.1117	1.2425	1.4059	1.5552	1.7132	1.9086	2.3032
μ (GeV)	2.05	2.11	2.18	2.24	2.31	2.37	2.43	2.50	2.56
$\Delta Y(\times 10^{-3})$	2.4993	2.7043	2.9547	3.1790	3.4520	3.6956	3.9481	4.2541	4.5260

Table 5.5: Numerical value for $\Delta Y(\mu_{RI})$, at the same scale we evaluate $X(\mu_{RI})$.

5.3.3 Fitting results for ϵ_K

We have measured all the five types of four point functions on the lattice. Similar to what we have done in [21], for the four point correlator, we compute separately the parity conserving part and the parity violating part. This is achieved by separating the spin structure of each of the two vertices into the part that conserves parity and the part that violates parity. We have $(V-A)\times(V-A) = (VV+AA)-(AV+VA)$, and $(V-A)\times(V+A) = (VV-AA)+(VA-AV)$, where V means a γ_μ vertex and A means a $\gamma_\mu\gamma_5$ vertex. The AA and VV structures conserve parity while the AV and VA violate parity. For the parity conserving part, we have an intermediate state of single pion that is lighter than the kaon, and for the parity violating part, we have an intermediate vacuum state that is lighter than the kaon. We note that the single pion states exist in type 1,3,4,5 diagrams and the vacuum state only contribute to the type 4 diagrams. We can sum over all the five types of diagrams and then perform a subtraction of the lighter than kaon intermediate state, or we can do an intermediate state subtraction for each type of diagram and then combine them. We note that the second approach is much harder because we have to figure out the single pion contribution to each type of diagram independently. So in our final result, we use the first approach while if we want to show how each type of diagram contribute, we have to use the second approach.

After subtracting the intermediate states that are lighter than the kaon from our integrated correlator, we can do a linear fit versus the integration box length T. We show the fitting of the type 1 plus type 2 diagrams in Fig. 5.8 and Fig. 5.9. We plot both the integrated correlator before we subtract the pion state, and after the subtraction of the single

pion state, and also after the subtraction of both the single pion state and the unphysical short distance part determined by coefficient $X_{i,j}$. We list the contribution to $\mathrm{Im}\, M_{\bar{0}0}$ from each operator combination. The contribution before we remove the short distance divergence part is shown in Table 5.7, and the contribution after we remove the short distance divergence part is shown in Table 5.8. We note that the imaginary part comes only from the λ_t, because all our Wilson coefficients and λ_u are real. We correct the short distance divergence using $X_{i,j}$ determined with external momentum scale $\mu_{RI} = 2.11$ GeV, and the $X_{i,j}$ is given in Table 5.6.

$X^{1,1}$	$X^{1,2}$	$X^{1,3}$	$X^{1,4}$	$X^{1,5}$	$X^{1,6}$
0.0374	0.0183	0.0818	0.0193	-0.1092	-0.0432
	$X^{2,2}$	$X^{2,3}$	$X^{2,4}$	$X^{2,5}$	$X^{2,6}$
	0.0101	0.0196	0.0214	-0.0310	-0.0359

Table 5.6: $X^{i,j}$ calculated using the external momentum scale $\mu = 2.11$ GeV, in lattice units. In the calculation of $X^{i,j}$, we only calculate $i < j$, since he value for $X^{i,j}$ with $i > j$ is the same and included in these coefficients.

Q_1Q_1	Q_1Q_2	Q_1Q_3	Q_1Q_4	Q_1Q_5	Q_1Q_6
	Q_2Q_2	Q_2Q_3	Q_2Q_4	Q_2Q_5	Q_2Q_6
-0.629(0.007)	0.795(0.011)	0.131(0.006)	-0.013(0.002)	-0.077(0.005)	0.175(0.008)
	-2.054(0.030)	-0.020(0.002)	0.261(0.010)	0.010(0.002)	0.116(0.017)

Table 5.7: Imaginary part of $M^{ut}_{\bar{0}0}$, before the subtraction of the short distance divergent part, with all the Wilson coefficients multiplied. We have included only type 1 and type 2 diagrams. All numbers are in units of 10^{-15} MeV.

Q_1Q_1	Q_1Q_2	Q_1Q_3	Q_1Q_4	Q_1Q_5	Q_1Q_6
	Q_2Q_2	Q_2Q_3	Q_2Q_4	Q_2Q_5	Q_2Q_6
-0.385(0.007)	0.445(0.010)	0.099(0.005)	0.002(0.002)	-0.042(0.003)	0.135(0.007)
	-1.505(0.029)	0.003(0.002)	0.214(0.008)	-0.019(0.002)	0.213(0.017)

Table 5.8: Imaginary part of $M^{ut}_{\bar{0}0}$, after the subtraction of the short-distance, divergent part, with all the Wilson coefficients multiplied. We have included only type 1 and type 2 diagrams. All numbers are in units of 10^{-15} MeV.

Then we combine all five types of diagrams, we have larger statistical errors because of the disconnected diagrams. For the parity violating part of our integrated correlator, we have used a pseudo-scalar operator $\bar{s}\gamma_5 d$ to subtract the vacuum intermediate state. For the parity conserving part, we choose to use a scalar operator $\bar{s}d$ to subtract the pion intermediate state. We find the coefficients c^s and c^p by requiring the new operator $Q'_i = Q_i - c_i^s \bar{s}d - c_i^p \bar{s}\gamma_5 d$ gives a zero matrix element for kaon to vacuum $\langle 0|Q'|K^0\rangle$ and kaon to single pion $\langle \pi|Q'|K^0\rangle$. We can make this choice because the scalar operator and pseudo-scalar operator can be written as a divergence of a current, and any physical process that is on-shell will not be changed by adding these two operators. Thus, we find c^s and c^p by using Eq. 5.33 and Eq. 5.34.

$$\langle \pi|Q_i - c_i^s \bar{s}d|K^0\rangle = 0 \tag{5.33}$$

$$\langle 0|Q_i - c_i^p \bar{s}d|K^0\rangle = 0 \tag{5.34}$$

We note that the subtraction of the pseudo-scalar operator $\bar{s}\gamma_5 d$ is necessary because of the large coupling to the vacuum state, especially when we have a right-handed vertex. Without the subtraction of this operator, we must determine the kaon to vacuum matrix element $\langle 0|Q_i|K^0\rangle$ and directly subtract it using $\frac{\langle K^0|Q_i|n\rangle\langle n|Q_i|K^0\rangle}{m_K}$. Due to the large size of the kaon to vacuum matrix element on the lattice, the amplitude of the subtracted term is very large and after the subtraction, the size of our integrated correlator will be reduced by a factor on the order of 100. Therefore we will have a very large statistical error if we choose to subtract the vacuum state directly. On the other hand, the subtraction of the scalar operator $\bar{s}d$ is less important because the kaon to pion matrix element $\langle \pi|Q_i|K^0\rangle$ is not that large. Using the scalar operator subtraction still reduces the error by roughly a factor of 5. We have listed the contribution to $\mathrm{Im}\, M_{00}^{ut}$ including all five types of diagrams in Table 5.9, and the fitting of the final integrated correlator is plotted in Fig 5.10 and Fig 5.11. We have corrected the short distance divergence for the lattice operator using an intermediate RI

scheme with scale $\mu_{RI} = 2.11$ GeV. The sum of all the contributions from different operator combinations Q_iQ_j will be the total lattice result for the Im $M_{\bar{0}0}^{ut}$, which includes all the low energy contributions up to a high energy cutoff determined by μ_{RI}. We call this Im $M_{\bar{0}0}^{ut,RI}$, and this corresponds to the contribution to Im $M_{\bar{0}0}^{ut}$, from the RI operator defined in Eq.5.10, or from the first line in the total $\Delta S = 2$ weak Hamiltonian (Eq. 5.12). We list the results for different types of diagrams in Table 5.10. In the fitting of Fig 5.10 and Fig 5.11, we have used a correlated fit with fitting range 10:16, and we show the χ^2 per degree of freedom in the figure. In fitting the connected diagrams in Fig. 5.8 and Fig. 5.9, we used a fitting range of 12:16. This is because a linear fit cannot represent the data well for smaller T, and using a longer fitting range gives a poor χ^2 (with χ^2/d.o.f on the size of 5 or more). While this choice of fitting range give a relatively large statistical error (compared to 10:16), it gives more reliable results because of the better χ^2.

By comparing Table 5.8 and Table 5.9, we can see that the inclusion of the disconnected diagrams does not change the result for Im $M_{\bar{0}0}^{ut}$ significantly for most of the operator combinations Q_iQ_j. This is different from our experience in the ΔM_K calculation that inclusion of the disconnected diagram will cancel part of the connected diagram result, decreasing the final result by roughly a factor of 2. Because the type 1 and type 2 diagrams are measured very accurately, so in our final results for ϵ_K we also quote the numbers from only the type 1 and type 2 diagrams.

Q_1Q_1	Q_1Q_2	Q_1Q_3	Q_1Q_4	Q_1Q_5	Q_1Q_6
	Q_2Q_2	Q_2Q_3	Q_2Q_4	Q_2Q_5	Q_2Q_6
-0.384(0.016)	0.438(0.069)	0.067(0.006)	0.004(0.012)	-0.016(0.013)	0.091(0.113)
	-1.565(0.121)	-0.013(0.011)	0.200(0.027)	-0.001(0.038)	0.193(0.328)

Table 5.9: Imaginary part of $M_{\bar{0}0}^{ut}$, after the subtraction of the short distance divergent part, and with all the Wilson coefficients multiplied. We have included all 5 types of diagrams. All numbers are in units of 10^{-15} MeV.

To get the final long distance correction to ϵ_K, we have to add the $RI \to \overline{MS}$ contribution determined from perturbation theory, which corresponds to the second line of Eq 5.12. We

$\mathrm{Im}\, M_{\bar{0}0}^{ut,lat,type\,1+2}$	$\mathrm{Im}\, M_{\bar{0}0}^{ut,RI,type\,1+2}$	$\mathrm{Im}\, M_{\bar{0}0}^{ut,RI}$	$\mathrm{Im}\, M_{\bar{0}0}^{ut,ld\,corr}$
-1.328(0.038)	-0.865(0.037)	-0.986(0.389)	-0.552(0.389)

Table 5.10: Contributions to $\mathrm{Im}\, M_{\bar{0}0}^{ut}$, in units of 10^{-15} MeV. The first column is before we remove the short distance divergence from our lattice result, and only includes the type 1 & 2 diagrams. The second column is after the removal of the short distance divergence. The third column is after removal of the divergence and includes all five types of diagrams. The last column is our final long distance correction to $\mathrm{Im}\, M_{\bar{0}0}^{ut}$, with the perturbative $RI \to \overline{MS}$ part included. We have chosen $\mu_{RI} = 2.11$ GeV.

have evaluated $\Delta Y^{i,j}$, which is independent of the $\overline{MS}$ scale μ, and it is multiplied by the kaon bag parameter B_K defined as follows:

$$\langle K^{\bar{0}}|Q(\mu)|K^0\rangle = \frac{4}{3}F_K^2 m_K B_K(\mu). \tag{5.35}$$

We note that this is different from the conventional formula by a factor of $2m_K$ because we used a different renormalization for our kaon wave function. To perform a consistent matching to our lattice calculation, we choose to use the parameters B_K, F_K, and m_K that were determined on the same gauge ensemble that we have used for this lattice calculation, rather than the more accurate values from more recent measurements or experiments. The scale dependence of B_K will be of order α_s, so using a single B_K value for different μ_{RI} is consistent with our NLO calculation. We take the value for B_K and F_K from [25], which gives

$$B_K^{RGI} = 0.750(15), \quad F_K = 155.5(8)\,\mathrm{MeV}. \tag{5.36}$$

The RGI value for B_K is the renormalization-group-independent value, which is defined in Eq. (18.4) of [10]. We can use this formula to find B_K at any energy scale. In the last column of Table 5.10, we have used the value of B_K at 2.11 GeV to find the $RI \to \overline{MS}$ correction. The number in the last column is the sum of this term proportional to B_K and the RI term we obtained from the lattice calculation. In Table 5.11, we show the result of this calculation for five different intermediate RI scales μ_{RI}, and in Table 5.12 we show

the result of the same calculation but include only type 1 and type 2 diagrams. We can see our RI matching is successful because the final long distance correction to ϵ_K has a very small dependence on μ_{RI}. In all of these results, we have chosen to use B_K at 2.11 GeV because the scale dependence of B_K is of higher order. We've also tried to use a different value for B_K defined at the varying scale μ_{RI} and find less than 5% difference in the results. In Fig. 5.12, we plot the μ_{RI} dependence of the RI part and the $RI \to \overline{MS}$ part of $\mathrm{Im}\, M_{\bar{0}0}^{ut}$, calculated from the lattice and from perturbation theory respectively. We also plot the sum of these two terms, which is our final long distance correction to $\mathrm{Im}\, M_{\bar{0}0}^{ut}$. We also show a second, similar plot in Fig. 5.12 which includes only type 1 and type 2 diagrams.

μ_{RI}	$\mathrm{Im}\, M_{\bar{0}0}^{ut,RI}$	$\mathrm{Im}\, M_{\bar{0}0}^{ut,RI\to\overline{MS}}$	$\mathrm{Im}\, M_{\bar{0}0}^{ut,ld\,corr}$	$\epsilon_K^{ut,ld\,corr}$
1.54 GeV	-0.746(0.389)	0.282	-0.464 (0.389)	0.0911(0.076)
1.92 GeV	-0.912(0.389)	0.384	-0.527 (0.389)	0.104(0.076)
2.11 GeV	-0.986(0.389)	0.434	-0.551 (0.389)	0.108(0.076)
2.31 GeV	-1.050(0.390)	0.486	-0.565 (0.390)	0.111(0.077)
2.56 GeV	-1.115(0.390)	0.548	-0.568 (0.390)	0.111(0.077)

Table 5.11: The contributions to $\mathrm{Im}\, M_{\bar{0}0}^{ut}$ (in units of 10^{-15} MeV), and the corresponding contribution to ϵ_K as we vary μ_{RI}. The second column presents our results from the lattice calculation, after the removal of the short distance divergence. The third column is the perturbative part that involves ΔY. The fourth column is our final long distance correction to $\mathrm{Im}\, M_{\bar{0}0}^{ut}$, which is the sum of the previous two columns. The last column is the corresponding contribution to ϵ_K, in units of 10^{-3}. We have chosen to use B_K at $\mu = 2.11$ GeV.

μ_{RI}	$\mathrm{Im}\, M_{\bar{0}0}^{ut,RI}$	$\mathrm{Im}\, M_{\bar{0}0}^{ut,RI\to\overline{MS}}$	$\mathrm{Im}\, M_{\bar{0}0}^{ut,ld\,corr}$	$\epsilon_K^{ut,ld\,corr}$
1.54 GeV	-0.620(0.036)	0.282	-0.337(0.036)	0.066(0.007)
1.92 GeV	-0.786(0.036)	0.384	-0.401(0.036)	0.079(0.007)
2.11 GeV	-0.860(0.037)	0.434	-0.425(0.037)	0.084(0.007)
2.31 GeV	-0.924(0.037)	0.486	-0.439(0.037)	0.086(0.007)
2.56 GeV	-0.989(0.037)	0.548	-0.442(0.037)	0.087(0.007)

Table 5.12: Results similar to those in Table 5.11, but with only type 1 and 2 diagrams.

From Fig. 5.12, we can see that our final long distance correction to $\mathrm{Im}\, M_{\bar{0}0}^{ut}$ depends very little on the intermediate scheme μ_{RI}. The dependence is smaller when the energy scale

is high, which can be understood because the systematic error from perturbation theory is expected to be less at a higher scale. However, a μ_{RI} that is too high may introduce additional discretization errors, so we choose to quote our results using $\mu_{RI} = 2.11$ GeV.

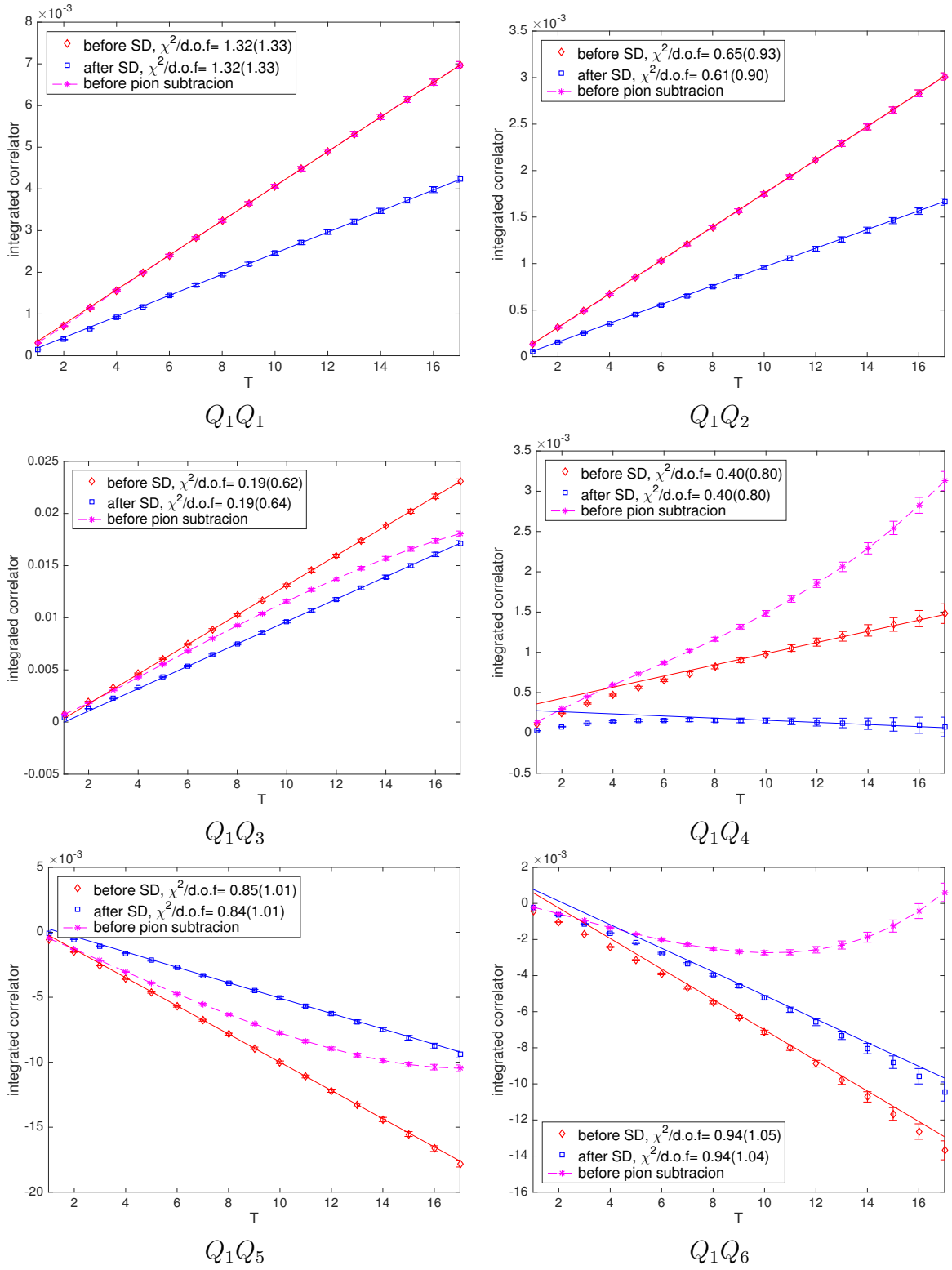

Figure 5.8: Integrated correlator including only type 1 and type 2 diagrams. We shown the result before and after we subtract the single pion state, and also after we subtracted the short distance part. The Wilson coefficients are not included.

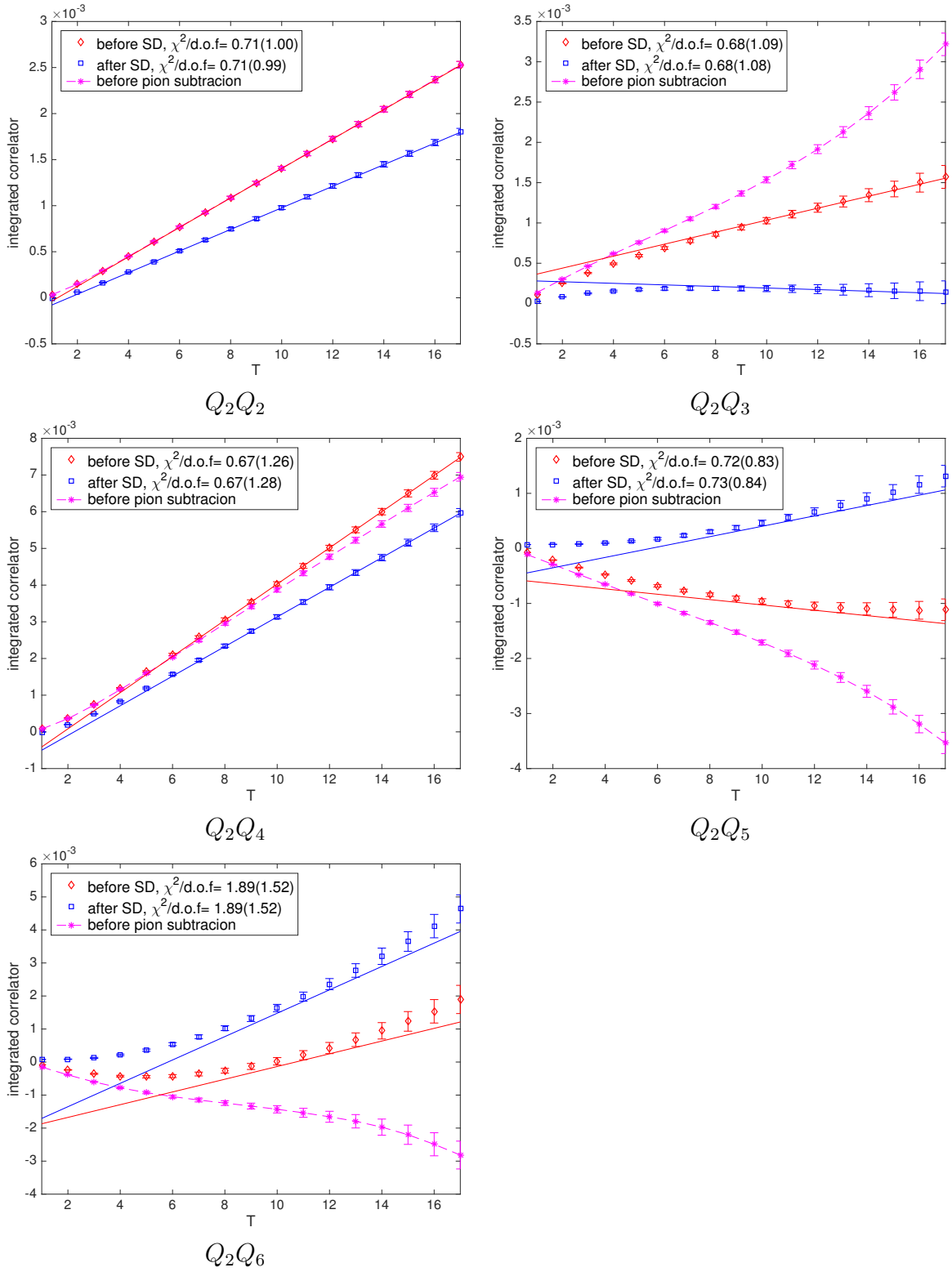

Figure 5.9: Integrated correlator including only type 1 and type 2 diagrams. We shown the result before and after we subtract the single pion state, and also after we subtracted the short distance part. The Wilson coefficients are not included.

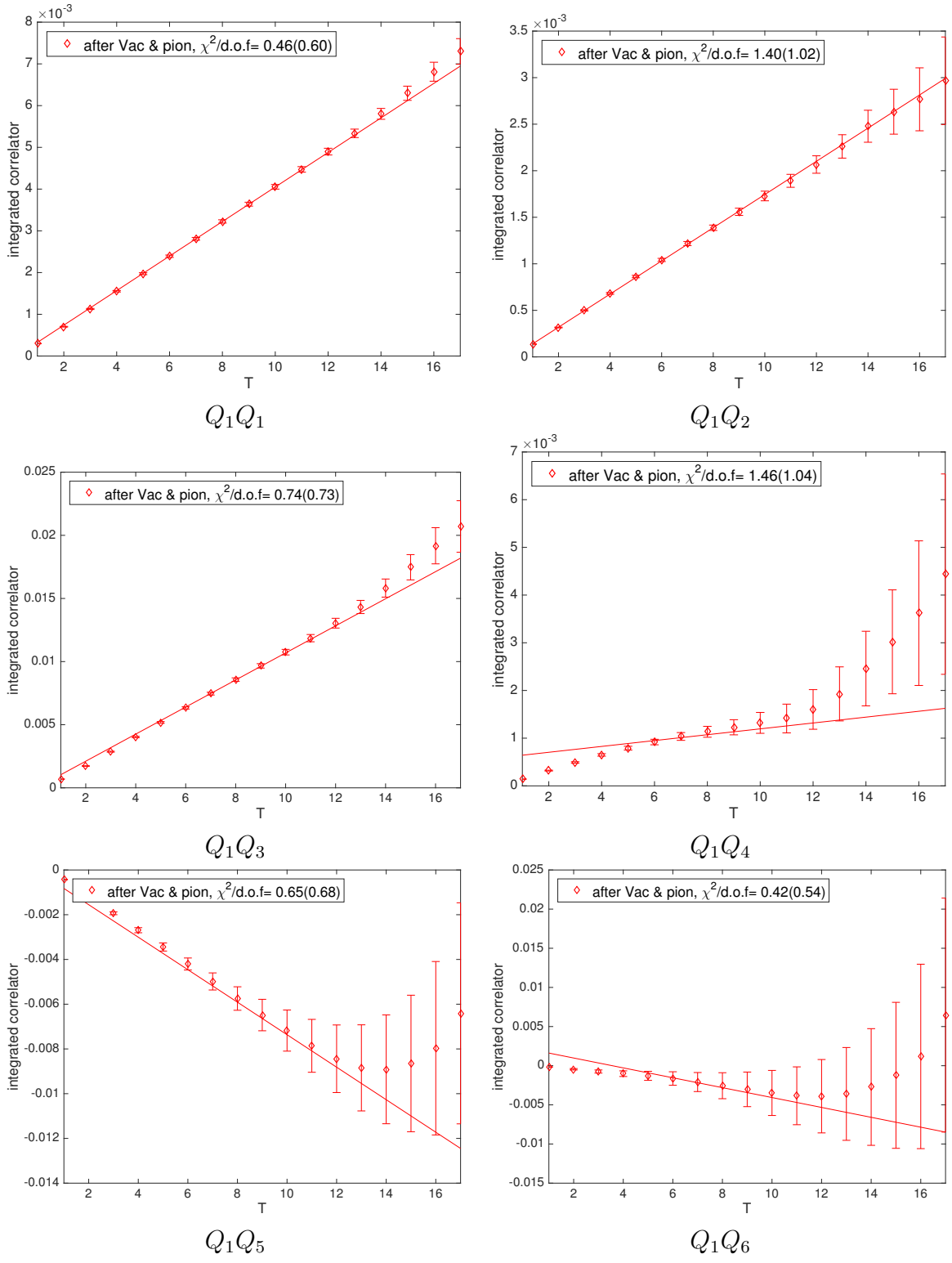

Figure 5.10: Integrated correlator including all five types of diagrams. We use a correlated fit with fitting range $T = 10 : 16$. The Wilson coefficients are not included.

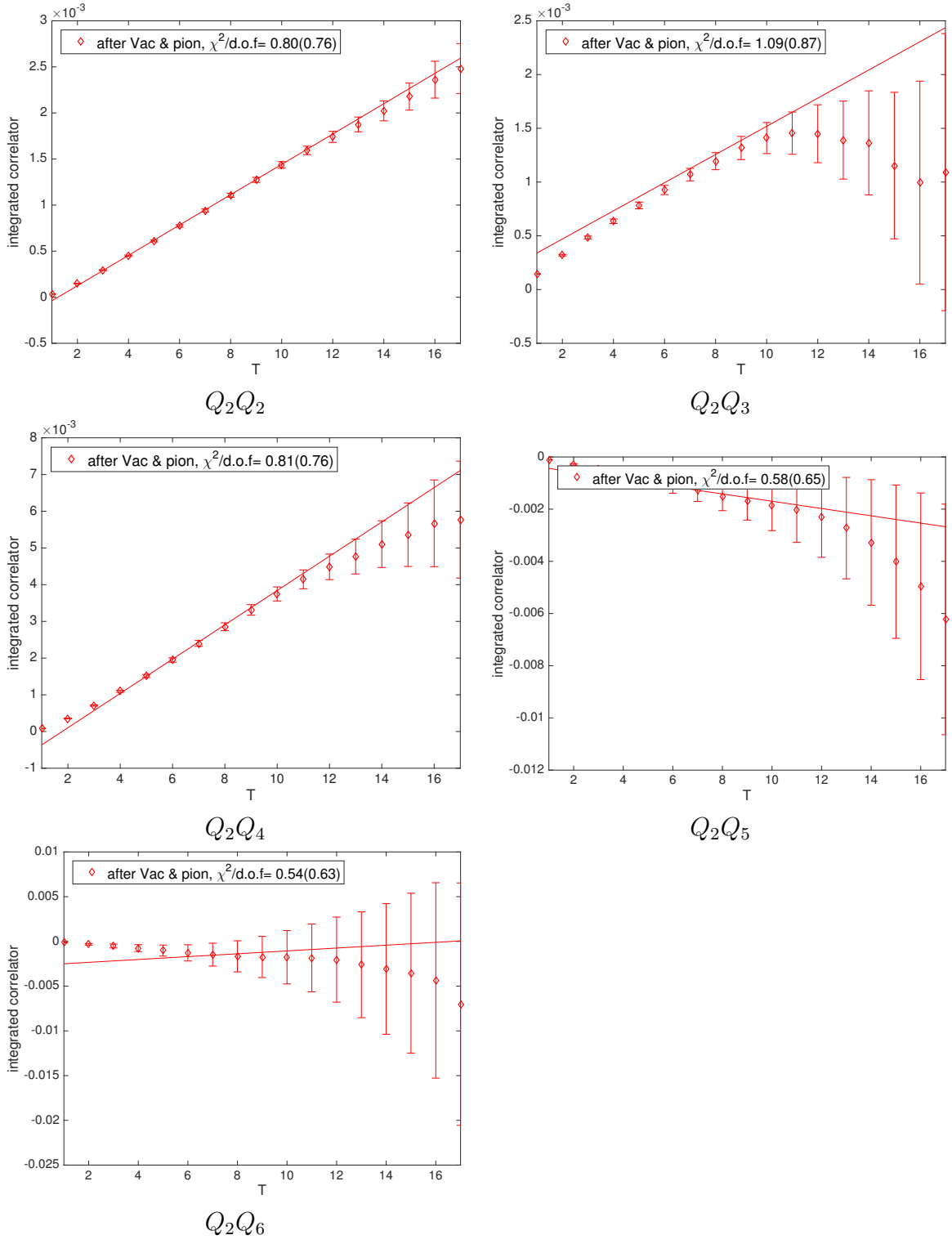

Figure 5.11: Integrated correlator including all five types of diagrams. We use a correlated fit with fitting range $T = 10 : 16$. The Wilson coefficients are not included.

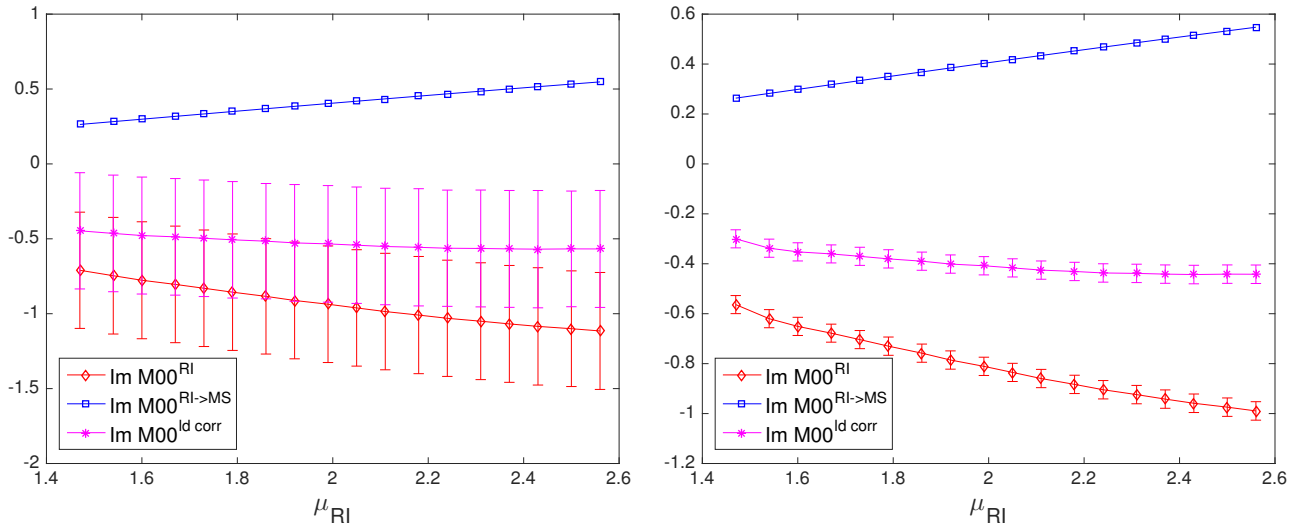

Figure 5.12: Im $M_{\bar{0}0}^{ut,RI}$, Im $M_{\bar{0}0}^{ut,RI\to\overline{MS}}$ and Im $M_{\bar{0}0}^{ut,ld\,corr}$ for different μ_{RI}, in units of 10^{-15} MeV. On the left, all types of diagrams are included. On the right, only type 1 and type 2 diagrams are included.

5.4 Conclusion and outlook

We have performed a lattice calculation to determine the $\mathrm{Im}\, M_{\bar{0}0}^{ut,RI}$ and a perturbation theory calculation to find $\mathrm{Im}\, M_{\bar{0}0}^{ut,RI\to\overline{MS}}$. These two terms correspond to the first two lines of Eq. 5.12. We call their sum the "long distance correction" to $\mathrm{Im}\, M_{\bar{0}0}^{ut}$. This should be added to the usual short distance evaluation of $\mathrm{Im}\, M_{\bar{0}0}^{ut}$, which corresponds to the third line of Eq. 5.12. Then we can use Eq. 2.27 to find the result for ϵ_K. However, in our calculation, we have used an $\overline{MS}$ scale of 2.15 GeV, in order to reduce the systematic errors from perturbation theory for both the Wilson coefficients and the correction given by $\mathrm{Im}\, M_{\bar{0}0}^{ut,RI\to\overline{MS}}$, while the previous short distance calculations have chose $\mu = m_c$. Therefore, we perform the short distance calculation in NLO now using the larger value $\mu = 2.15$ GeV. The expression for the short distance contribution to $\mathrm{Im}\, M_{\bar{0}0}$, including both the $\lambda_u\lambda_t$ part and the $\lambda_t\lambda_t$ part, is given by:

$$\mathrm{Im}\, M_{\bar{0}0} = \frac{G_F^2}{6\pi^2} F_K^2 m_K M_W^2 B_K\, \mathrm{Im}\{\lambda_t^2 \eta_2' S_0(x_t, x_t, x_c) + 2\lambda_t\lambda_u \eta_3' S_0'(x_t, 0, x_c)\} \tag{5.37}$$

The λ_t^2 term can be evaluated independent of our $\lambda_u\lambda_t$ term, so we will use the value from Table 2.1 and directly apply Eq. 2.39 and Eq. 2.40. To calculate the $\eta_3' S_0(x_t, 0, x_c)$, we might use the relation in Eq. 2.37 and Eq. 2.38 and find it using parameters in Table 2.1. However, we do not choose this approach since it has two minor problems: The first, as we explained above, that we need to evaluate this term at 2.15 GeV instead of the charm mass scale. The second is that the NLO calculation of the η_3 in Table 2.1 is accurate to order $\mathcal{O}(\alpha_s \log M_W/\mu)$, while the NLO calculation of the η_1 term is accurate to order $\mathcal{O}(\alpha_s)$. Also, these terms are not necessarily evaluated at the same scale μ_W, which is another source of inconsistency.

We calculate $\eta_3' S_0'(x_c, x_t)$ from Eq. 5.38 using $\mu_c = 2.15$ GeV and $\mu_W = 130$ GeV:

$$\eta_3' S_0'(x_c, x_t) = x_c(\mu_c)\alpha_s(\mu_c)^{d_4} \times \left[C_7(\mu_c) \left(1 - \frac{\alpha_s(\mu_c)}{4\pi} J_4 \right) + \frac{1}{2} \sum_{i=1}^{2} \sum_{j=1}^{6} C_i(\mu_c) C_j(\mu_c) r_{ij}(\mu_c) \right]. \tag{5.38}$$

This equation differs from those in [10] in two ways: We have absorbed the factor $\frac{\pi}{\alpha_s(\mu_c)}$ into the Wilson Coefficient C_7, and we evaluate this quantity above the charm quark mass threshold in a four flavor theory. Because of the renormalization group running and the running quark mass, both factors η_3' and $S_0'(x_c, x_t)$ have μ_c and μ_W dependence, so we do not quote their independent values. We have plotted the μ dependence of $\eta_3' S_0'(x_c, x_t)$ in Fig. 5.13, and we can see the dependence on μ becomes much weaker at an energy scale above 2 GeV compared to the common choice of m_c.. This indicates the benefit of evaluating this term at a higher energy scale. We have listed the different component of ϵ_K in Table 5.13 and all of our input parameters for the short distance calculation are listed in Table 5.14. We used the exclusive value for V_{cb} from [7]. It has been shown that there is a 3σ discrepancy between the experimental and Standard Model values. Our long distance calculation, which gives a result that is about 5% of the total ϵ_K value, makes this discrepancy smaller,

$$\epsilon_K^{ld\,corr} = 0.108(0.076) \times 10^{-3}.$$

However, we should note that our lattice calculation is unphysical with unphysically large pion and light charm quark masses. This calculation serves mainly to demonstrate the method and the possibility of performing this calculation instead of providing a physical result that can be compared with experiment. A more physical calculation using a gauge ensemble with a smaller lattice spacing and a larger physical volume will provide us more realistic information.

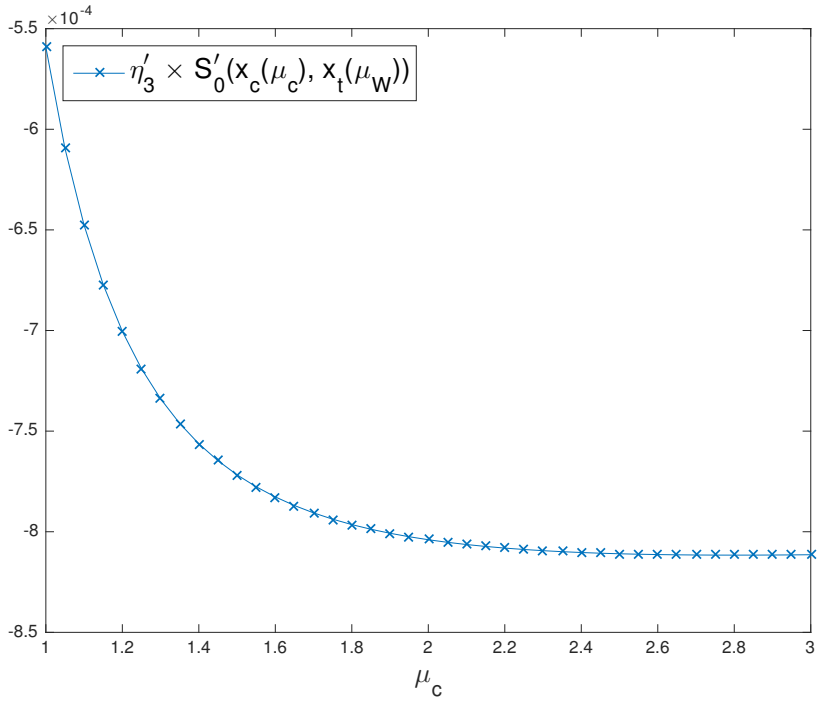

Figure 5.13: Scale dependence of $\eta_3' S_0'(x_c, x_t)$, calculated using the four-flavor theory.

$\eta_2' S_0'(x_t, x_t, x_c)$	$\eta_3' S_0'(x_t, 0, x_c)$	ϵ_K^{tt}
1.4208	-8.07×10^{-4}	1.293×10^{-3}
ϵ_K^{ut}	$\epsilon_K^{ld\,corr}$	ϵ_K^{ξ}
0.545×10^{-3}	$0.108(0.076) \times 10^{-3}$	$-0.039(0.034) \times 10^{-3}$

Table 5.13: The different short distance contribution to ϵ_K. I have used a perturbative calculation in NLO and using the CKM parameters from the angle-only-fit (AOF)[2], exclusive V_{cb} [3]. The last two columns are our long distance correction to ϵ_K and the contribution from ξ quoted from the $K \to \pi\pi$ measurement in [4]. I have dropped the statistical error from the short distance calculation.

G_F	1.16637×10^{-5}
B_K	0.7661
F_K	0.1562 GeV
m_K	0.4976 GeV
M_W	80.385 GeV
$m_c(m_c)$	1.29 GeV
$m_t(m_t)$	170 GeV
ΔM_K	3.484×10^{-15} GeV
λ_u	0.2196
λ_c	-0.2193 - $1.1572 \times 10^{-4}i$
λ_t	$-2.9565 \times 10^{-4} + 1.1572 \times 10^{-4}i$

Table 5.14: Input parameters used in short distance calculation.

Chapter 6

ΔM_K from the $32^3 \times 64$ lattice

The detailed procedure for the ΔM_K calculation can be found in [21] and [26]. So we only give a brief introduction about the structure of the weak Hamiltonian H_W. For ΔM_K, since it involves only the real part of the $K^0 - \bar{K}^0$ mixing matrix element (Eq. 2.17), we need only to consider the contribution from the first term of Eq. 2.35. This is because the other terms are suppressed by a factor of $\lambda_t/\lambda_u \sim 10^{-3}$. For the same reason, we can drop all the QCD penguin diagrams. Therefore the $\Delta S = 1$ weak Hamiltonian is given by:

$$H^{\Delta S=1} = \frac{G_F}{\sqrt{2}} \sum_{q,q'=u,c} V^*_{q',s} V_{q,d} \sum_{i=1,2} C_i Q_i^{q',q}. \tag{6.1}$$

In the above formula, we have only the current-current operators $Q_{1,2}$. Using the same reason, we drop the λ_t term to write $V^*_{u,s}V_{u,d} = -V^*_{c,s}V_{c,d}$. Therefore, when we evaluate the product of two $H_W^{\Delta S=1}$ operators, we will get an operator structure of $\bar{u}u\bar{u}u + \bar{c}c\bar{c}c - \bar{u}c\bar{c}u - \bar{c}u\bar{u}c$. Therefore, all the four point functions we calculated in Fig. 6.1, which involve the product of two $H_W^{\Delta S=1}$ operators, will have the internal quark lines with a structure $(u - c)$. The internal quark line refers to the quark propagator connecting the two vertices in the type 1&2 diagrams and the self-loop in the type 3&4 diagrams.

6.1 Details of simulation

We work on a 2+1 flavor, $32^3 \times 64 \times 32$ DWF lattice, with the Iwasaki + DSDR gauge action, and an inverse lattice spacing $1/a = 1.38$ GeV. The pion mass is 171 MeV and the kaon mass is 492 MeV. We implement GIM cancellation by including a quenched charm quark. We use two choices of charm quark mass, 0.38 and 0.3 in lattice units, which correspond to 750 MeV and 592 MeV in $\overline{MS}$ scheme defined at 2 GeV. We have used 120 configurations for the charm quark mass of 750 MeV and only 100 for the charm quark mass of 592 MeV. We have previously made ~ 400 measurements but the random number generator they used was incorrect. It had small correlations between the random numbers used on different lattice sites. However, we used data from these earlier measurements for the $\pi\pi$ scattering and the two point functions that determine the η mass. This is because these data do not contain random numbers and the η states and $\pi\pi$ states with isospin 0 have large statistical error, so we can benefit from using more measurements. In the analysis for $m_c = 750$ MeV, I used 360 configurations for the two pion energy and η mass, and for $m_c = 592$ MeV, I used 300 configurations. The way I combined the data is simply bin three configurations into one.

In order to accelerate the inversion, we used low-mode deflation with 560 eigenvectors obtained using the Lanczos algorithm. Also, we used Möbius fermions, which can allow us to use a smaller fifth dimension length L_s than the value $L_s = 32$ that we used in generating the gauge configurations using Shamir domain wall fermions. We evaluated the residual mass m_{res} for different choices of fifth dimension length L_s and the corresponding Möbius parameter $b + c$, while fixing $L_s \times (b + c) = 32$. We can see from table 6.1 that by using $L_s = 12$, and $b + c = 2.667$, we can keep our m_{res} at its unitary value $1.8447(60) \times 10^{-3}$, and obtain the best accelerating effect.

As in [1], we calculate all four types of four point diagrams, shown in Fig.6.1. In order to subtract the two-pion intermediate state, we must also calculate the kaon to two-pion matrix element $\langle \pi\pi | H_W | K \rangle$. The four types of diagrams that contribute to this process are shown in

L_s	16	14	12	10
$b+c$	2	2.286	2.667	3.2
m_{res}	$1.769(16) \times 10^{-3}$	$1.783(12) \times 10^{-3}$	$1.830(15) \times 10^{-3}$	$2.877(13) \times 10^{-3}$

Table 6.1: The residual mass m_{res} for different choice of L_s with Möbius fermions.

Fig 6.2. We use Coulomb gauge fixed wall sources for the kaon and the two-pion operators, and a point-source propagator at each time slice for the internal quark lines coming from one of the weak vertices in type 1&2 four point diagrams. For the self-loop in the type 3&4 four point diagrams and the three point diagrams, we use a random space-time volume source with 60 hits for the high-mode part, and we construct the low-mode part of the propagator from the 560 eigenvectors we obtained from the Lanczos Algorithm. Compared to the random wall source propagators we used in [1], our new method has two benefits. The first is that we do not have to do a propagator inversion for each time slice. Using a random volume source with 60 hits obtain an error similar in size compared that from using 5 random hits for each time slice in the random wall source propagators. The second is that by using the eigenvectors to construct the low-mode part of the propagator, the low-mode part becomes precise instead of random. This further reduces the error by at least a factor of 2.

In the treatment of the two-pion state, we separate the two pions in the source or sink by 4 units in the time direction to reduce the vacuum noise.

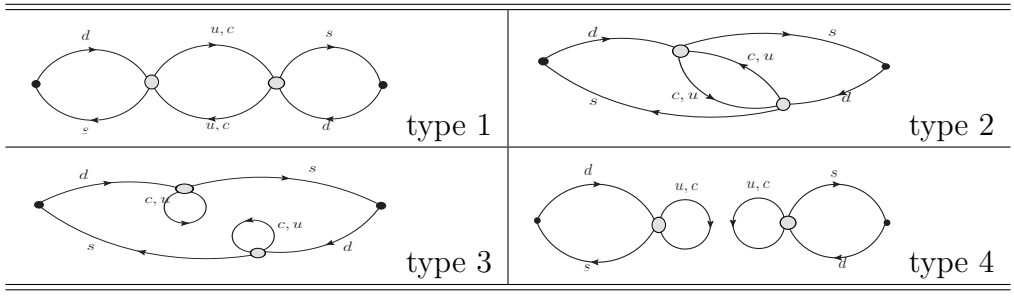

Figure 6.1: Four types of four-point diagrams used in the calculation of the integrated correlator.

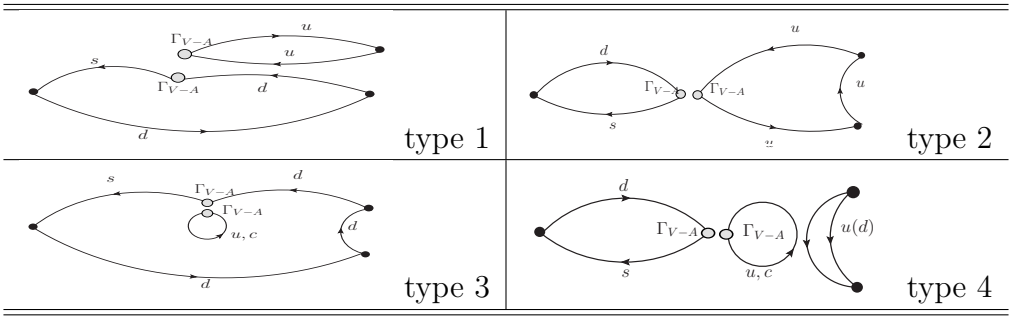

Figure 6.2: The Four types of diagrams which enter the calculation of $\langle \pi\pi | H_W | K \rangle$.

6.2 Results for $K_L - K_S$ mass difference

As in [1], we will first identify the intermediate state lighter than the kaon and remove their contribution to the exponential growing term in the integrated correlator. Then we can fit the T dependence of the integrated correlator to obtain ΔM_K. The intermediate states that we should consider are the vacuum state, the single-pion state, the two-pion state, and the η meson state. We discuss the treatment of their contribution in the following sections. We list the energies of different states in Table. 6.2. We show the effective mass plot for the two pion state and the eta state in Fig. 6.3 and Fig. 6.4. The $\pi\pi$ state with $I = 0$ has relatively large errors due to the disconnected diagrams, and the η states has the largest error since it is dominated by disconnected diagrams and has a relatively heavy mass.

6.2.1 Treatment of vacuum and η state

Because the vacuum intermediate state has the largest matrix element $\langle 0 | H_W | K \rangle$, if we directly subtract the vacuum state, then the statistical error in our final integrated correlator is very large, making fitting impossible. Therefore, we must use our freedom of adding a pseudo-scalar operator $\bar{s}\gamma_5 d$ to eliminate the vacuum contribution.

The treatment of η state is more complicated. First, we note that operators corresponding to η and η' are mixtures of the octet operator $O_8 = (\bar{u}\gamma_5 u + \bar{d}\gamma_5 d - 2\bar{s}\gamma_5 s)/\sqrt{6}$ and the singlet operator $O_1 = (\bar{u}\gamma_5 u + \bar{d}\gamma_5 d + \bar{s}\gamma_5 s)/\sqrt{3}$. The mixing angle θ is introduced such that the $|\eta\rangle$

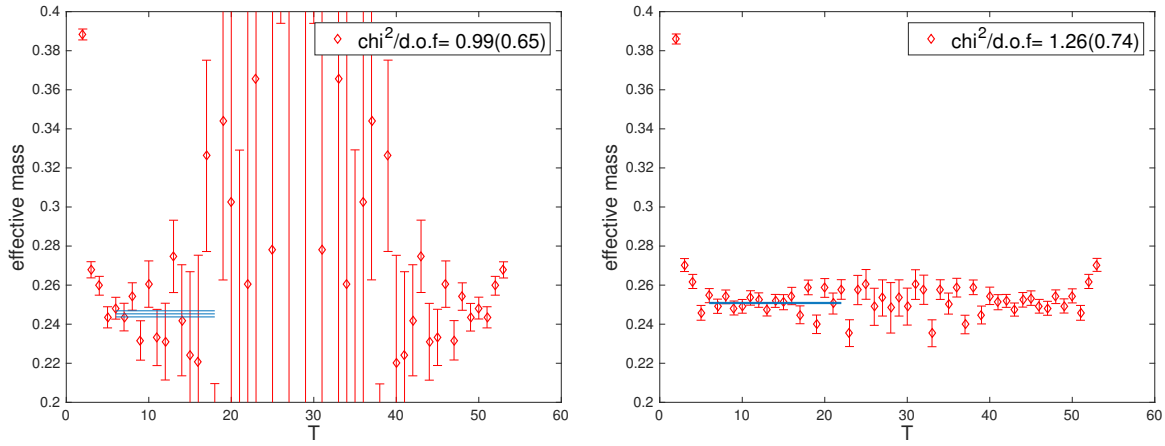

Figure 6.3: The effective mass for the two-pion states with $I = 0$ (on the left) and $I = 2$ (on the right).

and $|\eta'\rangle$ can be approximately written as:

$$\begin{pmatrix} |\eta\rangle \\ |\eta'\rangle \end{pmatrix} = \begin{pmatrix} \cos\theta & -\sin\theta \\ \sin\theta & \cos\theta \end{pmatrix} \begin{pmatrix} O_8|0\rangle \\ O_1|0\rangle \end{pmatrix}, \tag{6.2}$$

We can determine the mixing angle θ using lattice methods,as in [27]. We however don't choose this approach because the $|\eta'\rangle$ state, which is heavier than the $|\eta\rangle$ state , will give rise to huge statistical errors. Also , the mixing angle θ is of the order of $10°$, we can safely neglect it and use O_8 to generate our $|\eta\rangle$ state.

Because of the disconnected diagrams that enter the determination of the kaon to η matrix element, subtracting the η directly will give rise to a very large statistical error. Therefore we treat the η state similar to the vacuum: We use the scalar operator $\bar{s}d$ to eliminate the η intermediate state contribution. This is same as was done in [1]: we add scalar and pseudo-scalar operators to our weak Hamiltonian to get a modified Hamiltonian H'_w:

$$H'_W = H_W + c_p \bar{s}\gamma_5 d + c_s \bar{s} d. \tag{6.3}$$

Adding these two operators to our Hamiltonian does not change the physical result, but

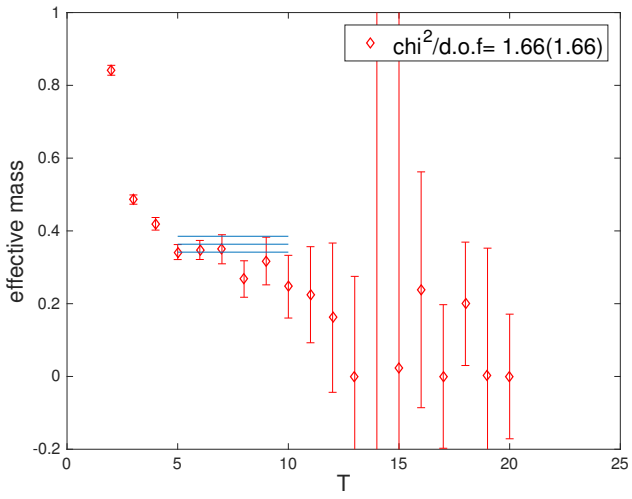

Figure 6.4: The effective mass for the η states.

will change the contribution of the intermediate states, so that the vacuum and η do not contribute. The two coefficients are determined by:

$$\langle 0|H_W + c_p \bar{s}\gamma_5 d|K\rangle = 0\,, \tag{6.4}$$

$$\langle \eta|H_W + c_s \bar{s}d|K\rangle = 0\,. \tag{6.5}$$

The coefficients c_s, c_p are shown in Table 6.3. We plot the fitting of the coefficient c_s in Fig. 6.5. We directly fit the ratio $\frac{\langle\eta|Q_i|K^0\rangle}{\langle\eta|\bar{s}d|K^0\rangle}$, since these two quantities are highly correlated and we can reduce the noise by taking this ratio.

M_K	M_π	M_η	$E_{\pi\pi,I=0}$	$E_{\pi\pi,I=2}$
496.4(4)	172.9(3)	501(30)	336.7(15)	346.0(4)

Table 6.2: Effective masses for the pion, kaon, η, and two-pion states, in units of MeV.

m_c	c_{1s}	c_{2s}	c_{1p}	c_{2p}
750 MeV	$6.8(14)\times10^{-4}$	$-8.7(8)\times10^{-4}$	$-4.205(10)\times10^{-4}$	$7.379(10)\times10^{-4}$
592 MeV	$6.2(18)\times10^{-4}$	$-7.6(11)\times10^{-4}$	$-3.906(10)\times10^{-4}$	$6.450(10)\times10^{-4}$

Table 6.3: The subtraction coefficients c_s, c_p, used for the operators Q_1 and Q_2 separately.

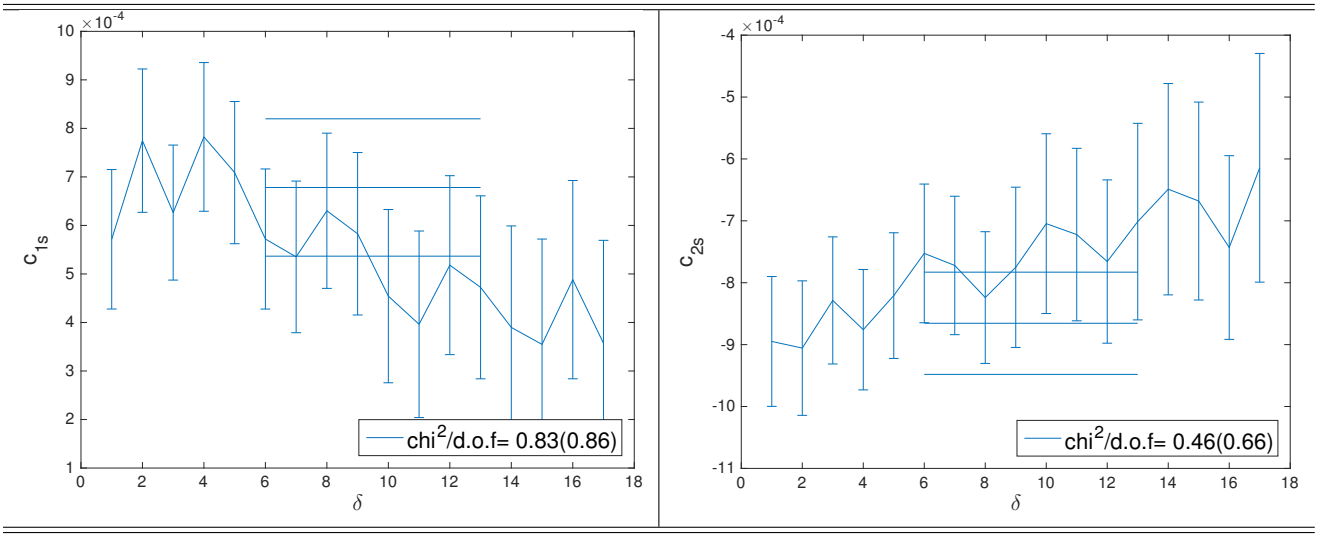

Figure 6.5: The fitting of the ratio $\frac{\langle\eta|Q_i|K^0\rangle}{\langle\eta|\bar{s}d|K^0\rangle}$, for operators Q_1 and Q_2 separately and charm mass 750 MeV. We used the fitting method in Sec. 4.2.2, and the horizontal axis is separation δ between the operator and the η sink.

6.2.2 Two-pion contribution to ΔM_K

With the modified Hamiltonian, we calculate the kaon to two-pion matrix element $\langle\pi\pi|H'_W|K\rangle$, with both isospin 0 and 2. Because we have included the operator $\bar{s}\gamma_5 d$ in H'_W, we also need to calculate the matrix element $\langle\pi\pi|\bar{s}\gamma_5 d|K\rangle$. The corresponding diagrams are shown in figure 6.6. We note the $\bar{s}\gamma_5 d$ operator does not contribute to $\langle\pi\pi_{I=2}|H'_W|K\rangle$, because this matrix element receives contribution only from type 1 and 2 diagrams in Fig 6.2.

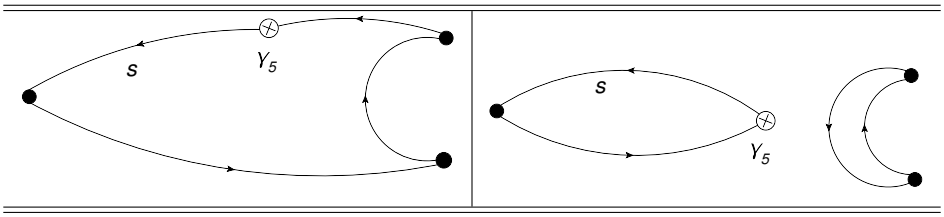

Figure 6.6: The kaon to two-pion subtraction diagrams $\langle\pi\pi|\bar{s}\gamma_5 d|K\rangle$.

We have listed the resulting kaon to two pion matrix element in Table 6.4, and the fitting plateaus are shown in Fig 6.7. We can see a clear enhancement of the isospin $I = 0$ kaon to two-pion matrix element relative to the $I = 2$ results, due to the "$\Delta I = 1/2$" rule. The

operators Q_1 and Q_2 have the same matrix element for isospin $I = 2$ required by SU(2) symmetry. The $I = 0$ matrix element are much noisier due to the disconnected diagrams, which are the type 4 diagram as in Fig 6.2. To determine the kaon to two-pion matrix element, we used the method we introduced in section 4.2.2. We show the fitting results in Fig 6.7, and the kaon to $\pi\pi$ matrix element in Table 6.4. The individual contribution of the two-pion states to ΔM_K are listed in Table 6.7.

m_c	$\langle \pi\pi_{I=2}\|Q_1\|K\rangle$	$\langle \pi\pi_{I=2}\|Q_2\|K\rangle$	$\langle \pi\pi_{I=0}\|Q_1\|K\rangle$	$\langle \pi\pi_{I=0}\|Q_2\|K\rangle$
750 MeV	$1.265(10) \times 10^{-4}$	$1.265(10) \times 10^{-4}$	$-4.8(10) \times 10^{-4}$	$6.4(9) \times 10^{-4}$
592 MeV	$1.270(9) \times 10^{-4}$	$1.270(9) \times 10^{-4}$	$-4.9(9) \times 10^{-4}$	$6.6(9) \times 10^{-4}$

Table 6.4: Kaon to two-pion matrix elements in lattice units.

6.2.3 The single pion contribution

We want to identify the kaon to single pion matrix element $\langle \pi|H'_W|K^0\rangle$, with the scalar operator $\bar{s}d$ included. All relevant matrix element are listed in Table 6.5, and the individual contribution of single pion state to ΔM_K is shown in Table 6.7.

m_c	$\langle \pi\|Q_1\|K\rangle$	$\langle \pi\|Q_2\|K\rangle$	$\langle \pi\|\bar{s}d\|K\rangle$
750 MeV	$3.39(16) \times 10^{-4}$	$2.21(2) \times 10^{-3}$	6.48(2)
592 MeV	$4.97(17) \times 10^{-4}$	$1.77(2) \times 10^{-3}$	6.49(2)

Table 6.5: The kaon to single pion matrix element $\langle \pi|Q_{1,2}|K\rangle$ (not including $\bar{s}d$) and the matrix element for the scalar operator $\langle \pi|\bar{s}d|K\rangle$, in lattice units.

6.2.4 $K_L - K_S$ mass difference

We first subtracte all the exponentially growing contributions from the single- and two-pion intermediate state described in the previous sections. We then fit our integrated correlator as a linear function of T. The fitting is shown in Fig 6.8. We also made the corresponding effective slope plot. We show the individual contributions to ΔM_K from different operator

combinations in Table 6.6. All of these numbers have been multiplied by the Wilson coefficient at the energy scale 3 GeV obtained using the RI/SMOM(γ_μ, γ_μ) intermediate scheme. Those Wilson coefficients can be found in Table C.1. We can vary the starting point of our fitting range T_{min} to show the consistency of this fit. We get a smaller error for smaller T_{min} but we might expect larger excited states contamination, so we choose to use $T_{min} = 8$ when we quote our final results.

m_c	T_{min}	Q_1Q_1	Q_1Q_2	Q_2Q_2	ΔM_K
750 MeV	6	0.73(4)	0.83(13)	2.29(17)	3.85(29)
750 MeV	7	0.74(6)	0.90(16)	2.46(20)	4.10(37)
750 MeV	8	0.70(7)	0.79(21)	2.36(26)	3.85(46)
592 MeV	6	0.59(5)	0.80(15)	1.79(17)	3.18(32)
592 MeV	7	0.62(7)	0.96(20)	2.04(22)	3.62(44)
592 MeV	8	0.58(8)	0.89(25)	2.06(29)	3.53(54)

Table 6.6: ΔM_K and the individual contributions from different operator combinations, in the units of 10^{-12} MeV. We have varied the starting point of our fitting range between 6 and 8 time units. All numbers are multiplied by the appropriate Wilson coefficient computed in the (γ_μ, γ_μ) scheme.

We list the individual contributions to ΔM_K from different intermediate state in Table 6.7. We can see the two-pion contribution two ΔM_K is at the few percent level. The $I = 2$ contribution is negligible, due to the "$\Delta I = 1/2$ rule".

m_c	$\Delta M_K(\pi\pi_{I=0})$	$\Delta M_K(\pi\pi_{I=2})$	$\Delta M_K(\pi)$
750 MeV	-0.06(2)	$-6.25(11) \times 10^{-4}$	0.39(15)
592 MeV	-0.06(2)	$-6.25(11) \times 10^{-4}$	0.38(19)

Table 6.7: Individual physical contribution to ΔM_K from the single-pion state and the two-pion state, in units of 10^{-12} MeV. The subtraction of $\bar{s}d$ and $\bar{s}\gamma_5 d$ is included.

We also calculate the individual contribution to ΔM_K from different types of diagrams identified in Fig 6.1. We plot the integrated correlator in Fig 6.9 for the connected type 1&2 diagrams, and in Fig 6.10 the integrated correlator for the type 3&4 diagrams. We note that when subtracting the exponentially growing intermediate states contribution, we have

associated their contributions to specific types of diagrams. This procedure is discussed in detail in [26]. The fitting results are shown in Table 6.8. We notice the cancellation between the connected and disconnected diagrams, which is consistent with our previous result in [1]. However, the contribution of the disconnected type 3&4 diagrams is smaller than what we observed in [1]. In that paper, we concluded that the type 3&4 diagrams gave a large cancellation of the results from the type 1&2 diagrams. However, in this new calculation with a near physical pion mass, we can see that the type 3&4 diagrams are less important. This is now more consistent with the expectation of "OZI" supression [28].

type	m_c	Q_1Q_1	Q_1Q_2	Q_2Q_2	ΔM_K
1/2	750 MeV	0.941(16)	1.223(60)	2.331(92)	4.49(16)
1/2	592 MeV	0.833(17)	1.325(67)	1.963(97)	4.12(17)
3/4	750 MeV	-0.23(6)	-0.42(20)	0.02(26)	-0.63(44)
3/4	592 MeV	-0.24(8)	-0.40(23)	0.12(26)	-0.52(50)

Table 6.8: Fitting results if we only include type 1/2 diagrams or type 3/4 diagrams for different m_c. $T_{min} = 8$ is used.

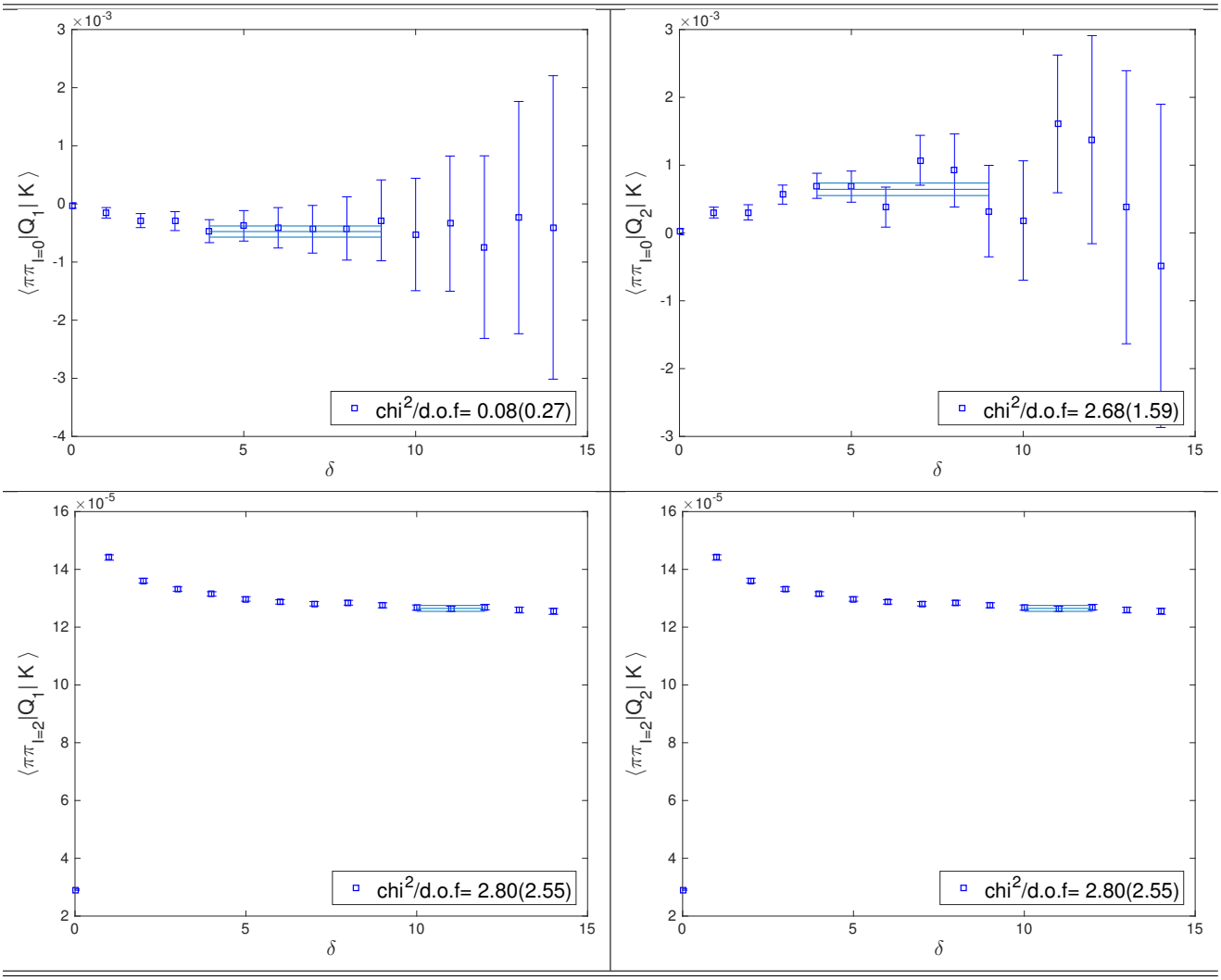

Figure 6.7: Fitting plateaus for the kaon to two-pion matrix element, for the operators Q_1 and Q_2 separately and charm mass 750 MeV. The two-pion state can have isospin either 0 or 2. The x-axis is the separation between the weak operator $Q_{1,2}$ and the sink. We have included the χ^2 per degree of freedom of the fitting, and its statistical error. The horizontal dashed lines show the fitting range, the central value and errors obtained from the fit.

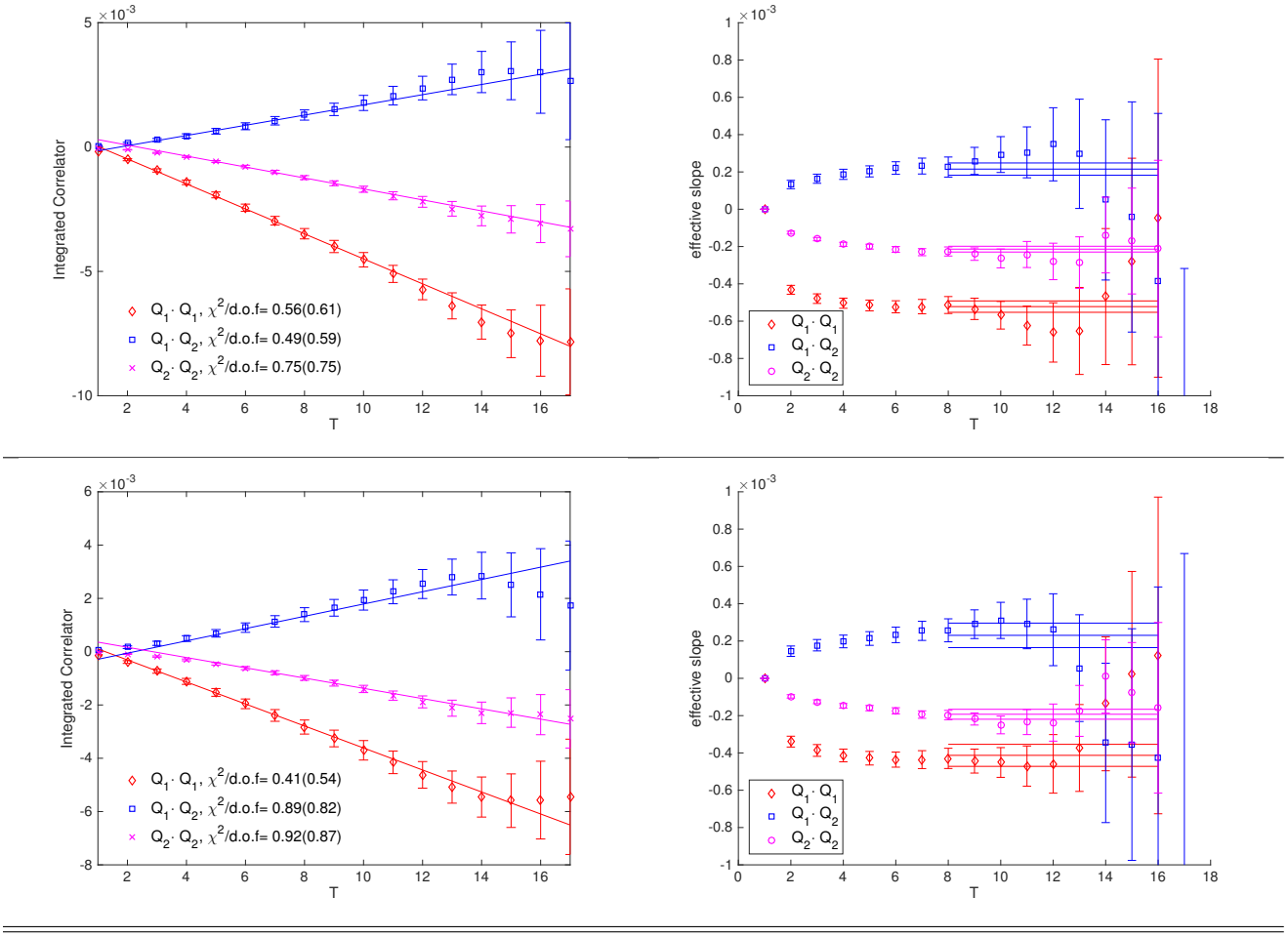

Figure 6.8: Plots of the integrated correlator and the effective slope plot for the three operator products Q_1Q_11, Q_1Q_2 and Q_2Q_2 The upper panel is from $m_c = 0.38$ (750 Mev), and the lower lanel is from $m_c = 0.3$ (592 MeV). $T_{min} = 8$ is used to obtain the fits shown.

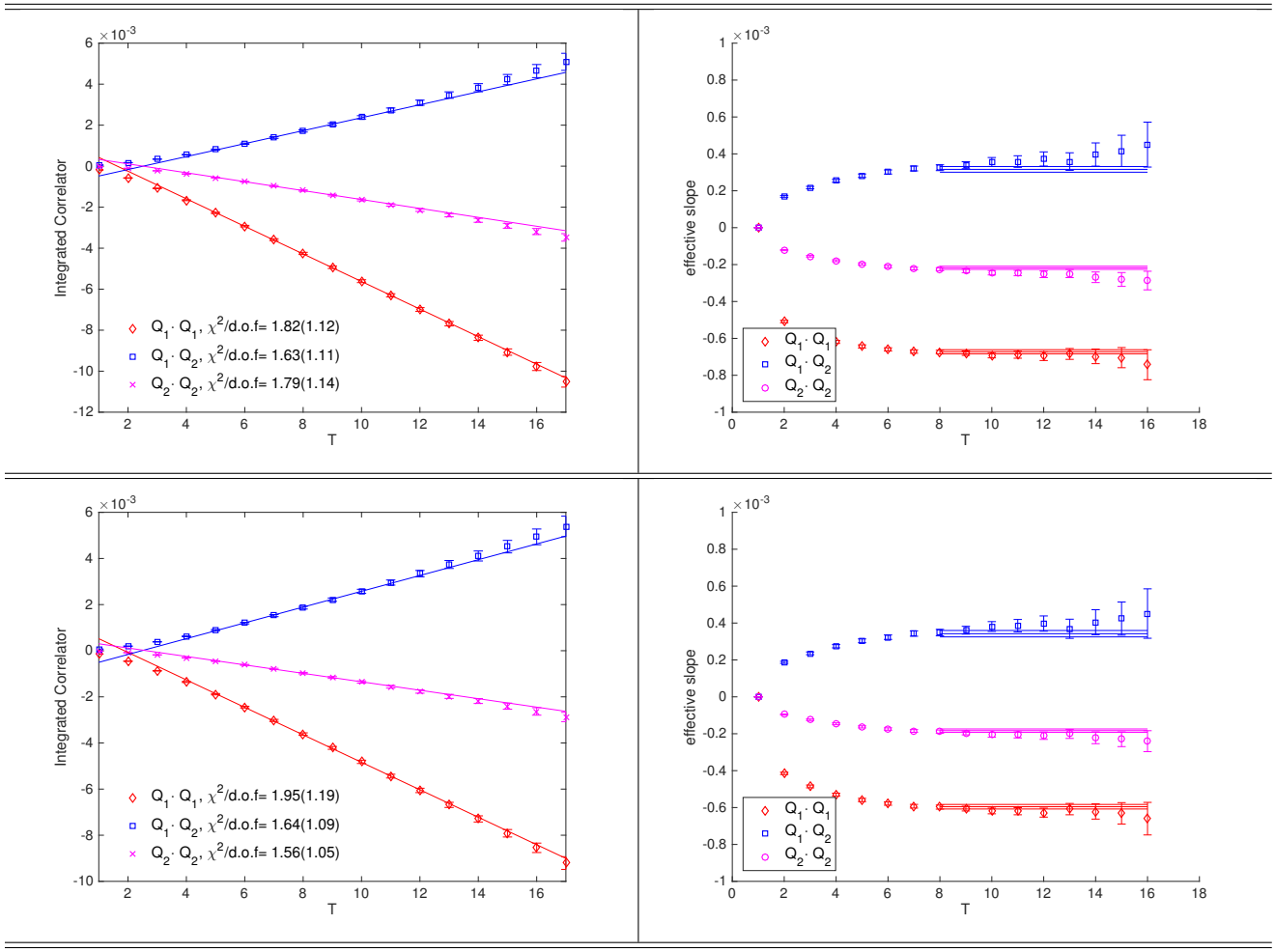

Figure 6.9: Plots for the integrated correlator and the effective slope, for type 1/2 diagrams only. In the upper panel: $m_c = 750$ MeV, while in the lower panel: $m_c = 592$ MeV. $T_{min} = 8$ is used.

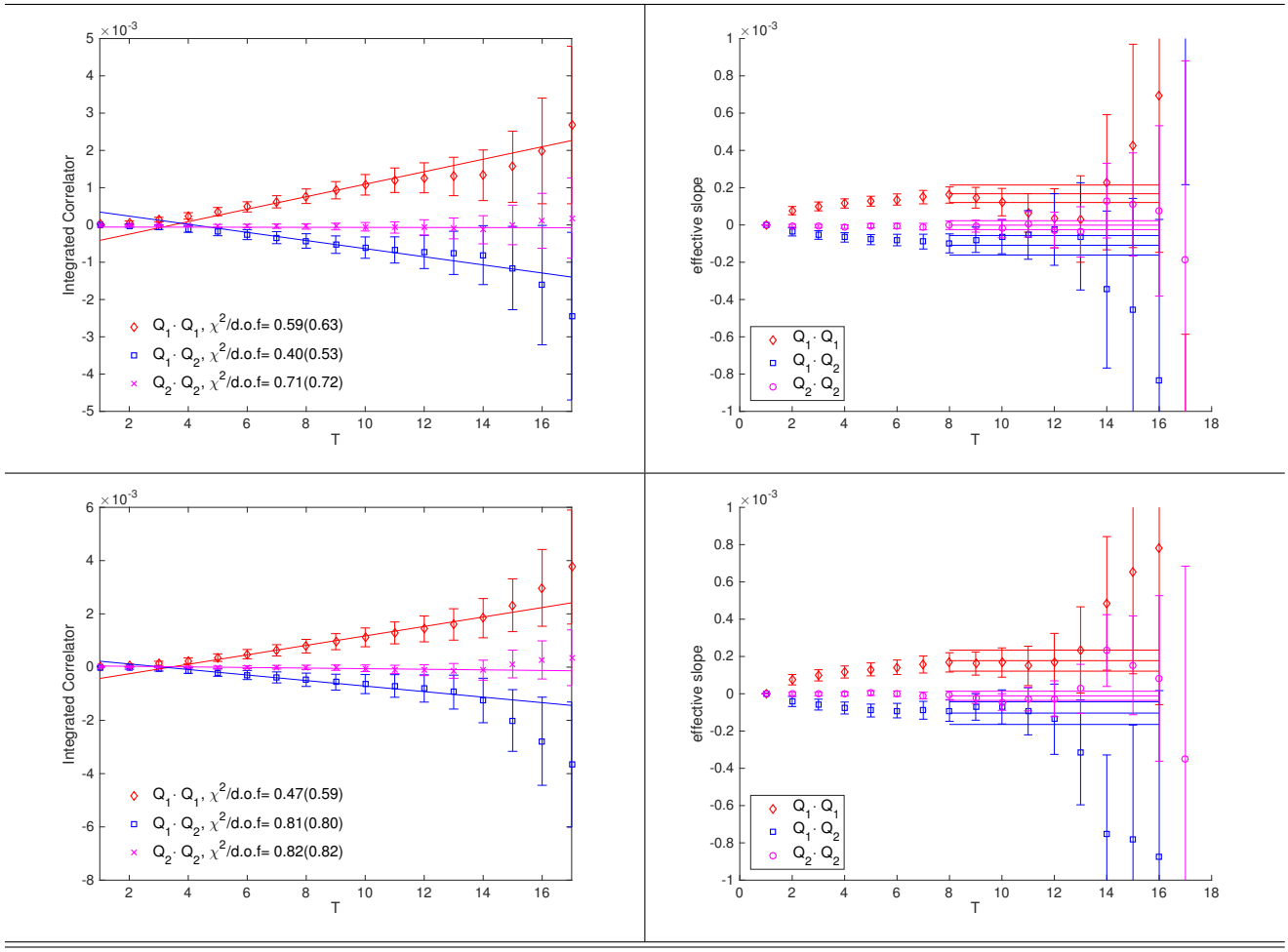

Figure 6.10: Integrated correlator and the effective slope, for type 3/4 diagrams only. The upper panel: $m_c = 750$ MeV, the lower paner: $m_c = 592$ MeV. $T_{min} = 8$ is used.

6.3 Finite volume corrections to ΔM_K

In this calculation, we have considered the physical two-pion intermediate state contribution to ΔM_K, as well as the exponentially growing two-pion contribution which has been subtracted. In this section, we consider a third consequence of the two-pion intermediate state: its contribution to enhanced, finite-volume effect. The finite volume correction given in [29] that must be added to our results is given by:

$$\Delta M_K^{FV} = 2\mathcal{P}\int \mathrm{dE}\,\rho_V(E)\frac{f(E)}{m_k - E} - 2\sum_n \frac{f(E_n)}{m_k - E_n} = -2\left(f(m_K)\cot(h)\frac{\mathrm{dh}}{\mathrm{dE}}\right)_{m_K} \quad (6.6)$$

$$f(m_K) = {}_V\langle \bar{K^0}|H_W|\pi\pi_{E=m_K}\rangle_V\ {}_V\langle\pi\pi_{E=m_K}|H_W|K_0\rangle_V, \quad (6.7)$$

$$h(k) = \delta(k) + \phi(k), \quad (6.8)$$

where the $\delta(k)$ is the s-wave phase shift, and $\phi(k)$ is the kinematic function defined in [30]. Because for the $I = 2$ $\pi\pi$ state, $f(m_K)$ is suppressed by roughly two orders of magnitude, we therefore consider only the $I = 0$ $\pi\pi$ state here. Note, the finite-volume quantization condition is:

$$h(E, L) = n\pi, \quad (6.9)$$

$$E^2 = 4(m^2 + k^2), \quad q = kL/2\pi. \quad (6.10)$$

We use the formulae in [31] to calculate the kinematic function $\phi(q)$, and we impose $n = 0$ to get the scattering phase $\delta(k)$. The last term in Eq. 6.6 is evaluated at $E_{\pi\pi} = M_K$, and we have:

$$\frac{dh}{dE} = \frac{q\phi'(q) + k\delta'(k)}{4\pi k^2}E. \quad (6.11)$$

In order to estimate the scattering phase and its derivative at $E_{\pi\pi} = M_K$, we calculate

the scattering length, which is defined as

$$a = \lim_{k \to 0} \frac{\delta_k}{k}. \tag{6.12}$$

This will be a poor approximation but is good enough for an estimate. We use the formulae in [32] to calculate the scattering length:

$$E_{\pi\pi} = 2m_\pi - \frac{4\pi a}{m_\pi L^3} \left\{ 1 + c_1 \frac{a}{L} + c_2 \frac{a}{L}^2 \right\} + O(L^{-6}), \tag{6.13}$$

$$c_1 = 02.837297, \quad c_2 = 6.375182. \tag{6.14}$$

The scattering phase is estimated using a linear extrapolation $\delta(k_{M_K}) = k_{M_K} a$.

$2f(m_K)$	$h = \delta + \phi$	$\cot h$	dh/dE	$\cot h \times dh/dE$	ΔM_K^{FV}
-0.0068(19)	1.79(8)	-0.225(79)	15.7(4)	-3.5(13)	-0.024(11)

Table 6.9: The $I = 0$ $\pi\pi$ contribution to ΔM_K, and the factors entering the finite volume correction. The last term is the finite volume correction to the $K_L - K_S$ mass difference ΔM_K^{FV}, in units of $10^{-12} MeV$.

We see that two-pion intermediate state only contributes only a small fraction of the total ΔM_K, and the corresponding finite volume correction is even smaller (less than 1%). Therefore, our being unable to measure precisely the kaon to two-pion matrix element or to accurrately compute $\delta(k)$ does not give rise to significant statistical error in ΔM_K.

To conclude, we have been able to measure the $K_L - K_S$ mass difference on this $32^3 \times 64$ lattice. We obtain a 10% error with our current 120 measurements, and our results agree with the experimental value within errors. We have included all the intermediate states we need to consider and have calculated the finite volume corrections, which is negligible for this lattice. However, we have unphysical masses for the pions and the charm quark. Thus, we shouldn't view this result as a physical standard model prediction for ΔM_K. The calculation presented in the next chapter should provide a more realistic result.

Chapter 7

ΔM_K from the $64^3 \times 128$ lattice

Finally, we present our most realistic calculation for the ΔM_K with a $64^3 \times 128$ Iwasaki lattice. The inverse lattice spacing is 2.36 GeV and we have physical pions (136 MeV). We have also used a physical charm quark mass in the calculation. Due to the larger inverse lattice spacing, we can expect the discretization errors from the charm quark to be smaller than those in our previous calculations. An estimation of systematic errors is made at the end of this chapter. This calculation is still ongoing but currently we have enough data to produce less than 40% statistical errors.

7.1 Details of simulation

The ensemble I used for the measurement has a 4D dimension of $64^3 \times 128$, and Mobius Fermions have been used to reduce the fifth dimension to 12 with the Mobius parameter $b + c = 2$. The measurement is performed on a 8K BG/Q supercomputer partition. AMA 4.1.4 is used in the measurement so we perform sloppy measurements on some of the configurations and both exact and sloppy measurements on other configurations. It takes about 5 hours for one sloppy measurement and 15 hours for an exact measurement on an 8K BG/Q partition.

In our first set of measurement, we have used 83 gauge configurations starting from Monte

Carlo trajectory 1200, and ending at 2840, with a separation of 20 Monte Carlo steps between each configuration was used. We performed measurements on 72 configurations using a sloppy propagator with a stopping residual of 10^{-4} for the CG. The other 11 configurations are measured using both sloppy and exact propagators, with the exact propagator have a stopping residual 10^{-8}. For those 11 configurations, we solve the propagator with a sloppy stopping condition first, and then we use the result as an initial guess for the exact propagator, so the final cost of the CG is roughly the same as just solving for the exact propagator. Since we used the new method discussed in Section 4.2.3 for the type 4 diagrams, we have to save left part and right part of the type 4 diagram separately. We have only done this for 7 exact configurations and 52 sloppy configurations. In the current analysis, we used only these 59 configurations for the type 3 and type 4 diagrams. We have more measurements where the type 4 diagrams are not saved by the left and right part, we choose to not use them for reason of simplicity. However, we do include all the 11 measurements for type 1&2 diagrams in our super-jackknifed analysis. In future work, we will re-do the type 4 diagrams for the remaining 24 configurations and save them in the proper way that we can perform this advanced analysis on the full 83 configurations.

Since the type 1&2 diagrams are relatively more accurate than the disconnected diagrams, we choose to perform the measurement for the type 1&2 diagrams only on the configurations that we used for the exact measurements. Therefore, we can reduce the cost for the sloppy configurations because we do not have to find the point source propagators that are needed for the type 1&2 diagrams. We also save time from not doing those contractions. We do not have to perform AMA corrections on the type 1&2 diagrams since they are only measured using exact propagators. Another potential benefit is that in future measurements, if we try to measure every 10 trajectories, we can worry less about the autocorrelations between those measurements because the connected type 1&2 diagrams, which tend to have higher auto-correlation, are measured less frequently.

We used a wall source propagator at each time slice for the light quark and strange quark propagators that are used to construct the kaons. In the connected diagrams, we used a point source at each time slice located at $(4t\%L, 4t\%L, 4t\%L, t)$, where % refers to taking the modulus. L is the length of the spacial directions, and t locates the time slice and varies between 0 and 127. In these measurement, we used 2000 eigenvectors obtained from Lanczos algorithm for the light quark. These eigenvectors are used for both low-mode deflation and constructing the All-To-All propagators (A2A) for the self-loop in the type 3&4 diagrams. The high mode part of the self-loop propagators in the type 3&4 diagrams are evaluated stochastically using 60 random hits.

We have saved the left and right part of the type 4 diagrams separately on disk, and can then construct the Green function for the type 4 diagram with all kaon sink-source separations in the analysis. This enables us to use the fitting method introduced in section 4.2.3.

We have used 4 different charm quark masses in the measurement: 0.25, 0.28, 0.31, and 0.34. We are able to use a variety charm masses because solving for the charm propagators is relatively fast. However, with one additional charm quark mass, we do have to spend time performing the contractions for the four-point and three-point functions, which is roughly 1000 seconds for each additional charm quark mass. Overall, on the sloppy measurement, we spend about 1 hour solving the light quark wall source propagators (128 wall sources), 1 hour on the strange quark wall source propagators (128 wall sources), 1 hour on the light quark random volume source propagators (60 hits) and the charm quark random volume source propagators (60 hits, 4 masses) and 1.5 hour on contractions. We also spend about 30 minutes on reading the eigenvectors from disk. On the exact configurations, we spend roughly 3 hours on the light quark wall source propagators, 2 hours on the strange quark wall source propagators, 3.5 hours on the light and charm quark point source propagators (128 point sources), 2 hours on light and charm quark random source propagators, and 4 hours

on contractions (we need to perform the contraction twice, using both sloppy propagators and exact propagators, and we have additional type 1&2 diagrams to compute). We also spend about 30 minutes reading the eigenvectors from disk.

When we perform the analysis, we combine the data using the super-jackknife method (Section 4.2.4). The first set of data is the 52 sloppy measurement. This does not contain data for the connected type 1&2 diagrams. The second set of data comes from the configurations on which we determine the AMA corrections. This also contains the measurements for the type 1&2 diagrams. Our Green's functions are determined by the sloppy measurement + AMA corrections. For each configuration in the first set of data, we use the regular jackknifed data for the sloppy measurement, corrected by the mean value of the AMA corrections, and we only use the mean value for the type 1&2 diagrams. In the second set of data, we use the regular jackknifed data for the AMA corrections, then add to them the mean value of the sloppy measurements, and we also use the regular jackknifed data for the results from the type 1&2 diagrams.

7.2 Results and error breakdown

7.2.1 Meson state and three point functions

We first list the results from fitting the two point functions for the meson masses and $\pi\pi$ energies. The fitting results are listed in Table 7.1 in lattice unit and MeV. The $\pi\pi$ energy with $I = 0$ has a larger statistical error because of the disconnected diagrams. We have shown the effective mass plot for the $\pi\pi$ states in Fig. 7.1 and the η in Fig. 7.2.

We need to fit the three point functions to determine the matrix element $\langle n|H_W|K^0\rangle$ and subtract the exponential term in Eq. 3.18. We can also add the operators $\bar{s}d$ and $\bar{s}\gamma_5 d$ to our weak Hamiltonian and make the contribution of two intermediate states vanish. We have this freedom because these operator can be expressed as a divergence of a current which

K^0	π	η	$\pi\pi_{I=0}$	$\pi\pi_{I=2}$
0.2105(2)	0.0576(1)	0.273(32)	0.1141(8)	0.1150(4)
496.9(7)	135.9(3)	645(75)	266.3(15)	271.4(6)

Table 7.1: Fitting results for meson mass and $\pi - \pi$ energy in both lattice units (top row) and MeV (bottom row).

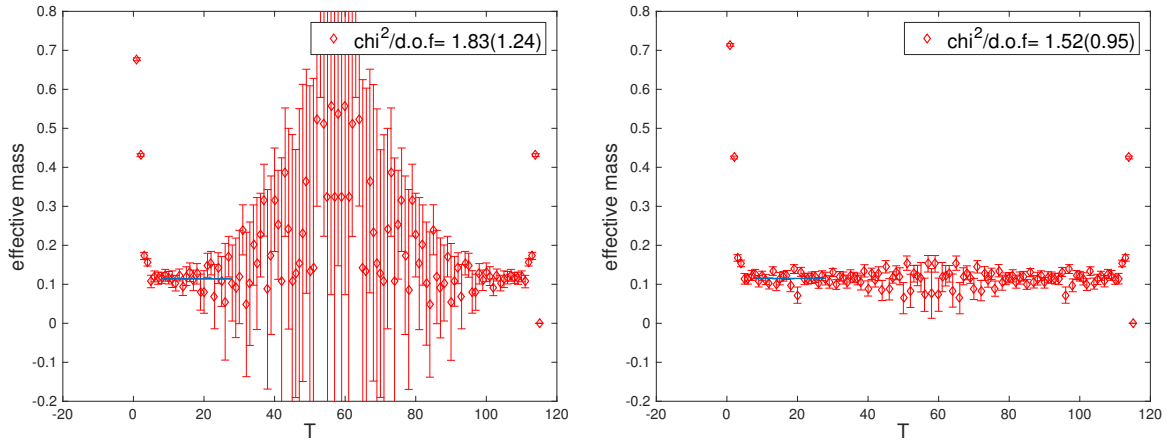

Figure 7.1: The effective mass plots for the $I = 0$ and $I = 2$ $\pi\pi$ states. On the left: I = 0, on the right, I = 2. The plots are symmetric about $T = 58$ since there's a separation of 6 between the two pions in the source and sink.

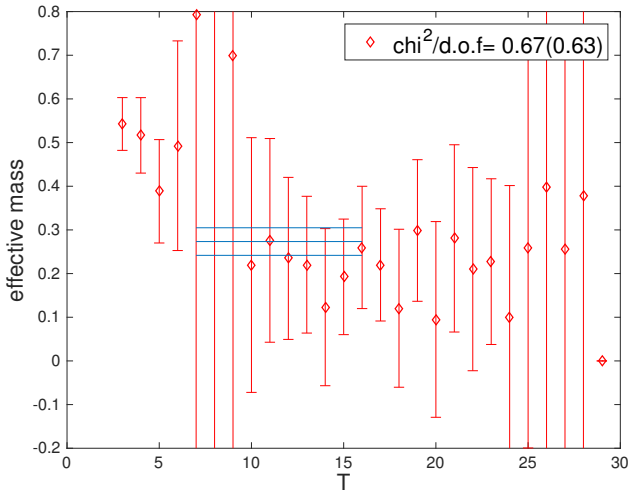

Figure 7.2: The effective mass plot for η states. It is dominated by disconnected diagrams and therefore has large statistical errors.

implies that their contribution to the on-shell kaon mixing matrix element will vanish. The choice of the coefficient of these two operators are the same as we introduced in Chapter 6:

$$\begin{aligned} \langle 0|H_W - c_p \bar{s}\gamma_5 d|K^0\rangle &= 0, \\ \langle \eta|H_W - c_s \bar{s} d|K^0\rangle &= 0. \end{aligned} \tag{7.1}$$

For the ΔM_K calculation, we have only the current-current operators $Q_{1,2}$. We find the coefficients in Eq. 7.1 separately for Q_1 and Q_2. We also quote the matrix elements for the kaon decay into each intermediate states separately for these two operators.

In Table 7.2, we listed the kaon to pion and vacuum matrix element, and in Table 7.3, we listed the coefficients appearing in Eq. 7.1. We list the K to $\pi\pi$ matrix element in Table 7.4. We note for the $I = 0$ matrix element, we have used the weak Hamiltonian with the $\bar{s}\gamma_5 d$ operator subtracted. For the $I = 2$ matrix element, which only involves connected diagrams, the $\bar{s}\gamma_5 d$ operator does not contribute. Since the K to $\pi\pi$ matrix element and the K to η matrix element have large statistical errors, we used the fitting method introduced in Section 4.2.3, and used 5 different source-sink separations (16:6:40). In all of the following tables, we have used $m_c = 0.31$, which is the physical charm quark mass.

$\langle\pi\|Q_1\|K^0\rangle$	$\langle\pi\|Q_2\|K^0\rangle$	$\langle 0\|Q_1\|K^0\rangle$	$\langle 0\|Q_2\|K^0\rangle$
$-5.08(5) \times 10^{-4}$	$1.407(8) \times 10^{-3}$	$-1.289(4) \times 10^{-2}$	$2.454(7) \times 10^{-2}$

Table 7.2: The bare lattice results for K^0 to π matrix element and the K^0 to vacuum matrix element, without subtracting the $\bar{s}d$ operator.

c_s^1	c_s^2	c_p^1	c_p^2
$1.53(64) \times 10^{-4}$	$-2.77(42) \times 10^{-4}$	$-1.476(3) \times 10^{-4}$	$2.811(3) \times 10^{-4}$

Table 7.3: The subtraction coefficients for the scalar and pseudo-scalar operator.

We have shown the $\langle\pi\pi|H_W|K^0\rangle$ as a function of the separation δ between the operator and the $\pi\pi$ sink in Fig. 7.3. For the $I = 0$ channel, where we have the contribution from

$\langle\pi\pi_{I=2}\|Q_1\|K^0\rangle$	$\langle\pi\pi_{I=2}\|Q_2\|K^0\rangle$	$\langle\pi\pi_{I=0}\|Q_1\|K^0\rangle$	$\langle\pi\pi_{I=0}\|Q_2\|K^0\rangle$
$1.451(7)\times10^{-5}$	$1.451(7)\times10^{-5}$	$-6.7(23)\times10^{-5}$	$8.4(26)\times10^{-5}$

Table 7.4: The bare lattice results for K to $\pi\pi$ matrix element for Isospin 0 and 2. The I=2 matrix element for Q_1 and Q_2 are the same because they are from the same three point diagrams.

disconnected diagrams, we expect to get smaller errors for small separation of δ because the three point diagram as shown in Section 4.2.2 is disconnected between the operator and the $\pi\pi$ sink, while the kaon source and the operator are always connected by a quark propagator. The disconnected part between the operator and the sink contribute more noise because the signal falls with increasing δ while the noise does not. Therefore the error bar in Fig. 7.3 increase with δ. In performing this fit, the data for each δ is averaged over different kaon sink and $\pi\pi$ source separations. We have enforced the separation between the kaon source and the operator to be greater than 6 to suppress potential excited-state contamination. We have used a similar method when fitting the η intermediate state to obtain the coefficient c_s. The $\langle\eta|Q_i|K^0\rangle$ has very large statistical errors, and we choose to fit the ratio $\frac{\langle\eta|Q_i|K^0\rangle}{\langle\eta|\bar{s}d|K^0\rangle}$ directly, so we do not have to worry about normalizing these two matrix element using the fitted η meson mass, which is also very noisy. We also benefit from the correlation between these two quantities. The fitting results for this ratio is shown in Fig. 7.4

7.2.2 Results for ΔM_K

In this section, we discuss the final result for ΔM_K with the charm quark mass $m_c = 0.31$. This is closest to the physical charm quark mass, which is obtained from fitting the D_s mass or η_c mass, and has a value $0.32 \sim 0.33$ [33].

The fitting result for ΔM_K is shown in Table 7.5. We have combined all the four types of four point diagrams and used both a correlated fit and an uncorrelated fit to get the result. We also used various fitting ranges to test the consistency of our results. We can separate the results from different types of diagrams and see their separate contributions. We can see that

the error from the type 1&2 diagrams and the type 3&4 diagrams are similar in size, since we measure the type 1&2 diagrams less frequently. Since we only have 11 measurements for the type 1&2 diagrams, we have to use a smaller fitting range when we use a correlated fit. This is because if we use a wider range, we do not have enough samples and the correlation matrix will be singular. We have plotted the integrated four point correlator in Fig. 7.5 and Fig. 7.6, where different fitting method are shown. Using correlated fit for the type 1&2 diagrams gives relative large χ^2 and very large error on the χ^2. Also, the fitting does not seem to give a reasonable behavior. So we currently prefer the un-correlated fit since we do not have enough measurements for the type 1&2 diagram.

	ΔM_K	ΔM_K(tp 3&4 only)	ΔM_K(tp 1&2 only)
un-corr, 10:20	5.8(17)	-1.1(12)	7.0(13)
corr, 14:20	6.6(18)	-0.4(14)	8.5(9)
corr, 16:22	5.6(25)	-1.6(21)	7.5(15)

Table 7.5: Results for ΔM_K from different fitting method (in units of $10^{-12} MeV$). The pair of numbers separated by a colon in the first column gives the fitting range.

We also want to see how much the AMA procedure affect our error. Since we used AMA to correct the Green's functions for the type 3&4 diagrams, we can do the analysis using only the mean value of the AMA correction, and ignore all the fluctuation from the AMA correction. The result for ΔM_K without the AMA error is shown in Table. 7.6. We can conclude that the AMA method does not contribute much to the error in our final answer.

	tp 3	tp 3,no AMA	tp 4	tp 4, no AMA
un-corr, 10:20	1.15(38)	1.15(35)	-2.00(114)	-1.93(105)
corr, 14:20	1.18(48)	1.19(45)	-1.26(130)	-1.52(150)
corr, 16:22	1.68(59)	1.67(57)	-3.02(207)	-2.79(243)

Table 7.6: Contribution to ΔM_K from type 3 and type 4 diagrams (in units of $10^{-12} MeV$), with the error from the AMA correction or without the error from the AMA correction.

We saved the results from our type 4 diagrams in a way that allows us to perform the fitting using various source-sink separations. This method was first used in [34]. This

greatly reduces our error from the type 4 diagrams. We also compute the results using the same number of configurations, but only with a single sink-source separation for the type 4 diagrams. This is shown in Table. 7.7. We can see that the statistical error from the type 4 diagrams reduced by a factor of 2 by using this improved fitting method.

	tp 4 (OneSep)	ΔM_K(OneSep)	tp 4 (MultSep)	ΔM_K(MultSep)
un-corr,10:20	-4.1(25)	3.9(29)	-2.1(12)	5.8(17)
corr,14:20	-4.2(26)	3.8(33)	-1.2(13)	6.6(18)
corr,16:22	-5.2(32)	3.1(40)	-3.0(21)	5.6(25)

Table 7.7: The result for ΔM_K and the type 4 diagrams contribution from the new method of using multiple source-sink separation and the old method using a single source-sink separation. In units of $10^{-12} MeV$.

7.2.3 m_c dependence

We have included four different results for charm qaurk mass in the calculation and we list the results for ΔM_K in Table 7.8. We can see the charm mass dependence by looking at the jackknifed difference of the results for ΔM_K from different m_c. Since the results are correlated, looking at the jackknifed difference in the ΔM_K can give us smaller errors. We have used 56 configurations instead of 59 since we had some hardware failures and three of those configurations only finished the heavier charm mass.

m_c	0.25	0.28	0.31	0.34
ΔM_K	4.7(19)	5.1(18)	5.5(20)	5.9(21)

Table 7.8: Results for ΔM_K calculated from different charm quark masses. We used uncorrelated fit with the fitting range 10:20. The charm quark masses are bare lattice numbers and the ΔM_K are in units of 10^{-12} MeV.

One of the reasons we want to use multiple charm quark mass is the worry that the Domain Wall Fermions action might becomes unphysical when the fermion mass become heavy. It has been shown that $f_{q\bar{q}}$ behavior become sick when the fermions mass is close to 0.4. This behavior results from unphysical states propagating in the fifth dimension with

m_c	0.28	0.31	0.34
ΔM_K	0.38(66)	0.78(65)	1.23(80)

Table 7.9: The jackknifed differences between ΔM_K calculated from different charm quark masses and ΔM_K from $m_c = 0.25$. We used un-correlated fit with the fitting range 10:20. The charm quark masses are bare lattice numbers and the ΔM_K are in units of 10^{-12} MeV.

masses similar to the physical domain wall states. However, based on the results in Table. 7.8 and Table 7.9, we see there is a linear increase of the results for ΔM_K as we increase the charm quark mass, showing no sign of unphysical behavior.

7.2.4 Finite volume corrections

We estimate the finite volume corrections are similar as we did in Chapter 6. Here we just give the results. We first quote the $\pi\pi_{I=0}$ phase shift we estimated at $E(\pi\pi_{I=0}) = m_{K^0}$:

$$\delta(m_{K^0}) = 16.7(47). \tag{7.2}$$

The relevant terms for the finite volume correction are listed in Table 7.10. We can see there is a large enhancement for the $f(m_K)$ from the term $\cot h \times dh/dE$. The final finite volume correction is one magnitude larger than we found in the 32^3 calculation, although this term is not accurately determined.

$2f(m_K)$	$h = \delta + \phi$	$\cot h$	dh/dE	$\cot h \times dh/dE$	$\Delta M_K(FV)$
-0.0026(15)	-0.32(8)	-3.07(85)	34.7(6)	-106(31)	-0.27(18)

Table 7.10: The $\pi\pi_{I=0}$ contribution to ΔM_K, and the terms determining the corresponding finite volume correction. The last term is the finite volume correction to the $K_L - K_S$ mass difference $\Delta M_K(FV)$, in units of $10^{-12} MeV$.

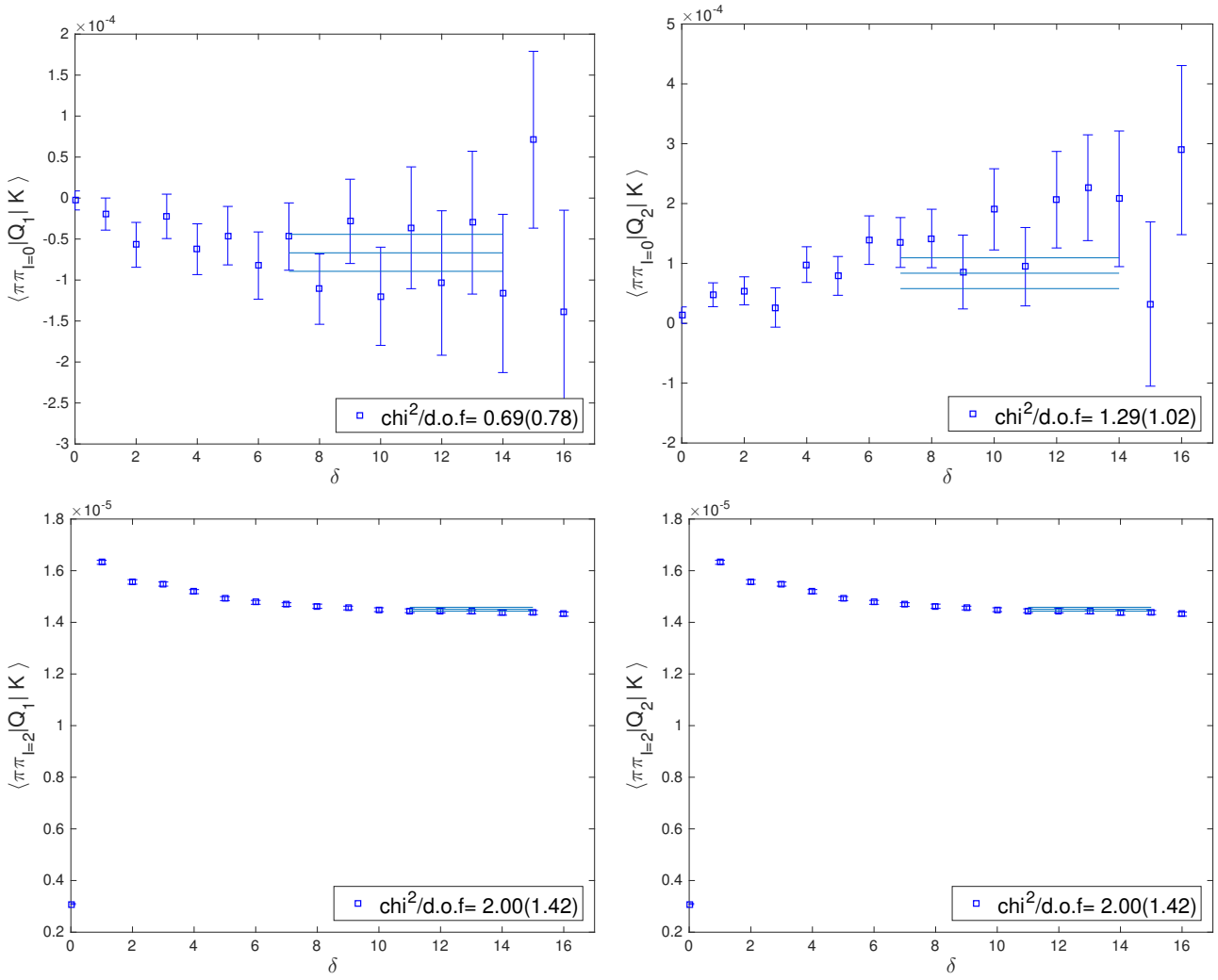

Figure 7.3: The $\langle\pi\pi|Q_i|K\rangle$ matrix element for various $\pi\pi$-operator separation δ. On the left: Q_1, on the right, Q_2.

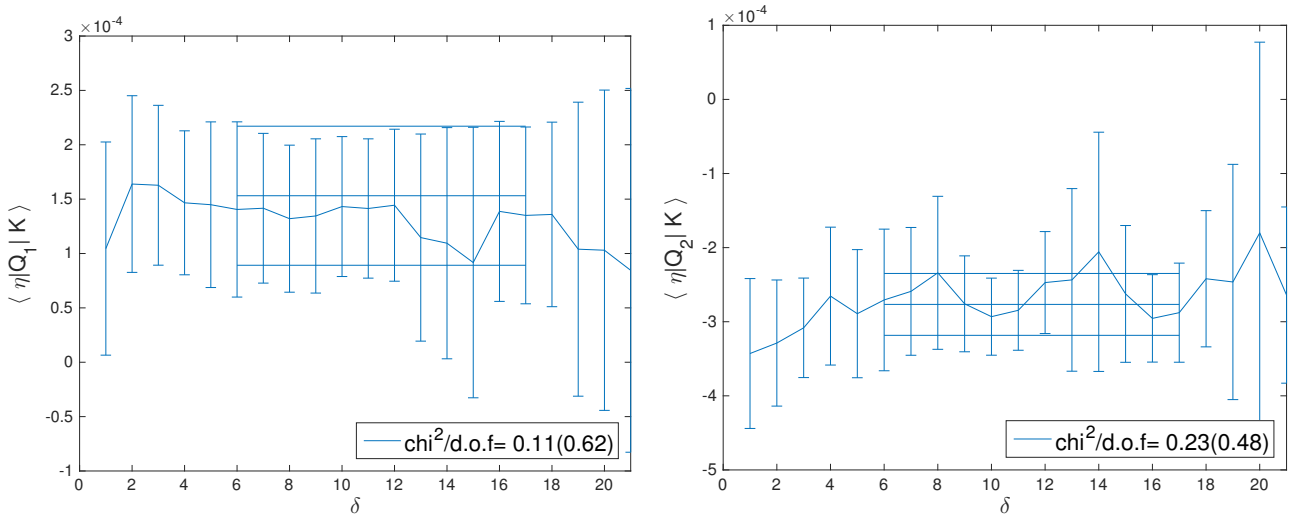

Figure 7.4: $\frac{\langle\eta|Q_i|K\rangle}{\langle\eta|\bar{s}d|K\rangle}$ for various η-operator separations δ. On the left: Q_1, on the right, Q_2.

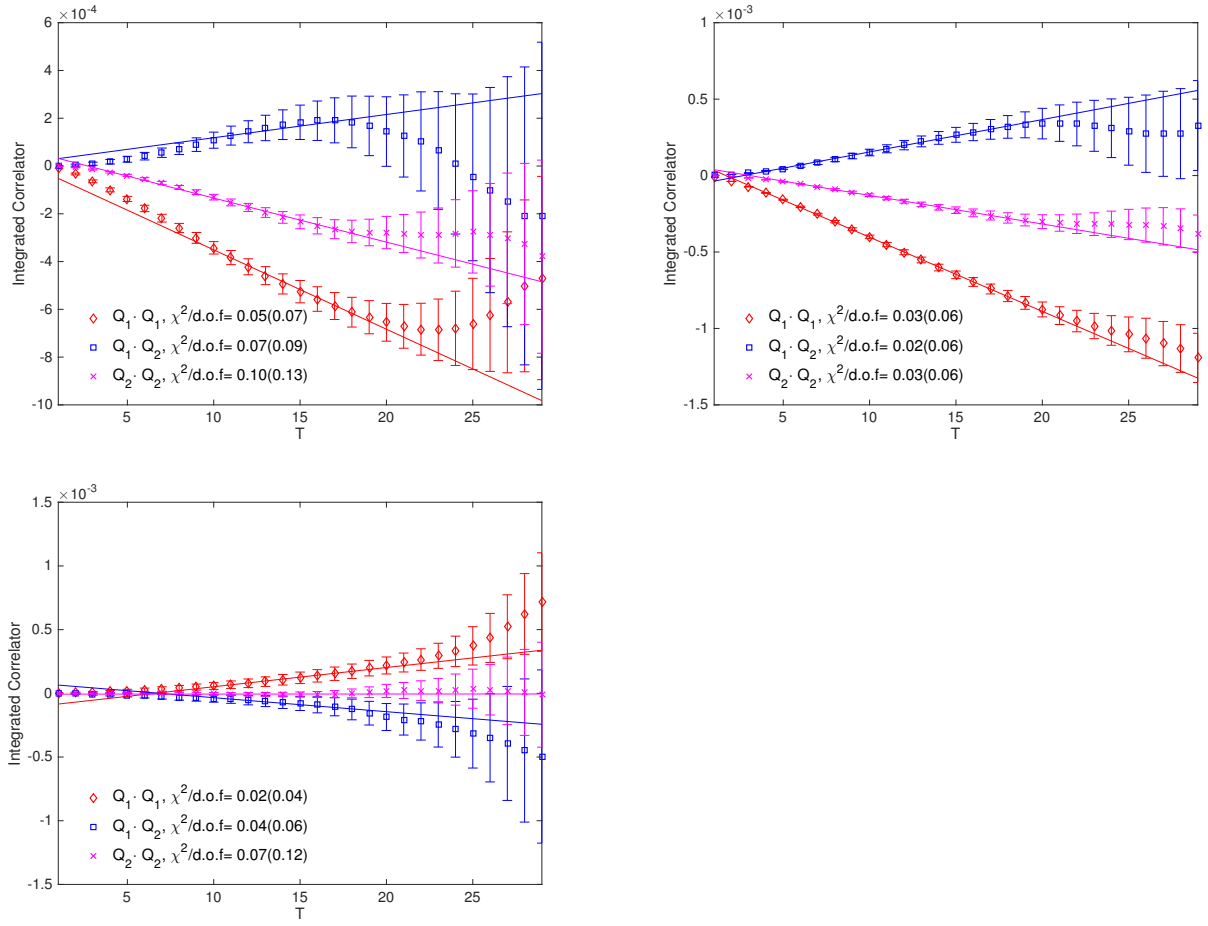

Figure 7.5: The fitting results for the integrated four point correlator. From left to right, top to bottom: All diagrams included, only type 1&2 diagrams included, and only type 3&4 diagrams included. From un-correlated fit using the range using the range 10:20.

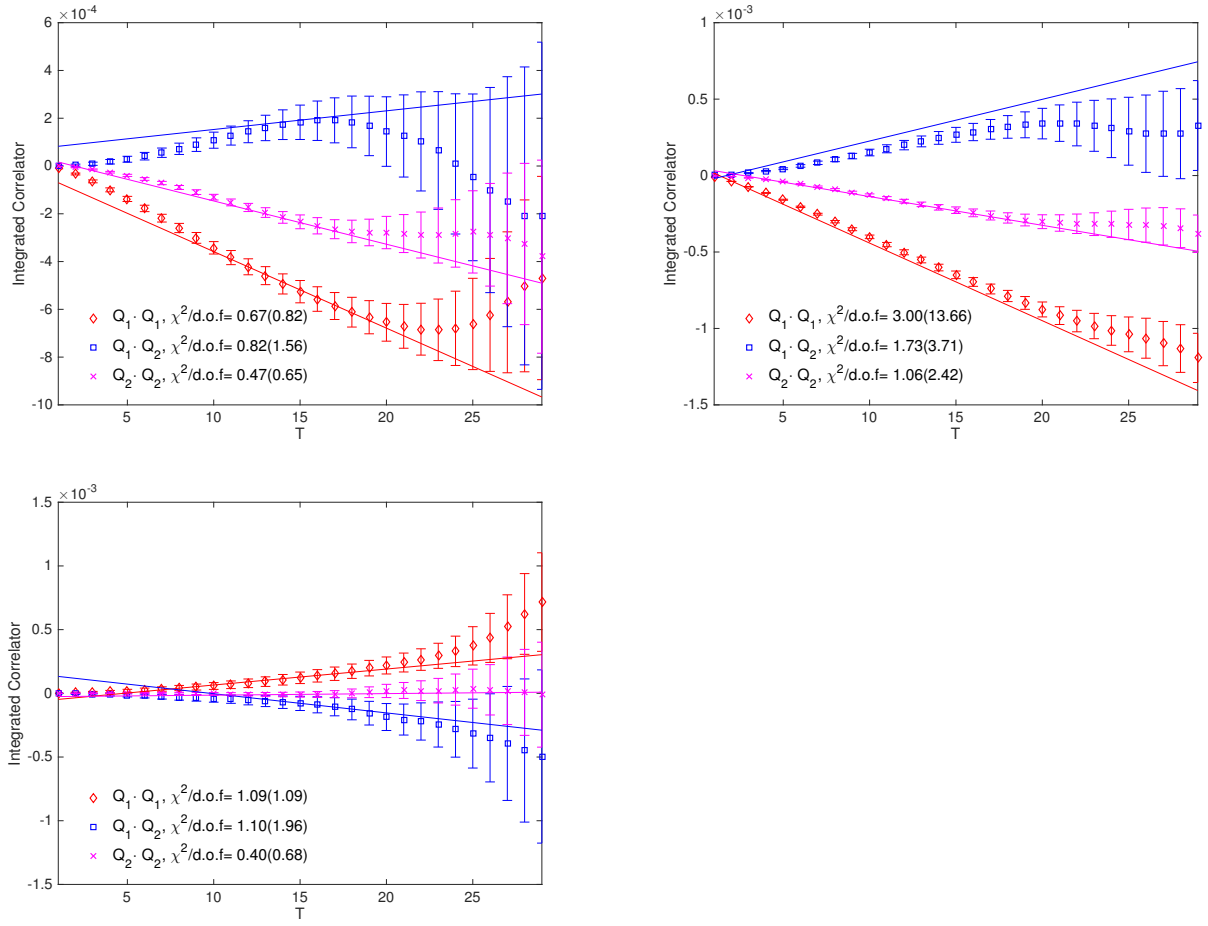

Figure 7.6: The fitting results for the integrated four point correlator. From left to right, top to bottom: All diagrams included, only type 1&2 diagrams included, and only type 3&4 diagrams included. From correlated fit using the range 16:22.

7.3 Conclusion

We have used 59 measurements in the analysis and we obtained

$$\Delta M_K^{FV} = 5.8(17) \times 10^{-12} \text{ MeV}. \tag{7.3}$$

Including the finite volume correction, we can obtain the infinite volume result (adding the errors in quadrature):

$$\Delta M_K = 5.5(17) \times 10^{-12} \text{ MeV}. \tag{7.4}$$

We used four different charm masses in this calculation, and we did not see any unphysical behavior in the result caused by our heavy charm quark mass with DWF action. Our future plans include finishing this calculation with 160 measurements so we can get a statistical error ~ 1.0, which is about 20% of the current results for ΔM_K. The systematic error can be evaluated simply by $(m_c a)^2$, which give us 25%. We can also estimate the systematic error using the dispersion relations in Appendix D. We can see in the typical energy scale around 1 GeV, the dispersion relation calculated with the charm mass 0.31 indicate 10% deviation from unity, which indicate a similar size systematic error.

One important ongoing project is to improve the fermion action. We have used DWF action for the fermions and it is known that for a sufficiently heavy quark mass the DWF action might be problematic. We are working on improved fermion actions that we will use in future calculations. cancellation.

Chapter 8

Conclusion

In this work, we have demonstrated our approach to evaluate the long distance contributions to second order, $K^0 - \bar{K}^0$ mixing. We have shown the calculation of two important and related quantities, ΔM_K and ϵ_K. The mass difference ΔM_K involves more contribution from long distance effects and therefore a lattice calculation is necessary to obtain a reliable estimation from the Standard Model, since a perturbation theory calculation may give large systematic errors. We began the ΔM_K calculation on a $16^3 \times 32$ lattice with inverse lattice spacing 1.78GeV, and gradually increased the physical volume and approached physical quark masses. Now we are able to evaluate this quantity using physical kinematics, enabling us to obtain a physical results that we can compare with experimental value. Although this physical calculation is still ongoing, we are able to get $\sim 30\%$ statistical errors and obtain

$$\Delta M_K = 5.5(17) \times 10^{-12} \text{ MeV}.$$

The ϵ_K, on the other hand, is dominated by short distance effects. We have shown that although the long distance contribution is small, it is however necessary to determine if we want a complete estimation based on Standard Model. The lattice QCD calculation of ϵ_K is more challenging due to the short-distance divergence in both the lattice calculation and the

perturbation theory calculations. We have presented our approach to remove this divergence by introducing an extra energy scale and a Regularization Independent (RI) scheme. In this work, we have performed the first calculation of the long-distance contribution to ϵ_K from lattice QCD, where unphysical kinematics are used. We are able to estimate the size of the long distance contribution in ϵ_K, despite large statistical errors and systematic errors due to unphysical quark masses. In this unphysical calculation, we obtained the long distance correction to ϵ_K (only statistical errors are included):

$$\epsilon_K^{ld\,corr} = 0.108(76) \times 10^{-3}.$$

Our first future plan will include a physical calculation of ΔM_K with less than 20% statistical error. This can be achieved by extending the calculation in Chapter 7 to obtain ~ 160 measurements. This is three times the current statistics and a less than 20% statistical error can be expected. The second plan is the study of a better DWF action that may allow us to use a physical charm mass without worrying about unphysical states from the Domain Wall Fermion action. The third plan is to start a new, physical calculation for the ϵ_K. This requires more computer time since the measurements for ϵ_K is about twice as hard as ΔM_K, and with the same amount of measurements, we might have a larger statistical error for ϵ_K because it involves the right-handed vertices. Right-handed vertices couple to vacuum much more strongly than the left-handed vertices, and this requires us to obtain more measurements in order to get a similar statistical error compared to ΔM_K.

Bibliography

[1] Z. Bai, N. Christ, T. Izubuchi, C. Sachrajda, A. Soni, *et al.*, Phys.Rev.Lett. **113**, 112003 (2014), 1406.0916.

[2] A. Bevan *et al.*, Nucl. Phys. Proc. Suppl. **241-242**, 89 (2013).

[3] A. Alberti, P. Gambino, K. J. Healey, and S. Nandi, Phys. Rev. Lett. **114**(6), 061802 (2015), 1411.6560.

[4] Z. Bai *et al.* (RBC, UKQCD), Phys. Rev. Lett. **115**(21), 212001 (2015), 1505.07863.

[5] J. Brod and M. Gorbahn, Phys. Rev. Lett. **108**, 121801 (2012), URL `http://link.aps.org/doi/10.1103/PhysRevLett.108.121801`.

[6] A. J. Buras and J. Girrbach, Eur. Phys. J. **C73**(9), 2560 (2013), 1304.6835.

[7] J. A. Bailey, Y.-C. Jang, W. Lee, and S. Park (SWME), Phys. Rev. **D92**(3), 034510 (2015), 1503.05388.

[8] C. Patrignani *et al.* (Particle Data Group), Chin. Phys. **C40**(10), 100001 (2016).

[9] T. Inami and C. Lim, Prog.Theor.Phys. **65**, 297 (1981).

[10] G. Buchalla, A. J. Buras, and M. E. Lautenbacher, Rev. Mod. Phys. **68**, 1125 (1996), URL `http://link.aps.org/doi/10.1103/RevModPhys.68.1125`.

[11] J. A. Bailey, Y.-C. Jang, W. Lee, and S. Park (SWME) (2015), 1503.06613.

[12] S. Duane, A. Kennedy, B. Pendleton, and D. Roweth, Phys.Lett. **B195**, 216 (1987).

[13] Y. Iwasaki, Nucl.Phys. **B258**, 141 (1985).

[14] H. Rothe, World Sci.Lect.Notes Phys. **43**, 1 (1992).

[15] H. Yin, Phd Thesis .

[16] J. Foley, K. Jimmy Juge, A. O'Cais, M. Peardon, S. M. Ryan, and J.-I. Skullerud, Comput. Phys. Commun. **172**, 145 (2005), hep-lat/0505023.

[17] T. Kaneko, S. Aoki, G. Cossu, H. Fukaya, S. Hashimoto, J. Noaki, and T. Onogi (JLQCD), PoS **LATTICE2010**, 146 (2010), 1012.0137.

[18] T. Blum, T. Izubuchi, and E. Shintani, Phys. Rev. **D88**(9), 094503 (2013), 1208.4349.

[19] J. D. Bratt *et al.* (LHPC), Phys. Rev. **D82**, 094502 (2010), 1001.3620.

[20] A. J. Buras, D. Guadagnoli, and G. Isidori, Phys.Lett. **B688**, 309 (2010), 1002.3612.

[21] N. Christ, T. Izubuchi, C. Sachrajda, A. Soni, and J. Yu (RBC, UKQCD), Phys.Rev. **D88**, 014508 (2013), 1212.5931.

[22] G. Martinelli, C. Pittori, C. T. Sachrajda, M. Testa, and A. Vladikas, Nucl.Phys. **B445**, 81 (1995), hep-lat/9411010.

[23] N. H. Christ, X. Feng, A. Portelli, and C. T. Sachrajda (RBC, UKQCD), Phys. Rev. **D93**(11), 114517 (2016), 1605.04442.

[24] Y. Aoki *et al.* (RBC, UKQCD), Phys.Rev. **D83**, 074508 (2011), 1011.0892.

[25] T. Blum *et al.* (RBC, UKQCD) (2014), 1411.7017.

[26] J. Yu, Phd Thesis .

[27] N. Christ, C. Dawson, T. Izubuchi, C. Jung, Q. Liu, *et al.*, Phys.Rev.Lett. **105**, 241601 (2010), 1002.2999.

[28] S. Okubo, Physics Letters **5**(2), 165 (1963), ISSN 0031-9163, URL http://www.sciencedirect.com/science/article/pii/S0375960163925489.

[29] N. Christ, G. Martinelli, and C. Sachrajda, PoS **LATTICE2013**, 399 (2014), 1401.1362.

[30] M. Luscher, Nucl.Phys. **B354**, 531 (1991).

[31] T. Yamazaki, S. Aoki, M. Fukugita, K.-I. Ishikawa, N. Ishizuka, Y. Iwasaki, K. Kanaya, T. Kaneko, Y. Kuramashi, M. Okawa, A. Ukawa, and T. Yoshié (CP-PACS Collaboration), Phys. Rev. D **70**, 074513 (2004), URL http://link.aps.org/doi/10.1103/PhysRevD.70.074513.

[32] L. Lellouch and M. Luscher, Commun.Math.Phys. **219**, 31 (2001), hep-lat/0003023.

[33] T. Tsang, NA .

[34] N. H. Christ, X. Feng, A. Juttner, A. Lawson, A. Portelli, and C. T. Sachrajda, Phys. Rev. **D94**(11), 114516 (2016), 1608.07585.

[35] C. Sturm, Y. Aoki, N. H. Christ, T. Izubuchi, C. T. C. Sachrajda, and A. Soni (RBC and UKQCD Collaborations), Phys. Rev. D **80**, 014501 (2009), URL http://link.aps.org/doi/10.1103/PhysRevD.80.014501.

[36] C. Lehner and C. Sturm, Phys. Rev. **D84**, 014001 (2011), 1104.4948.

[37] C. Lehner and C. Sturm, NA .

[38] P. A. Boyle, L. Del Debbio, A. Juttner, A. Khamseh, F. Sanfilippo, and J. T. Tsang (2017), 1701.02644.

Appendix A

All diagrams calculated on the lattice

A.1 All four points diagrams

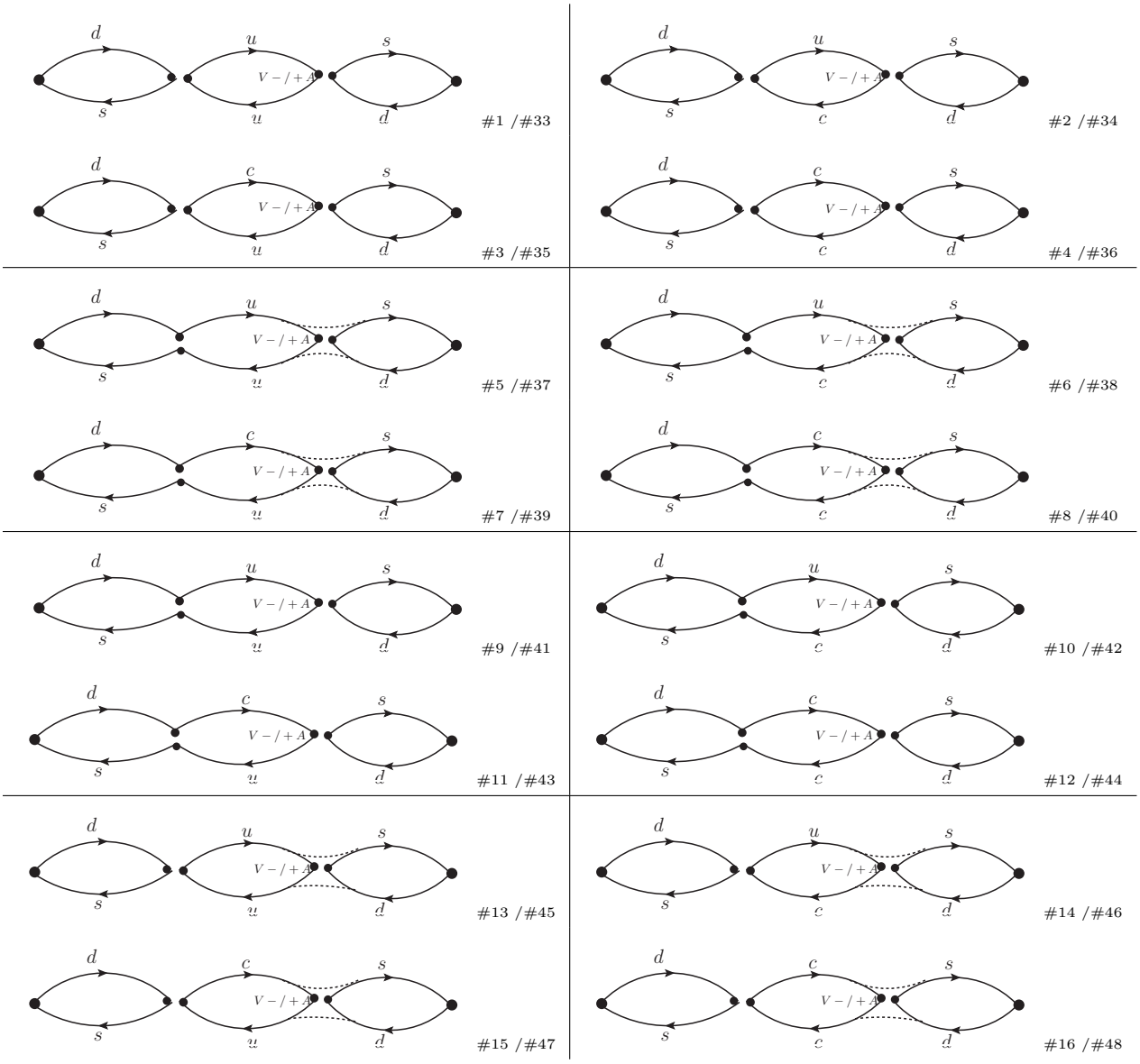

Figure A.1: Contractions for type 1 four point diagrams, all vertices have a V-A structure if no explicit notation is shown. Each diagram represents two different contractions depending on the vertex being marked is a $V-A$ or $V+A$ vertex. The dashed lines represent the contraction of color.

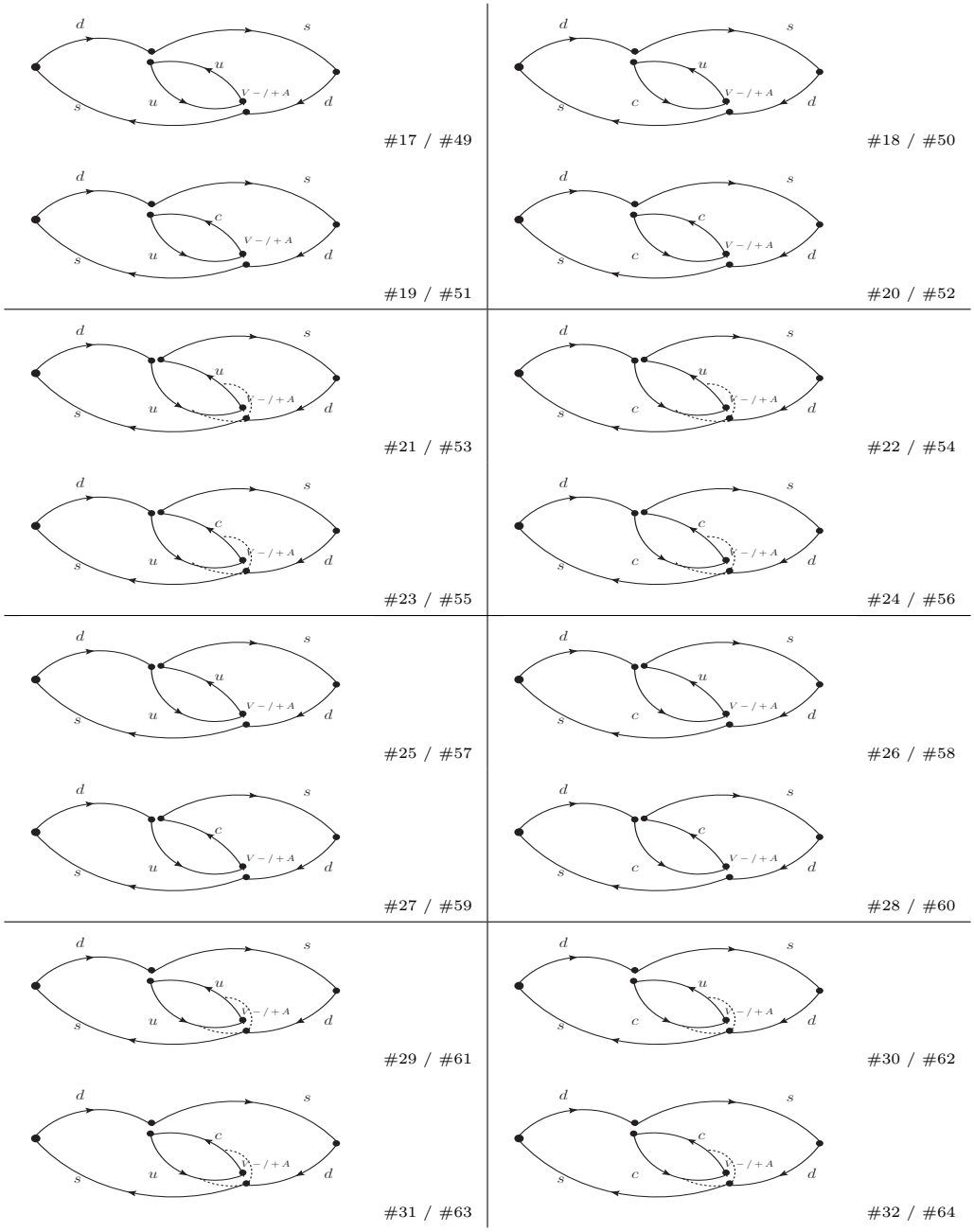

Figure A.2: Contractions for type 2 four point diagrams, all vertex are V-A structure if no explicit notation is shown. Each diagram represents two different contractions depending on the vertex being marked is a $V - A$ or $V + A$ vertex. The dashed lines represent the contraction of color.

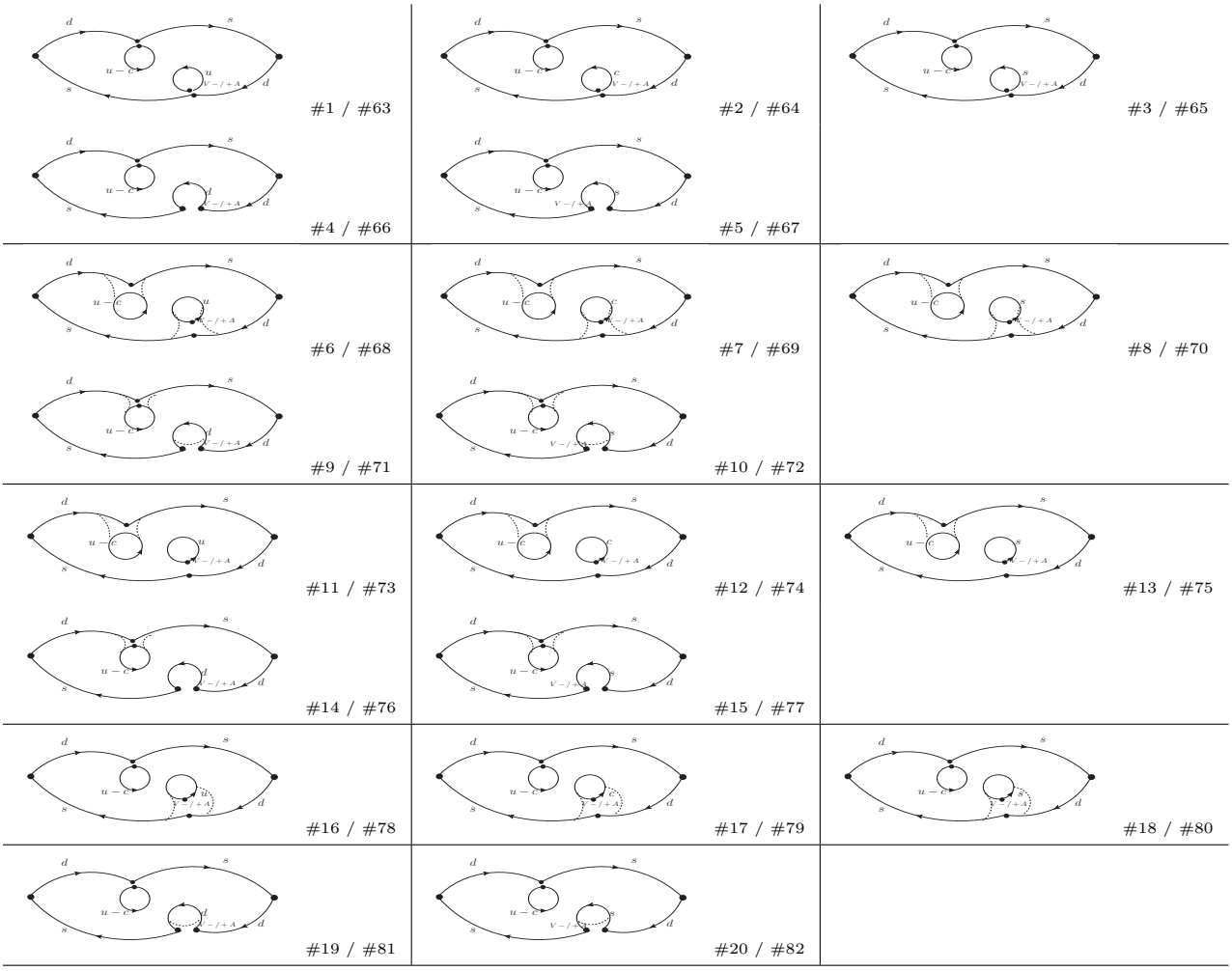

Figure A.3: Contractions for type 3 four point diagrams, all vertex are V-A structure if no explicit notation is shown. Each diagram represents two different contractions depending on the vertex being marked is a $V - A$ or $V + A$ vertex. The dashed lines represent the contraction of color.

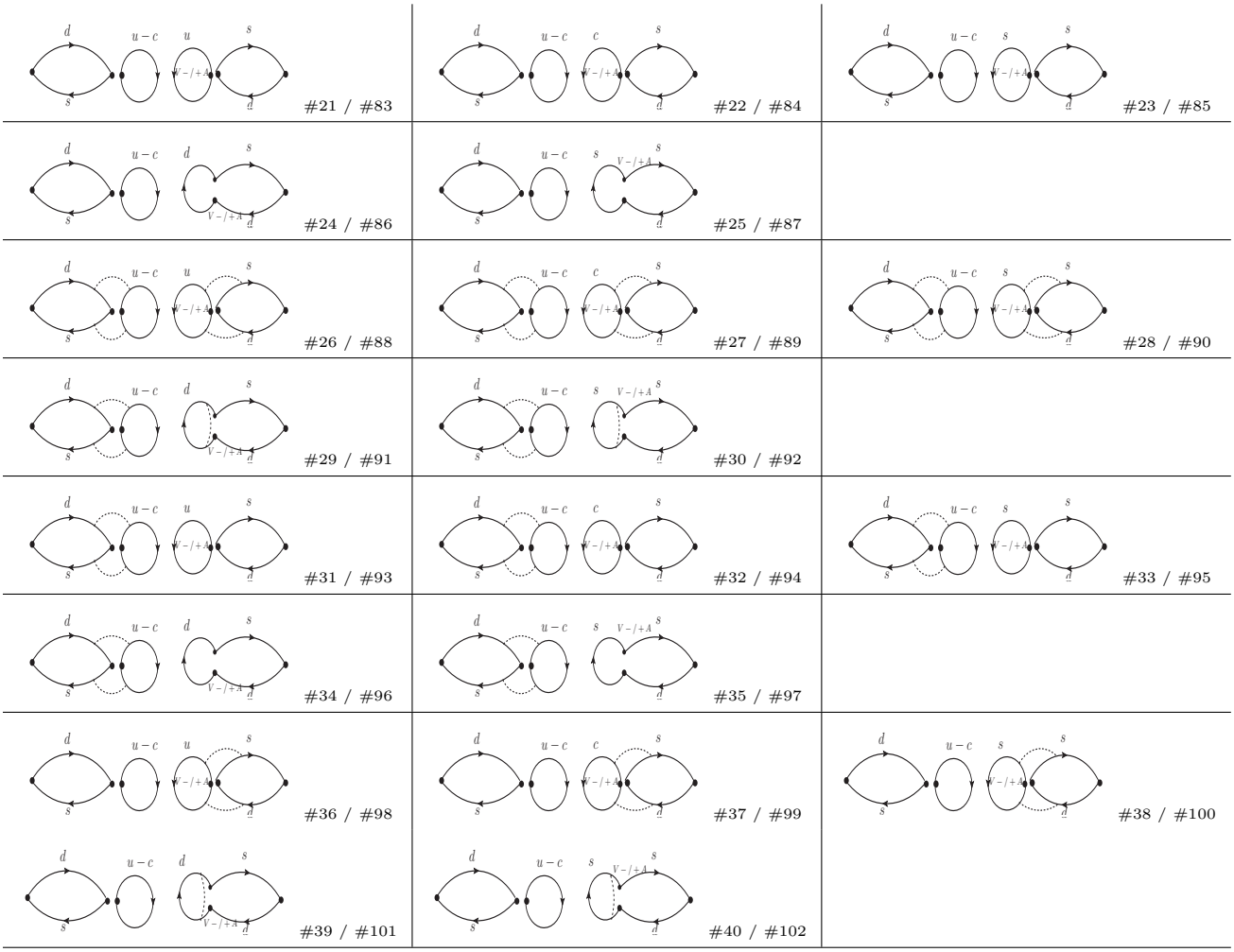

Figure A.4: contractions for type 4 four point diagrams, all vertex are V-A structure if has no explicit notation. Each diagram represents two different contractions depending on the vertex being marked is a $V - A$ or $V + A$ vertex. The dashed lines represent the contraction of color.

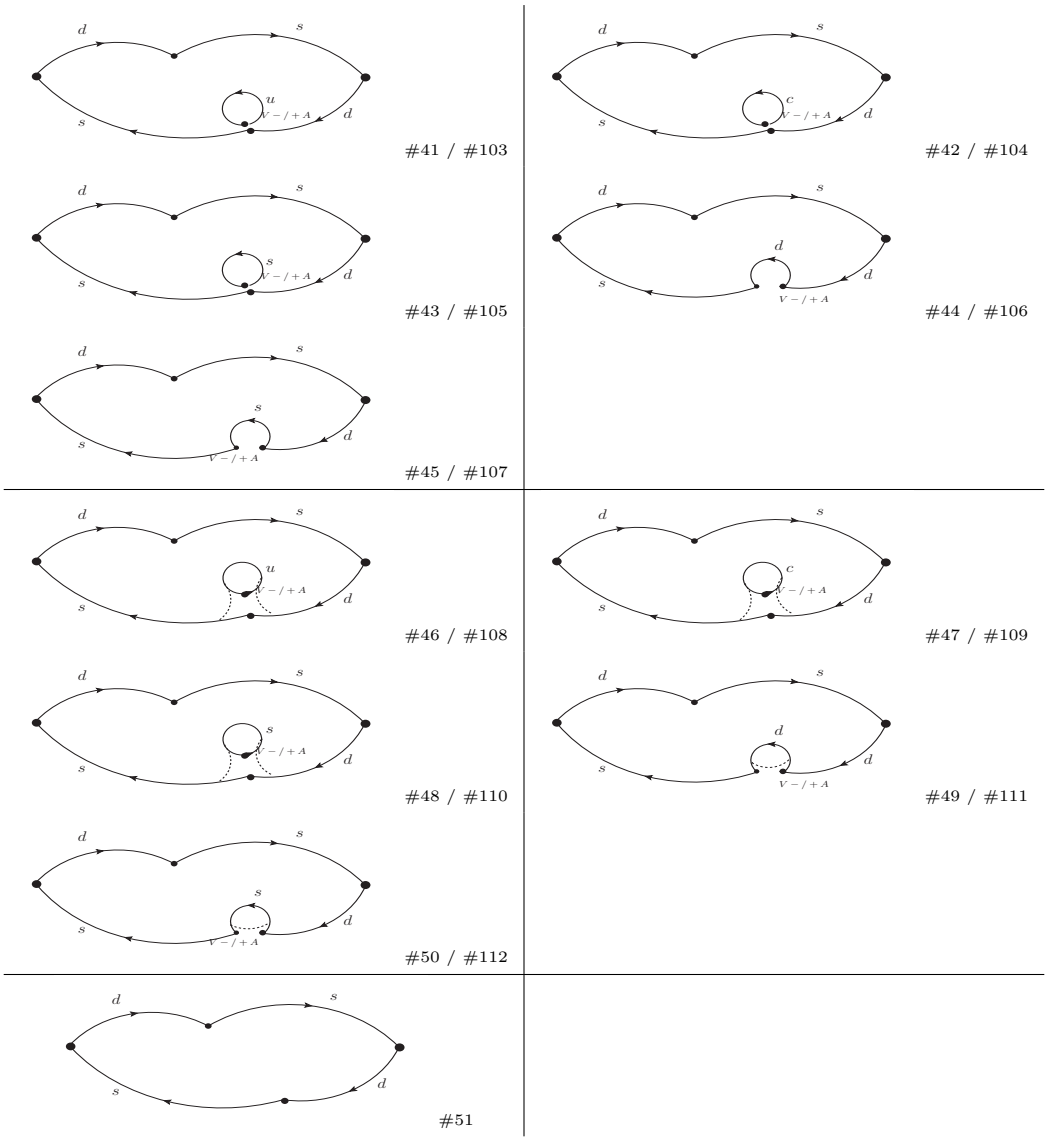

Figure A.5: Contractions for type 3 subtraction four point diagrams. Each diagram represents two different contractions depending on the vertex being marked is a $V - A$ or $V + A$ vertex. The dashed lines represent the contraction of color.

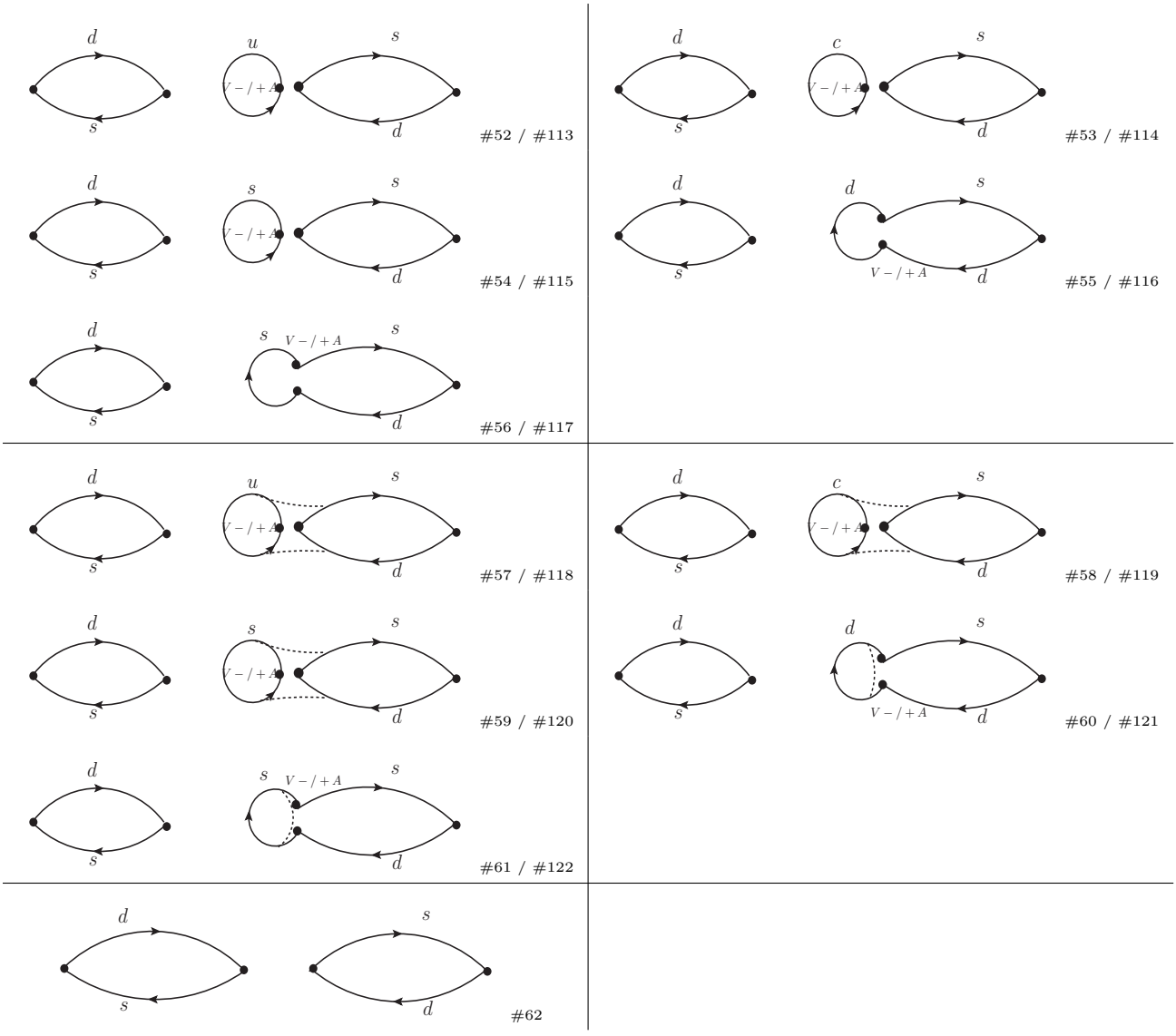

Figure A.6: contractions for type 4 subtraction four point diagrams. Each diagram represents two different contractions depending on the vertex being marked is a $V-A$ or $V+A$ vertex. The dashed lines represent the contraction of color.

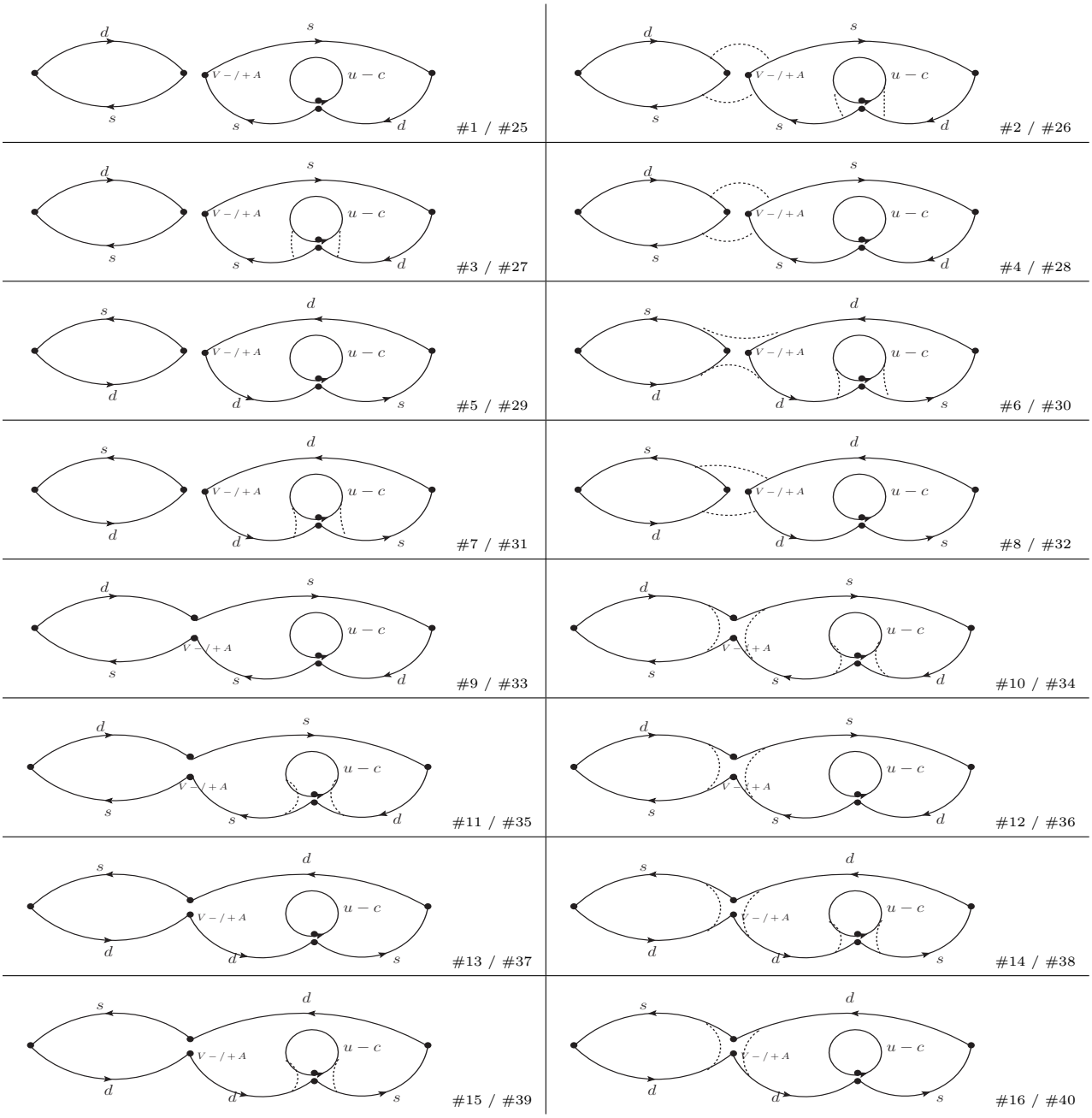

Figure A.7: Contractions for type 5 four point diagrams, all vertex are V-A structure no explicit notation is shown. Each diagram represents two different contractions depending on the vertex being marked is a $V-A$ or $V+A$ vertex. The dashed lines represent the contraction of color.

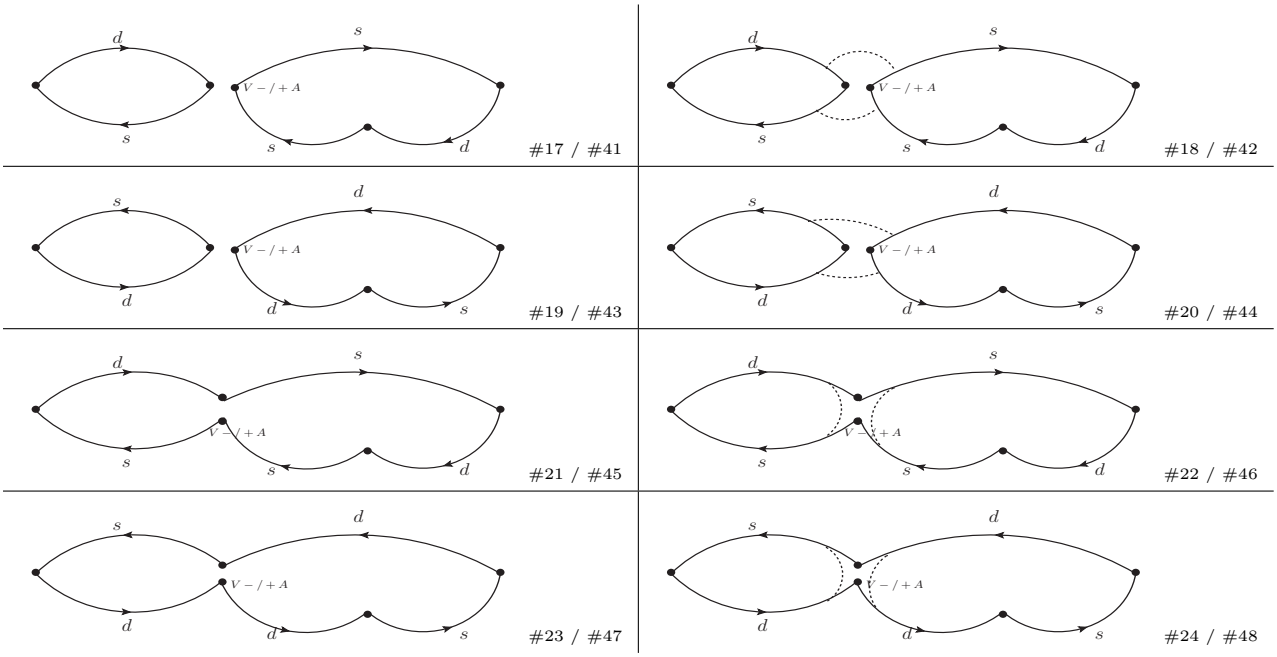

Figure A.8: Contractions for type 5 subtraction diagrams. Each diagram represents two different contractions depending on the vertex being marked is a $V-A$ or $V+A$ vertex. The dashed lines represent the contraction of color.

A.2 All three point diagrams

We show the contractions of all relevant three point diagrams, $k \to \pi\pi$ contractions are not included here.

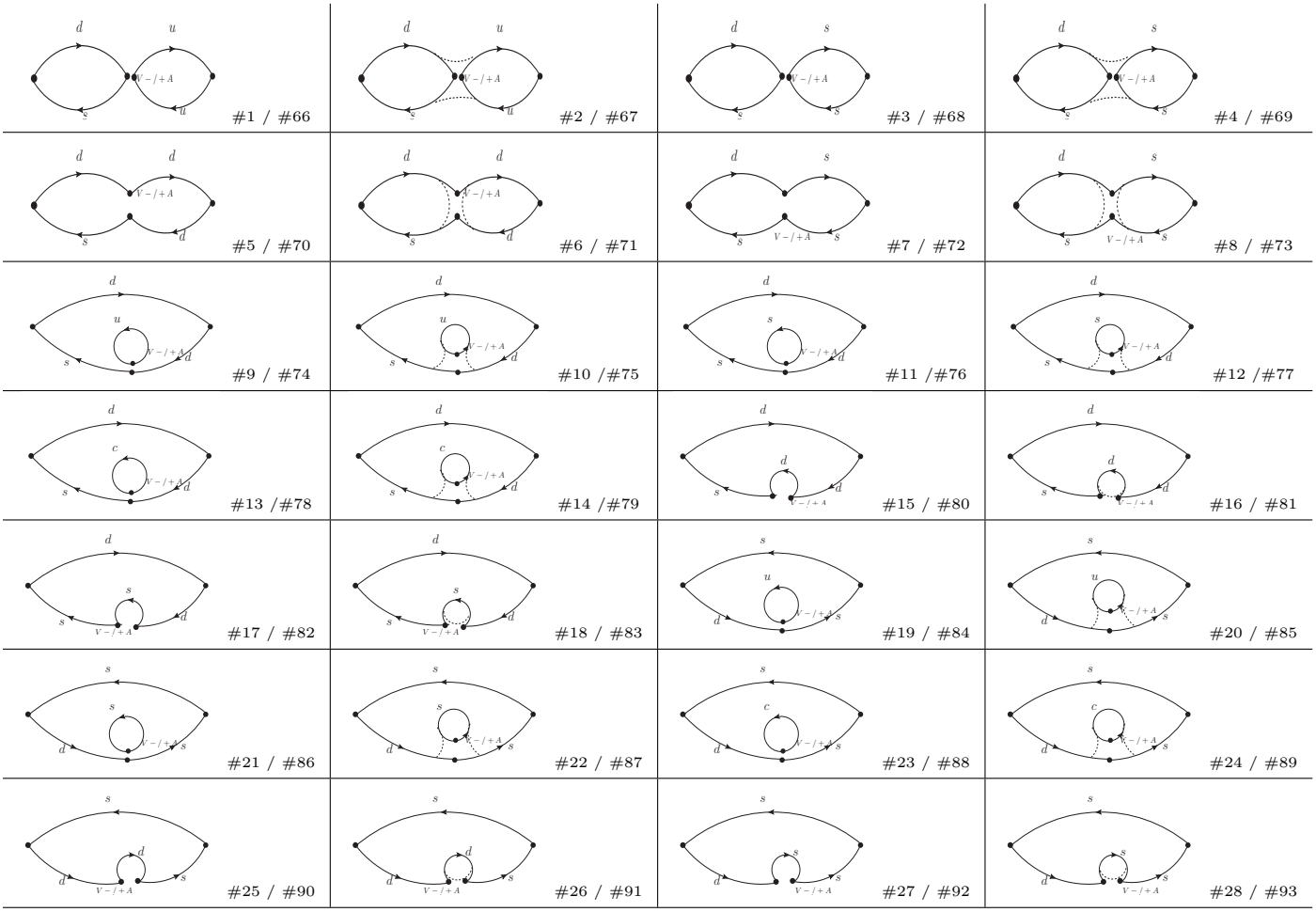

Figure A.9: 3 point diagrams. The dashed lines represent contraction of colors. Each diagram represents two different contractions depending on the vertex being marked is a $V-A$ or $V+A$ vertex.

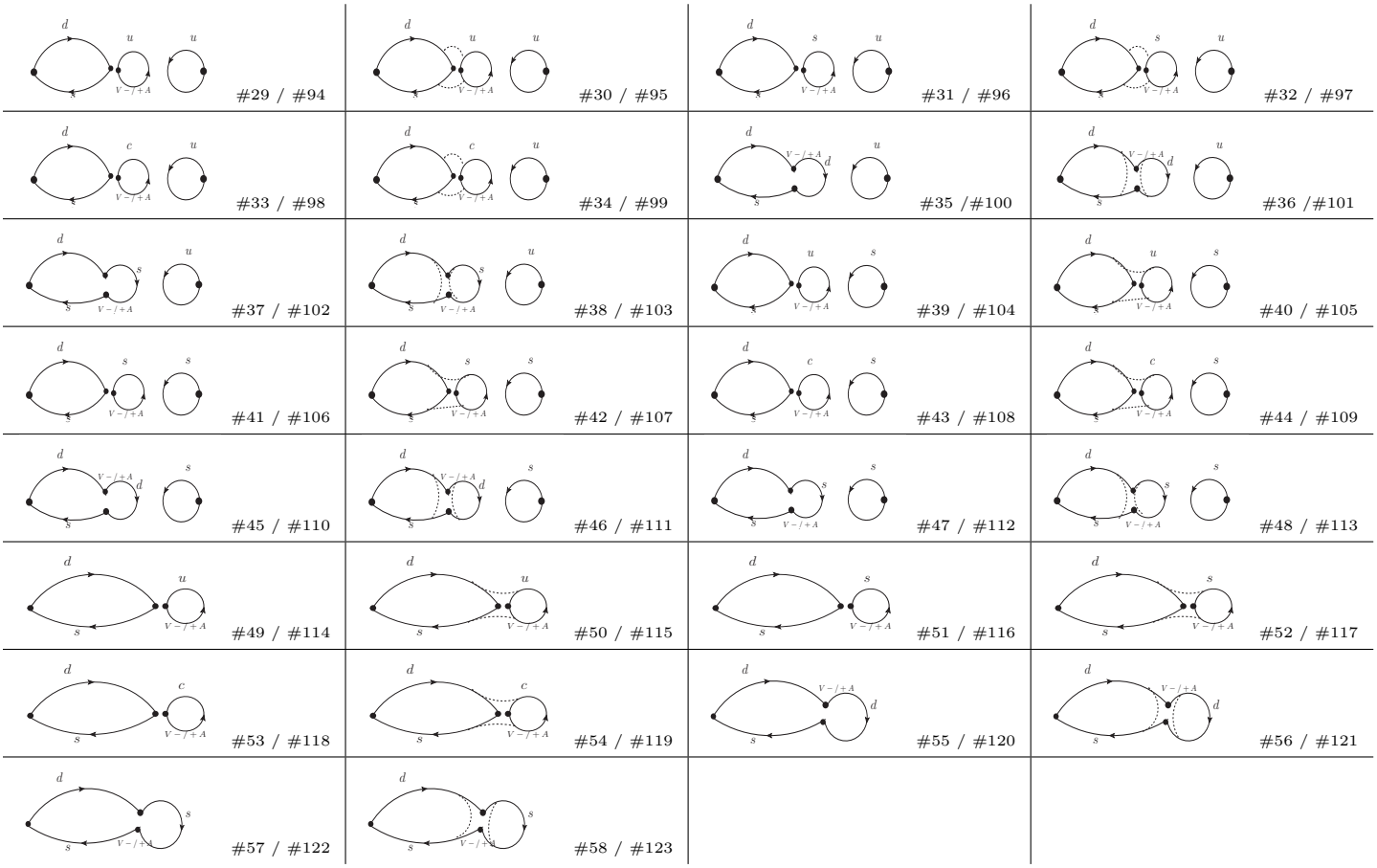

Figure A.10: 3 point diagrams(continued). The dashed lines represent contraction of color. Each diagram represents two different contractions depending on the vertex being marked is a $V - A$ or $V + A$ vertex.

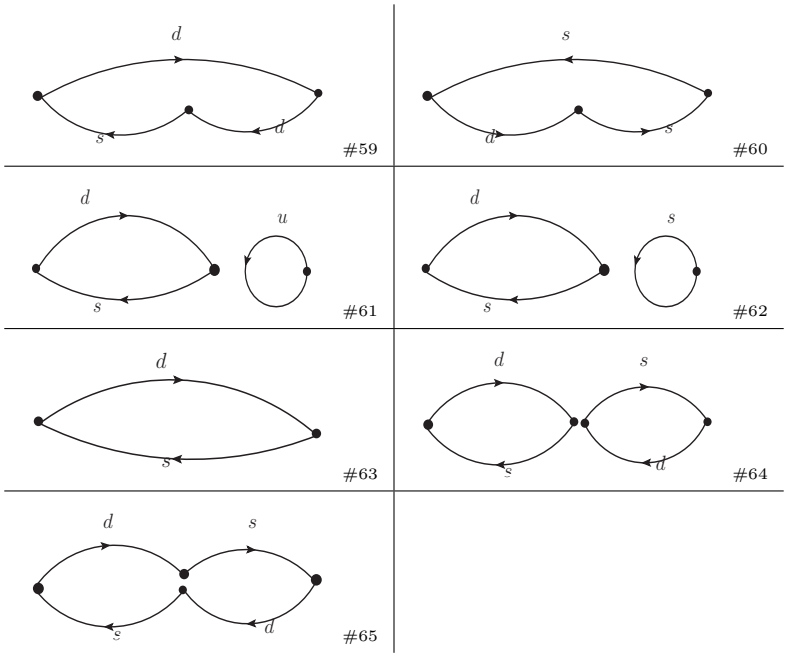

Figure A.11: 3 point diagrams(continued). The dashed lines represent contraction of colors. Each diagram represents two different contractions depending on the vertex being marked is a $V - A$ or $V + A$ vertex.

A.3 All K to $\pi\pi$ diagrams

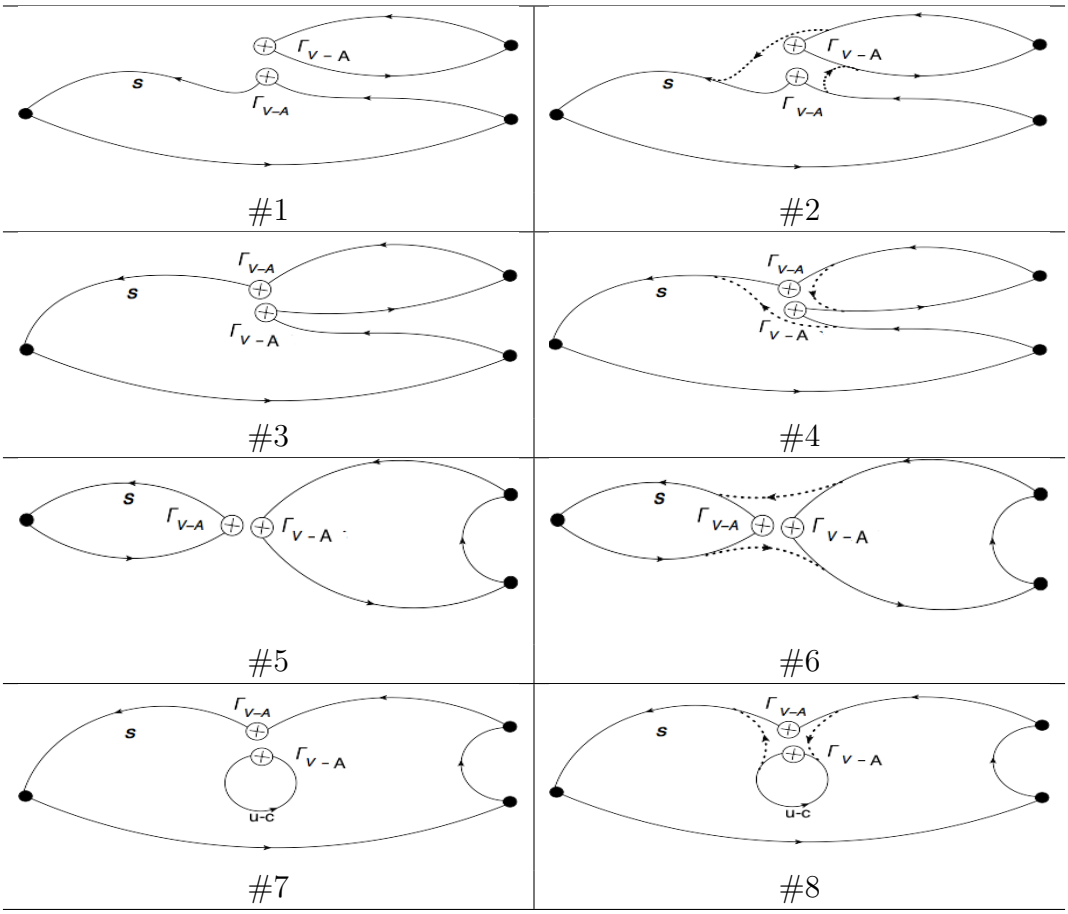

Figure A.12: Contractions for $K \to \pi\pi$ diagrams. Only Q_1 and Q_2 are included. The vertex is a $V - A$ vertex.

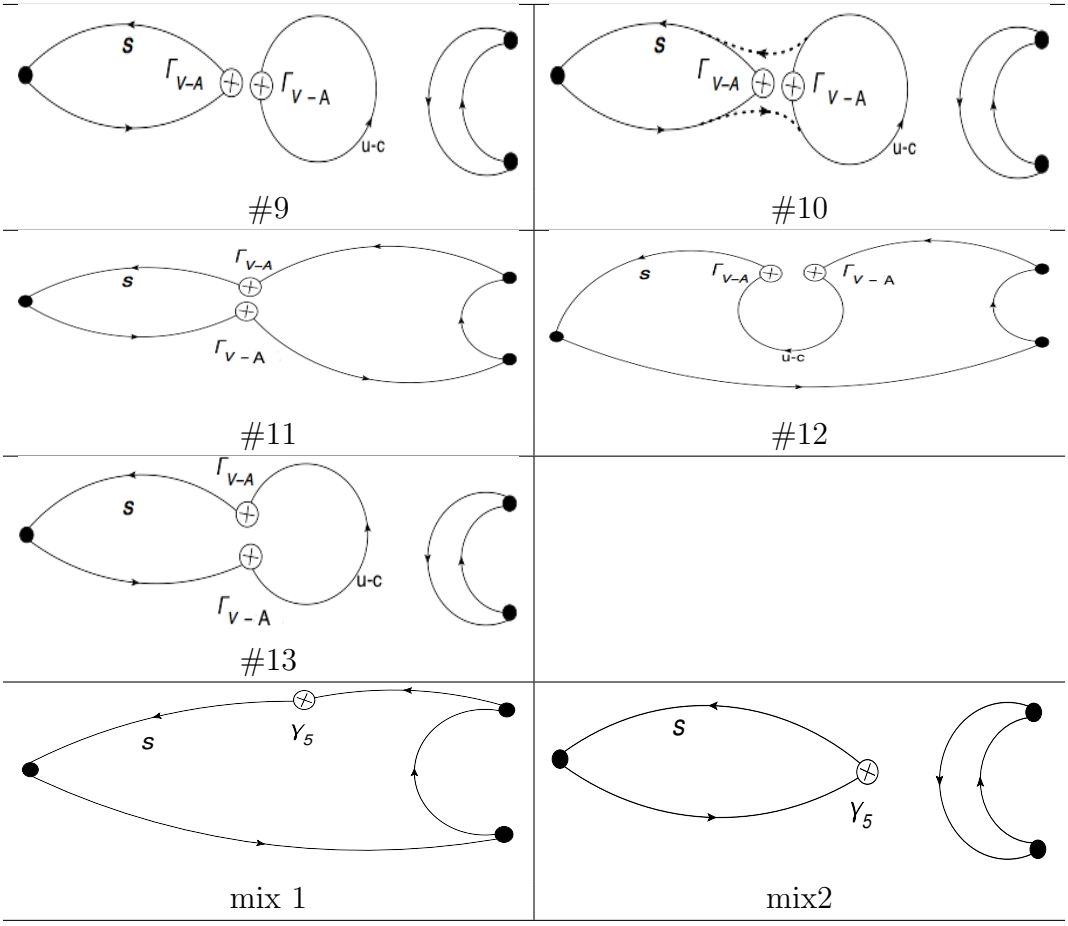

Figure A.13: Contractions for $K \to \pi\pi$ diagrams, continued. Only Q_1 and Q_2 are included. The vertex is a $V - A$ vertex.

A.4 All two point dagrams

The $\pi\pi$ scattering diagrams are not included here.

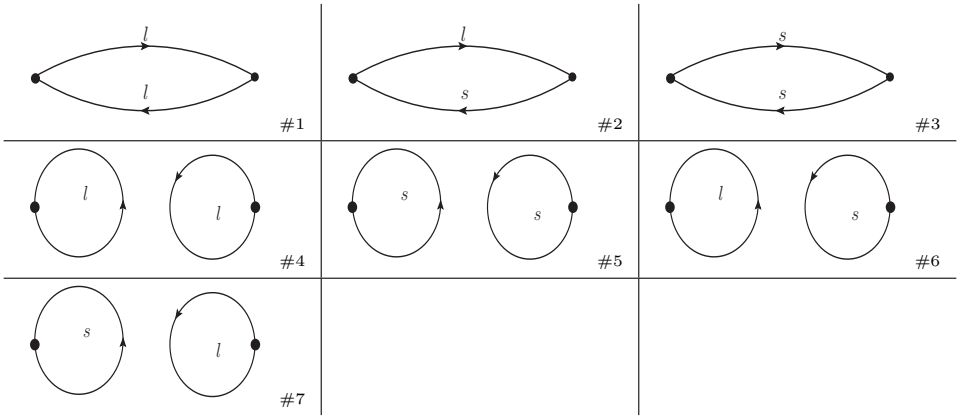

Figure A.14: 2 point diagrams

A.5 All $\pi\pi$ scattering diagrams

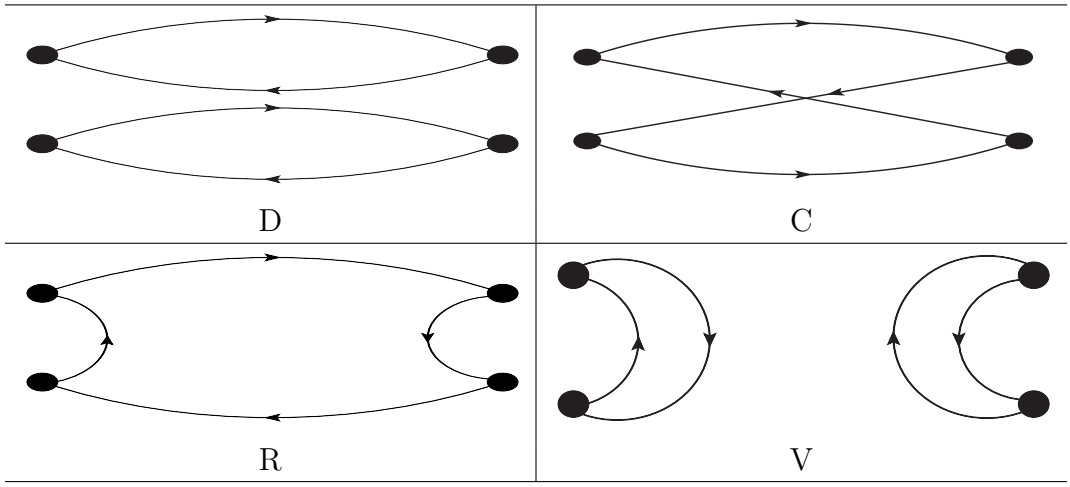

Figure A.15: $D(t)$,$C(t)$,$R(t)$,$V(t)$ for two pions

Appendix B

Contraction details

We list all the contractions we need to determine the meson masses, the matrix element and the final results from the Green functions we have calculated. We list all the diagrams in Chapter A, This chapter specifies how we combine those diagrams to find the quantity we want.

B.1 Two point contractions

The relevant diagrams are in A.4.

$$\langle \pi|\pi\rangle = [\#1] \tag{B.1}$$

$$\langle K^0|K^0\rangle = [\#2] \tag{B.2}$$

$$\langle \eta|\eta\rangle = \frac{1}{3}\left(2\times[\#1]+[\#3]-4\times[\#4]-[\#5]-2\times[\#6]-2\times[\#7]\right) \tag{B.3}$$

$$\langle \eta'|\eta'\rangle = \frac{1}{6}\left(2\times[\#1]+4\times[\#3]-4\times[\#4]-4\times[\#5]+4\times[\#6]+4\times[\#7]\right) \tag{B.4}$$

B.2 $\pi\pi$ scattering contractions

The relevant diagrams are in A.5.

$$\langle \pi\pi_{I=0} | \pi\pi_{I=0} \rangle = 2D + C - 6R + 3V \tag{B.5}$$

$$\langle \pi\pi_{I=2} | \pi\pi_{I=2} \rangle = 2D - 2C \tag{B.6}$$

B.3 Three point contractions

The relevant diagrams are in A.2. We first multiply all the 3 point diagrams that have an even number of loops by -1. The minus signs in the following equations are therefore not relevant for the number of loops, but come from the structure of the meson states.

$$\langle \pi | Q_1^{uu} | K^0 \rangle = \frac{1}{\sqrt{2}} \left([\#1] - [\#9] \right) \tag{B.7}$$

$$\langle \pi | Q_1^{cc} | K^0 \rangle = \frac{1}{\sqrt{2}} \left(-[\#13] \right) \tag{B.8}$$

$$\langle \pi | Q_2^{uu} | K^0 \rangle = \frac{1}{\sqrt{2}} \left([\#2] - [\#10] \right) \tag{B.9}$$

$$\langle \pi | Q_2^{cc} | K^0 \rangle = \frac{1}{\sqrt{2}} \left(-[\#14] \right). \tag{B.10}$$

Define the following quantities:

$$[K \to \pi]_u^L (1) = \frac{1}{\sqrt{2}} \left([\#1] - [\#9] \right) \tag{B.11}$$

$$[K \to \pi]_u^L (2) = \frac{1}{\sqrt{2}} \left([\#2] - [\#10] \right) \tag{B.12}$$

$$[K \to \pi]_c^L (1) = \frac{1}{\sqrt{2}} \left(-[\#13] \right) \tag{B.13}$$

$$[K \to \pi]_c^L (2) = \frac{1}{\sqrt{2}} \left(-[\#14] \right). \tag{B.14}$$

$$[K \to \pi]_d^L (1) = \frac{1}{\sqrt{2}} (-[\#1] - [\#5] - [\#9] - [\#15]) \tag{B.15}$$

$$[K \to \pi]_d^L (2) = \frac{1}{\sqrt{2}} (-[\#2] - [\#6] - [\#10] - [\#16]) \tag{B.16}$$

$$[K \to \pi]_s^L (1) = \frac{1}{\sqrt{2}} (-[\#11] - [\#17]) \tag{B.17}$$

$$[K \to \pi]_s^L (2) = \frac{1}{\sqrt{2}} (-[\#12] - [\#18]) . \tag{B.18}$$

$$[K \to \pi]_u^R (1) = \frac{1}{\sqrt{2}} ([\#66] - [\#74]) \tag{B.19}$$

$$[K \to \pi]_u^R (2) = \frac{1}{\sqrt{2}} ([\#67] - [\#75]) \tag{B.20}$$

$$[K \to \pi]_c^R (1) = \frac{1}{\sqrt{2}} (-[\#78]) \tag{B.21}$$

$$[K \to \pi]_c^R (2) = \frac{1}{\sqrt{2}} (-[\#79]) \tag{B.22}$$

$$[K \to \pi]_d^R (1) = \frac{1}{\sqrt{2}} (-[\#66] - [\#70] - [\#74] - [\#80]) \tag{B.23}$$

$$[K \to \pi]_d^R (2) = \frac{1}{\sqrt{2}} (-[\#67] - [\#71] - [\#75] - [\#81]) \tag{B.24}$$

$$[K \to \pi]_s^R (1) = \frac{1}{\sqrt{2}} (-[\#76] - [\#82]) \tag{B.25}$$

$$[K \to \pi]_s^R (2) = \frac{1}{\sqrt{2}} (-[\#77] - [\#83]) . \tag{B.26}$$

Using the above quantities, we find:

$$\langle\pi|Q_3|K^0\rangle = [K\to\pi]_u^L(1)+[K\to\pi]_d^L(1)+[K\to\pi]_c^L(1)+[K\to\pi]_s^L(1) \quad \text{(B.27)}$$

$$\langle\pi|Q_4|K^0\rangle = [K\to\pi]_u^L(2)+[K\to\pi]_d^L(2)+[K\to\pi]_c^L(2)+[K\to\pi]_s^L(2) \quad \text{(B.28)}$$

$$\langle\pi|Q_5|K^0\rangle = [K\to\pi]_u^R(1)+[K\to\pi]_d^R(1)+[K\to\pi]_c^R(1)+[K\to\pi]_s^R(1) \quad \text{(B.29)}$$

$$\langle\pi|Q_6|K^0\rangle = [K\to\pi]_u^R(2)+[K\to\pi]_d^R(2)+[K\to\pi]_c^R(2)+[K\to\pi]_s^R(2) \quad \text{(B.30)}$$

$$\langle\pi|\bar{s}d|K^0\rangle = -\frac{1}{\sqrt{2}}[\#59]. \quad \text{(B.31)}$$

Similarly, define the following quantities:

$$[K\to 0]_u^L(1) = ([\#49]) \quad \text{(B.32)}$$

$$[K\to 0]_u^L(2) = ([\#50]) \quad \text{(B.33)}$$

$$[K\to 0]_c^L(1) = ([\#53]) \quad \text{(B.34)}$$

$$[K\to 0]_c^L(2) = ([\#54]) \quad \text{(B.35)}$$

$$[K\to 0]_d^L(1) = ([\#49]+[\#55]) \quad \text{(B.36)}$$

$$[K\to 0]_d^L(2) = ([\#50]+[\#56]) \quad \text{(B.37)}$$

$$[K\to 0]_s^L(1) = ([\#51]+[\#57]) \quad \text{(B.38)}$$

$$[K\to 0]_s^L(2) = ([\#52]+[\#58])\,. \quad \text{(B.39)}$$

$$[K \to 0]_u^R (1) = ([\#114]) \tag{B.40}$$

$$[K \to 0]_u^R (2) = ([\#115]) \tag{B.41}$$

$$[K \to 0]_c^R (1) = ([\#118]) \tag{B.42}$$

$$[K \to 0]_c^R (2) = ([\#119]) \tag{B.43}$$

$$[K \to 0]_d^R (1) = ([\#114] + [\#120]) \tag{B.44}$$

$$[K \to 0]_d^R (2) = ([\#115] + [\#121]) \tag{B.45}$$

$$[K \to 0]_s^R (1) = ([\#116] + [\#122]) \tag{B.46}$$

$$[K \to 0]_s^R (2) = ([\#117] + [\#123]) \,. \tag{B.47}$$

Using the above quantities, we find:

$$\langle 0|Q_1^{uu}|K^0\rangle = [K \to 0]_u^L (1) \tag{B.48}$$

$$\langle 0|Q_1^{cc}|K^0\rangle = [K \to 0]_c^L (1) \tag{B.49}$$

$$\langle 0|Q_2^{uu}|K^0\rangle = [K \to 0]_u^L (2) \tag{B.50}$$

$$\langle 0|Q_2^{cc}|K^0\rangle = [K \to 0]_c^L (2) \tag{B.51}$$

$$\langle 0|Q_3|K^0\rangle = [K \to 0]_u^L (1) + [K \to 0]_d^L (1) + [K \to 0]_c^L (1) + [K \to 0]_s^L (1) \tag{B.52}$$

$$\langle 0|Q_4|K^0\rangle = [K \to 0]_u^L (2) + [K \to 0]_d^L (2) + [K \to 0]_c^L (2) + [K \to 0]_s^L (2) \tag{B.53}$$

$$\langle 0|Q_5|K^0\rangle = [K \to 0]_u^R (1) + [K \to 0]_d^R (1) + [K \to 0]_c^R (1) + [K \to 0]_s^R (1) \tag{B.54}$$

$$\langle 0|Q_6|K^0\rangle = [K \to 0]_u^R (2) + [K \to 0]_d^R (2) + [K \to 0]_c^R (2) + [K \to 0]_s^R (2) \tag{B.55}$$

$$\langle 0|\bar{s}\gamma_5 d|K^0\rangle = [\#63]. \tag{B.56}$$

To find the kaon to η matrix element, define the following quantities:

$$[K \to \eta]_u^L(1) = \frac{1}{\sqrt{6}}([\#1] + [\#29] + [\#9] + [\#29] - 2 \times [\#19] - 2 \times [\#39]) \quad \text{(B.57)}$$

$$[K \to \eta]_u^L(2) = \frac{1}{\sqrt{6}}([\#2] + [\#30] + [\#10] + [\#30] - 2 \times [\#20] - 2 \times [\#40]) \quad \text{(B.58)}$$

$$[K \to \eta]_c^L(1) = \frac{1}{\sqrt{6}}([\#33] + [\#13] + [\#33] - 2 \times [\#23] - 2 \times [\#43]) \quad \text{(B.59)}$$

$$[K \to \eta]_c^L(2) = \frac{1}{\sqrt{6}}([\#34] + [\#14] + [\#34] - 2 \times [\#24] - 2 \times [\#44]) \quad \text{(B.60)}$$

$$\begin{aligned}[K \to \eta]_d^L(1) = \frac{1}{\sqrt{6}}&(2 \times [\#29] + 2 \times [\#35] + [\#9] + [\#15] + [\#1] + [\#5] \\ &-2 \times [\#19] - 2 \times [\#25] - 2 \times [\#39] - 2 \times [\#45])\end{aligned} \quad \text{(B.61)}$$

$$\begin{aligned}[K \to \eta]_d^L(2) = \frac{1}{\sqrt{6}}&(2 \times [\#30] + 2 \times [\#36] + [\#10] + [\#16] + 2 + [\#6] \\ &-2 \times [\#20] - 2 \times [\#26] - 2 \times [\#40] - 2 \times [\#46])\end{aligned} \quad \text{(B.62)}$$

$$\begin{aligned}[K \to \eta]_s^L(1) = \frac{1}{\sqrt{6}}&(2 \times [\#31] + 2 \times [\#37] + [\#11] + [\#17] \\ &-2 \times [\#21] - 2 \times [\#27] - 2 \times [\#3] - 2 \times [\#7] - 2 \times [\#41] - 2 \times [\#47])\end{aligned} \quad \text{(B.63)}$$

$$\begin{aligned}[K \to \eta]_s^L(2) = \frac{1}{\sqrt{6}}&(2 \times \#32 + 2 \times \#38 + \#12 + \#18 \\ &-2 \times \#22 - 2 \times \#28 - 2 \times \#4 - 2 \times \#8 - 2 \times \#42 - 2 \times \#48)\,.\end{aligned} \quad \text{(B.64)}$$

$$[K \to \eta]_u^R(1) = \frac{1}{\sqrt{6}}([\#66] + [\#94] + [\#74] + [\#94] - 2 \times [\#84] - 2 \times [\#104]) \quad \text{(B.65)}$$

$$[K \to \eta]_u^R(2) = \frac{1}{\sqrt{6}}([\#67] + [\#95] + [\#75] + [\#95] - 2 \times [\#85] - 2 \times [\#105]) \quad \text{(B.66)}$$

$$[K \to \eta]_c^R(1) = \frac{1}{\sqrt{6}}([\#98] + [\#78] + [\#98] - 2 \times [\#88] - 2 \times [\#108]) \quad \text{(B.67)}$$

$$[K \to \eta]_c^R(2) = \frac{1}{\sqrt{6}}([\#99] + [\#79] + [\#99] - 2 \times [\#89] - 2 \times [\#109]) \quad \text{(B.68)}$$

$$[K \to \eta]_d^R(1) = \frac{1}{\sqrt{6}}(2 \times [\#94] + 2 \times [\#100] + [\#74] + [\#80] + [\#66] + [\#70] \quad \text{(B.69)}$$
$$-2 \times [\#84] - 2 \times [\#90] - 2 \times [\#104] - 2 \times [\#110])$$

$$[K \to \eta]_d^R(2) = \frac{1}{\sqrt{6}}([\#95] + [\#101] + [\#75] + [\#81] + [\#67] + [\#71] + [\#95] + [\#101] \quad \text{(B.70)}$$
$$-2 \times [\#85] - 2 \times [\#91] - 2 \times [\#105] - 2 \times [\#111])$$

$$[K \to \eta]_s^R(1) = \frac{1}{\sqrt{6}}([\#96] + [\#102] + [\#76] + [\#82] + [\#96] + [\#102] \quad \text{(B.71)}$$
$$-2 \times [\#86] - 2 \times [\#92] - 2 \times [\#68] - 2 \times [\#72] - 2 \times [\#106] - 2 \times [\#112])$$

$$[K \to \eta]_s^R(2) = \frac{1}{\sqrt{6}}([\#97] + [\#103] + [\#77] + [\#83] + [\#97] + [\#103] \quad \text{(B.72)}$$
$$-2 \times [\#87] - 2 \times [\#93] - 2 \times [\#69] - 2 \times [\#73] - 2 \times [\#107] - 2 \times [\#113])\,.$$

Using the above quantities, we find:

$$\langle\eta|Q_1^{uu}|K^0\rangle = [K\to\eta]_u^L(1) \tag{B.73}$$

$$\langle\eta|Q_1^{cc}|K^0\rangle = [K\to\eta]_c^L(1) \tag{B.74}$$

$$\langle\eta|Q_2^{uu}|K^0\rangle = [K\to\eta]_u^L(2) \tag{B.75}$$

$$\langle\eta|Q_2^{cc}|K^0\rangle = [K\to\eta]_c^L(2) \tag{B.76}$$

$$\langle\eta|Q_3|K^0\rangle = [K\to\eta]_u^L(1)+[K\to\eta]_d^L(1)+[K\to\eta]_c^L(1)+[K\to\eta]_s^L(1) \tag{B.77}$$

$$\langle\eta|Q_4|K^0\rangle = [K\to\eta]_u^L(2)+[K\to\eta]_d^L(2)+[K\to\eta]_c^L(2)+[K\to\eta]_s^L(2) \tag{B.78}$$

$$\langle\eta|Q_5|K^0\rangle = [K\to\eta]_u^R(1)+[K\to\eta]_d^R(1)+[K\to\eta]_c^R(1)+[K\to\eta]_s^R(1) \tag{B.79}$$

$$\langle\eta|Q_6|K^0\rangle = [K\to\eta]_u^R(2)+[K\to\eta]_d^R(2)+[K\to\eta]_c^R(2)+[K\to\eta]_s^R(2) \tag{B.80}$$

$$\langle\eta|\bar{s}d|K^0\rangle = \frac{1}{\sqrt{6}}(59-2\times60+2\times61-2\times62). \tag{B.81}$$

B.4 $K\to\pi\pi$ contractions

All the relevant diagrams are in Section A.3. We have only shown the Q_1 and Q_2 operators. The operator with cc does not contribute to the I=2 amplitude. For the $I=0$ amplitude, since the operators always appear in the form of $Q^{uu}-Q^{cc}$ for the ΔM_K calculation, we use the combination $u-c$ in the self-loop in all the diagrams, calculating the matrix element for the difference $Q^{uu}-Q^{cc}$. This is not the case for the ϵ_K calculation. However, in the ϵ_K calculation, we used a lattice with heavy pions, so we do not need to calculate the $K\to\pi\pi$ since the $\pi\pi$ states are heavier than the kaon.

$$\langle \pi\pi_{i=2}|Q_1^{uu}|K^0\rangle = \sqrt{\frac{2}{3}}\left([\#1]-[\#3]\right) \tag{B.82}$$

$$\langle \pi\pi_{I=2}|Q_2^{uu}|K^0\rangle = \sqrt{\frac{2}{3}}\left([\#2]-[\#4]\right) = \sqrt{\frac{2}{3}}\left(\#1-\#3\right) \tag{B.83}$$

$$\langle \pi\pi_{i=0}|(Q_1^{uu}-Q_1^{cc})|K^0\rangle = \sqrt{\frac{1}{3}}\left(-[\#1]-2\times[\#4]+3\times[\#5]+3\times[\#7]-3\times[\#9]\right) \tag{B.84}$$

$$\begin{aligned}\langle \pi\pi_{i=0}|(Q_1^{uu}-Q_1^{cc})|K^0\rangle &= \sqrt{\frac{1}{3}}\left(-[\#2]-2\times[\#4]+3\times[\#6]+3\times[\#8]-3\times[\#10]\right) \\ &= \sqrt{\frac{1}{3}}\left([\#3]+2\times[\#1]-3\times[\#11]-3\times[\#12]+3\times[\#13]\right)\end{aligned} \tag{B.85}$$

$$\langle \pi\pi_{i=0}|\bar{s}d|K^0\rangle = \sqrt{\frac{1}{3}}\left(3\times mix2-3\times mix1\right) \tag{B.86}$$

B.5 Four point contractions

We list the contractions for the ΔM_K calculation and the ϵ_K calculation separately, since the structure of H_W is different. The relevant diagrams are in A.1. We use the function $addtp12(a,b,c,d)$ to denote adding the type 1&2 diagrams with the numbers a,b,c,d. If a number appears twice, that means a factor of 2 should be introduced, and if a number is negative, that means that term is multiplied by -1. We define the function $addtp34(a,b,c,d)$ for type 3&4 diagram and $addtp5(a,b,c,d)$ for type 5 diagram.

B.5.1 ΔM_K contractions

In the calculation of the ΔM_K, we have only the Q_1 and Q_2 operators, and all the internal quark lines have a structure $u-c$. We first multiply all the diagrams with an even number

of loops by a -1, then we have (there is a common factor of 2 which we we have not shown):

$$\begin{aligned}
\langle \bar{K}^0|Q_1Q_1|K^0\rangle &= addtp12(1,-2,-3,4) + addtp12(17,-18,-19,20) \qquad \text{(B.87)}\\
&\quad + addtp34(1,-2) + addtp34(21,-22)\\
\langle \bar{K}^0|Q_1Q_2|K^0\rangle &= addtp12(13,-14,-15,16) + addtp12(29,-30,-31,32) \qquad \text{(B.88)}\\
&\quad + addtp34(16,-17) + addtp34(36,-37)\\
\langle \bar{K}^0|Q_2Q_1|K^0\rangle &= addtp12(9,-10,-11,12) + addtp12(25,-26,-27,28) \qquad \text{(B.89)}\\
&\quad + addtp34(11,-12) + addtp34(31,-32)\\
\langle \bar{K}^0|Q_2Q_2|K^0\rangle &= addtp12(5,-6,-7,8) + addtp12(21,-22,-23,24) \qquad \text{(B.90)}\\
&\quad + addtp34(6,-7) + addtp34(26,-27)
\end{aligned}$$

$$\begin{aligned}
\langle \bar{K}^0|\bar{s}dQ_1|K^0\rangle &= addtp34(41,-42) + addtp34(52,-53) \qquad \text{(B.91)}\\
\langle \bar{K}^0|\bar{s}dQ_2|K^0\rangle &= addtp34(46,-47) + addtp34(57,-58) \qquad \text{(B.92)}\\
\langle \bar{K}^0|\bar{s}d\bar{s}d|K^0\rangle &= addtp34(51,62). \qquad \text{(B.93)}
\end{aligned}$$

B.5.2 ϵ_K contractions

We first multiply all the diagrams with an even number of loops by a -1, then we have (there is a common factor of 2 which we have not shown):

$$\begin{aligned}
\langle \bar{K}^0 | Q_1 Q_1 | K^0 \rangle &= addtp12(-2,-3,4,4,-18,-19,20,20) \qquad \text{(B.94)} \\
&\quad + addtp34(-2,-2,-22,-22) \\
\langle \bar{K}^0 | Q_1 Q_2 | K^0 \rangle &= addtp12(-14,-15,16,16,-10,-11,12,12) \qquad \text{(B.95)} \\
&\quad + addtp12(-30,-31,32,32,-26,-27,28,28) \\
&\quad + addtp34(-17,-12,-17,-12,-32,-37,-32,-37) \\
\langle \bar{K}^0 | Q_2 Q_2 | K^0 \rangle &= addtp12(-6,-7,8,8,-22,-23,24,24) \qquad \text{(B.96)} \\
&\quad + addtp34(-7,-7,-27,-27)
\end{aligned}$$

$$\langle \bar{K}^0|Q_1Q_3|K^0\rangle = 2*addtp12(-1,4,-17,20) - 2*addtp34(1,1,2,3,4,5) \quad \text{(B.97)}$$
$$-2*addtp34(21,21,22,23,24,25) - 2*addtp5(1,5,9,13)$$

$$\langle \bar{K}^0|Q_1Q_4|K^0\rangle = 2*addtp12(-13,16,-29,32) - 2*addtp34(16,16,17,18,19,20) \quad \text{(B.98)}$$
$$-2*addtp34(36,36,37,38,39,40) - 2*addtp5(4,8,12,16)$$

$$\langle \bar{K}^0|Q_1Q_5|K^0\rangle = 2*addtp12(-33,36,-49,52) - 2*addtp34(63,63,64,65,66,67) \quad \text{(B.99)}$$
$$-2*addtp34(83,83,84,85,86,87) - 2*addtp5(25,29,33,37)$$

$$\langle \bar{K}^0|Q_1Q_6|K^0\rangle = 2*addtp12(-45,48,-61,64) - 2*addtp34(78,78,79,80,81,82) \quad \text{(B.100)}$$
$$-2*addtp34(98,98,99,100,101,102) - 2*addtp5(28,32,36,40)$$

$$\langle \bar{K}^0|Q_2Q_3|K^0\rangle = 2*addtp12(-9,12,-25,28) - 2*addtp34(11,11,12,13,14,15) \quad \text{(B.101)}$$
$$-2*addtp34(31,31,32,33,34,35) - 2*addtp5(3,7,11,15)$$

$$\langle \bar{K}^0|Q_2Q_4|K^0\rangle = 2*addtp12(-5,8,-21,24) - 2*addtp34(6,6,7,8,9,10) \quad \text{(B.102)}$$
$$-2*addtp34(26,26,27,28,29,30) - 2*addtp5(2,6,10,14)$$

$$\langle \bar{K}^0|Q_2Q_5|K^0\rangle = 2*addtp12(-41,44,-57,60) - 2*addtp34(73,73,74,75,76,77) \quad \text{(B.103)}$$
$$-2*addtp34(93,93,94,95,96,97) - 2*addtp5(27,31,35,39)$$

$$\langle \bar{K}^0|Q_2Q_6|K^0\rangle = 2*addtp12(-37,40,-53,56) - 2*addtp34(68,68,69,70,71,72) \quad \text{(B.104)}$$
$$-2*addtp34(88,88,89,90,91,92) - 2*addtp5(26,30,34,38).$$

Appendix C

Operator Mixing and the calculate the lattice Wilson coefficients with NPR

In this chapter we introduce the Non-Perturbative Renormalization that we used to find the lattice Wilson coefficients for our operators. In the first section, I give the introduction and basis of the process we used to perform the NPR, and give the result for the NPR for the 24^3 lattice we used to calculate ϵ_K. In the following sections, I give the results for the NPR on the 32^3 and 64^3 ensembles. We note that the operators in the ΔM_K calculation are a subset of the operators in the ϵ_K calculation. So we only introduce the procedure in the first section.

C.1 NPR for ϵ_K on the 24^3 lattice

We have introduced the method we use to perform the Non-perturbative Renormalization (NPR) to find the lattice Wilson coefficients for the $K_L - K_S$ mass difference calculation in [21]. In the case of the ΔM_K, we have only the two current-current operators, and the operators are defined in four flavor theory where we also have charm quark. For the calculation of ϵ_K, the NPR will be harder because we have to include all the QCD penguin

operators. The procedure is similar to what we have done in [4], with the difference that we are working with four flavor operators and we do not include the electroweak penguin operators. We define the intermediate RI/SMOM scheme as introduced in [35]. We impose the RI condition specified in [36] on our Landau gauge fixed, amputated Green functions with off-shell external momentum p_1 and p_2. The momentum satisfy that $p_1^2 = p_2^2 = (p_1 - p_2)^2 = \mu^2$. We have chosen to use $\mu = 2.15$ GeV, the same as our choice in [21]. We have four different RI/SMOM schemes, the (γ_μ, γ_μ) scheme, the $(\gamma_\mu, \not{q})$ scheme, the $(\not{q}, \not{q})$ scheme, and the $(\not{q}, \gamma_\mu)$ scheme. In this work, we use the (γ_μ, γ_μ) scheme and the $(\gamma_\mu, \not{q})$ scheme, where the first γ_μ indicates the projection operator we use to define the operator renormalization and the second γ_μ or $\not{q}$ indicates the projection operator we use in the wave function renormalization.

We first write down the weak Hamiltonian that changes strangeness by one (we define $\lambda_i = V_{i,s}^* V_{i,d}$):

$$H_W = \frac{G_F}{\sqrt{2}}\Big(\sum_{q,q'=u,c} V_{q',s}^* V_{q,d} \sum_{i=1,2} C_i Q_i^{q',q} - \lambda_t \sum_{i=3}^{6} C_i Q_i \Big). \tag{C.1}$$

The q and q' in the current-current operator $Q_{1,2}^{q',q}$ can be either the up quark or the charm quark, resulting in 4 different operators for both Q_1 and Q_2. We note that the Wilson coefficients $C_{1,2}$ will be independent of the choice of q and q', so these four operators will have the same Wilson coefficient.

We need to define our operator basis for the NPR. We first define $\tau = \lambda_t/\lambda_u$, and write our $\Delta S = 1$ weak Hamiltonian as follows:

$$\begin{aligned} H_W \;=\; & \frac{G_F}{\sqrt{2}} \Bigg\{ V_{u,s}^* V_{u,d} \left[(1-\tau) \sum_{i=1,2} z_i(\mu)(Q_i^{uu} - Q_i^{cc}) + \tau \sum_{i=1}^{6} v_i(\mu) Q_i \right] \\ & + V_{u,s}^* V_{c,d} \sum_{i=1,2} z_i Q_i^{u,c} + V_{c,s}^* V_{u,d} \sum_{i=1,2} z_i Q_i^{c,u} \Bigg\}. \end{aligned} \tag{C.2}$$

Here the Q_1 and Q_2 without super-scripts indicate Q_1^{uu} and Q_2^{uu}. The first term in Eq. C.2,

$Q_i^{uu} - Q_i^{cc}$, does not mix with the penguin operators $Q_{3,4,5,6}$ because of the GIM cancellation, and the third and forth term also do not mix with the penguin operator because of their flavor structure (either $Q_i^{u,c}$ or $Q_i^{u,c}$). As we claimed before, the Wilson coefficient for the current-current operators do not depend on the quark structure. So we have $z_1 = v_1$ and $z_2 = v_2$. More details about this statement can be found in [10]. In the following discussion, we use C_i, $(i = 1, 2, ..., 6)$ to denote the Wilson coefficients for all of these 6 operators. We only need to perform the operator renormalization on the operators which appear in the second term, and form a basis of six operators. After we perform the NPR calculation to find the lattice Wilson coefficients for these 6 operators, the lattice Wilson coefficients for the other current-current operators will be automatically known (same as C_1^{lat} and C_1^{lat}).

With our basis of 6 operators (Q_1^{uu}, Q_2^{uu}, Q_3, Q_4, Q_5, Q_6), we first transform the operators to the RI/SMOM scheme using the 6×6 mixing matrix $Z^{lat \to RI}$:

$$Q_k^{RI} = Z_{kj}^{lat \to RI} Q_j^{lat}. \tag{C.3}$$

Then we transform the RI operators to the $\overline{MS}$ scheme using a 6×6 matrix Δr obtained from our internal note [37]:

$$Q_i^{\overline{MS}} = (1 + \Delta r)_{ik}^{RI \to \overline{MS}} Q_k^{RI} \tag{C.4}$$

Finally, we can find the lattice Wilson coefficient by using:

$$C_i^{\overline{MS}} Q_i^{\overline{MS}} = C_i^{lat} Q_i^{lat}. \tag{C.5}$$

We have performed the NPR measurements on 100 configurations from the $16^3 \times 32$ Iwasaki ensemble which has the same lattice spacing as the ensemble we used in the ϵ_K measurement. In the (γ_μ, γ_μ) scheme, we found $Z_q^{\gamma_\mu} = 0.7404(4)$, and the mixing matrix $Z^{lat \to RI}$ is given in Eq. C.6. Using this mixing matrix, and $\Delta r^{RI \to \overline{MS}}$ for the (γ_μ, γ_μ) scheme, we can find the lattice Wilson coefficients given in Eq. C.7.

$$Z^{lat\to RI} = \begin{pmatrix} 0.505(0) & -0.050(0) & 0.004(2) & -0.003(2) & 0.001(2) & -0.003(1) \\ -0.050(0) & 0.505(0) & -0.003(1) & 0.010(1) & -0.003(1) & 0.008(1) \\ 0 & 0 & 0.514(8) & -0.043(7) & -0.001(9) & 0.006(5) \\ 0 & 0 & -0.056(6) & 0.540(5) & -0.008(6) & 0.027(4) \\ 0 & 0 & 0.002(7) & -0.006(6) & 0.537(8) & -0.089(5) \\ 0 & 0 & -0.012(3) & 0.033(3) & -0.040(3) & 0.410(2) \end{pmatrix} \tag{C.6}$$

$$C^{lat} = \begin{pmatrix} -0.202(0.000) & 0.588(0.000) & 0.012(0.001) & -0.024(0.001) & 0.009(0.001) & -0.027(0.001) \end{pmatrix} \tag{C.7}$$

In the $(\gamma_\mu, \not{q})$ scheme, we the $Z_q^{\not{q}} = 0.8016(3)$, and the mixing matrix $Z^{lat\to RI}$ given in Eq. C.8. Using this mixing matrix, and the $\Delta r^{RI\to\overline{MS}}$ for the $(\gamma_\mu, \not{q})$ scheme, we can find the lattice Wilson coefficients given in Eq. C.9. We can see there's about 10% discrepancy in the lattice Wilson coefficients from the two different schemes, and this will be part of our systematic error. We can overcome this discrepancy by performing the NPR calculation at a higher energy scale, so that the errors from our $RI \to \overline{MS}$ conversion and the perturbation theory evaluation of the $\overline{MS}$ Wilson coefficients can be better controlled. This can be achieved either by using a finer lattice for our measurements or by using step-scaling in the NPR calculation.

$$Z^{lat\to RI} = \begin{pmatrix} 0.592(0) & -0.059(0) & 0.004(2) & -0.004(2) & 0.001(2) & -0.003(1) \\ -0.059(0) & 0.592(0) & -0.004(1) & 0.012(1) & -0.003(1) & 0.010(1) \\ 0 & 0 & 0.603(10) & -0.051(8) & -0.002(10) & 0.007(6) \\ 0 & 0 & -0.065(7) & 0.633(6) & -0.010(7) & 0.032(5) \\ 0 & 0 & 0.003(9) & -0.008(7) & 0.629(10) & -0.104(6) \\ 0 & 0 & -0.014(3) & 0.039(3) & -0.047(4) & 0.481(3) \end{pmatrix} \tag{C.8}$$

$$C^{lat} = \Big(-0.222(0.000) \quad 0.645(0.000) \quad 0.013(0.001) \quad -0.027(0.001) \quad 0.010(0.001) \quad -0.030(0.001)\Big) \tag{C.9}$$

C.2 NPR on the 64^3 lattice

We used a smaller lattice ($32^3 \times 64$) to perform this calculation. This smaller ensemble is generated using the same bare coupling but with a heavier than physical light quark and with Shamir rather than Mobius DWF action. The difference in the light quark masses should lead to a negligible error associated with our substitution of this $32^3 \times 64$ ensemble because the NPR calculation is performed at large momenta. However, the difference between the Shamir and Mobius actions may lead to as much as 1% difference between the renormalization factors computed on the $32^3 \times 64$ ensemble and those appropriate for the $64^3 \times 128$ ensemble being used to compute ΔM_K. (Here 1% was the difference in lattice spacings found between these two, nearly identical ensembles [25].)

We are only interested in the current-current operators, so the NPR results have very small statistical errors. We used 3 configurations. The details about these two ensemble can be found in [25]. The lattice momenta we used are:

$$p_1 = (4, 4, 0, 0) \tag{C.10}$$

$$p_2 = (0, 4, 4, 0) \tag{C.11}$$

These momenta correspond to an energy scale 2.64 GeV.

We calculated the value of Z_V and obtained $Z_V = 0.784$. This is actually about 1% different from the value 0.777 in [25]. We also alculate Z_q using the γ_μ scheme and found:

$$Z_q = 0.8136 \tag{C.12}$$

Using this value for Z_q, we found the 2×2 $lat \to RI$ mixing matrix in the (γ_μ, γ_μ) scheme:

$$Z^{lat \to RI} = \begin{pmatrix} 0.6266 & -0.0437 \\ -0.0437 & 0.6266 \end{pmatrix} \tag{C.13}$$

The $RI \to \overline{MS}$ mixing matrix ΔR is given as follow:

$$Z^{lat \to RI} = 10^{-3} \times \begin{pmatrix} -2.28 & 6.85 \\ 6.85 & -2.28 \end{pmatrix} \tag{C.14}$$

Using similar method as in the previous section, we find the $\overline{MS}$ Wilson coefficients:

$$C^{\overline{MS}} = \begin{pmatrix} -0.260 & 1.118 \end{pmatrix} \tag{C.15}$$

Finally, the lattice Wilson coefficients are:

$$C^{lat} = \begin{pmatrix} -0.206 & 0.709 \end{pmatrix} \tag{C.16}$$

C.3 NPR on the 32^3 DSDR lattice

Since this is a coarse lattice with a small inverse lattice spacing 1.38 GeV, we might have large discretization errors if we try to use a high energy scale in the NPR calculation, while a small scale might introduce large systematic errors from perturbation theory. We therefore use step scaling: first we match the lattice operator to RI/SMOM at 1.5 GeV, then we use a finer intermediate lattice (1/a=2.38 GeV) and do the same calculation at both 1.5 GeV and 3 GeV to get the step scaling function. Then with this step scaling function, we can relate our operator on the coarse lattice to the RI/SMOM operator at 3 GeV. Using procedure similar to that in the previous chapters, we can finally relate our lattice operators to the $\overline{MS}$ operators at 3 GeV.

For the intermediate scheme, we used both the RI/SMOM$(\gamma_\mu, \not{q})$ and RI/SMOM(γ_μ, γ_μ) schemes [36] as our intermediate matching scheme. The final lattice Wilson coefficients should be indepen-

dent of the intermediate scheme, and their discrepancy can be viewed as the size of the systematic error from our lattice to continuum matching. The lattice coefficients obtained using these two intermediate schemes are shown in Table C.1. We have about a 5% discrepancy between the lattice Wilson coefficients, and this will introduce about a 10% systematic error in our final results for ΔM_K. We can potentially overcome this by working on a finer lattice which will reduce the lattice discretization effects and using step scaling to match at a higher scale to minimize the errors from perturbation theory.

$C_1^{\overline{MS}}$	$C_2^{\overline{MS}}$	$\Delta r_{11} = \Delta r_{22}$	$\Delta r_{12} = \Delta r_{21}$	$Z_{11} = Z_{22}$	$Z_{12} = Z_{21}$	C_1^{lat}	C_2^{lat}
-0.2394	1.1068	-0.0566	0.0065	0.5589	-0.0918	-0.2179	0.6027
-0.2394	1.1068	-0.0022	0.0065	0.5008	-0.0819	-0.2064	0.5713

Table C.1: The $\overline{MS}$ Wilson Coefficients, $RI/SMOM \to \overline{MS}$ matching matrix Δr, $lat \to RI$ matching matrix Z obtained using Z_q calculated in different schemes, and finally the lattice Wilson coefficient at the scale 3.0GeV. 1st row: $(\gamma_\mu, \not{q})$ scheme, 2nd row: (γ_μ, γ_μ). We do not show a statistical error because all are less than 1%.

Appendix D

Tests of the DWF formulation for heavy quarks

In this chapter, we presents some tests we have done using heavy quarks with the Domain Wall Fermion action. The main purpose of these tests is to understand if we can safely use our choice of charm quark mass m, without having to worry that ma may be too large, resulting in unphysical behavior for the DWF formulation we are using. These tests can also used as a measure for the systematic error coming from the charm quark.

D.1 Dispersion relations

The dispersion relation is defined as follows:

$$c^2 = \frac{E^2 - m^2}{p^2}. \tag{D.1}$$

We measure the energy of the D meson. We give the charm quark a momentum while leaving the light quark at rest. We used wall source propagators for both of the two flavors and used a point sink in the contractions. To test the calculation on the 64^3 ensemble, we have calculated this dispersion relation on a 32^3 Iwasaki lattice instead, which has similar lattice spacing (2.38 GeV).

The result is plotted in Fig D.1. A similar plot is shown in Fig. D.2 for the 32^3 DSDR lattice with an inverse lattice spacing of 1.36 GeV. From these two plots, we can see the deviation of the dispersion relation from 1 is much more significant on the course lattice with a 1.36 GeV inverse lattice spacing. If we quote this deviation as our systematic error for the energy scale around the charm quark mass ~ 1.3 GeV and our input lattice charm quark mass ~ 0.32, we will quote a 10% for the fine lattice and a 25% percent for the course lattice.

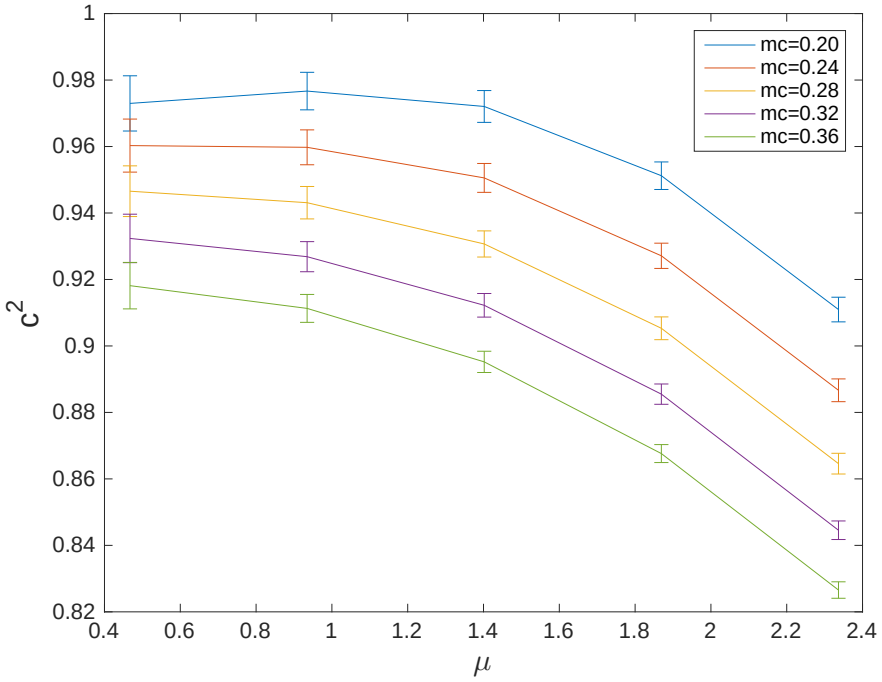

Figure D.1: The dispersion relation for different charm quark masses and momenta. The x axis is the energy scale of the momenta p.This calculation is performed on the 32^3 Iwasaki lattice with $1/a = 2.38$ GeV. 10 gauge configurations are used.

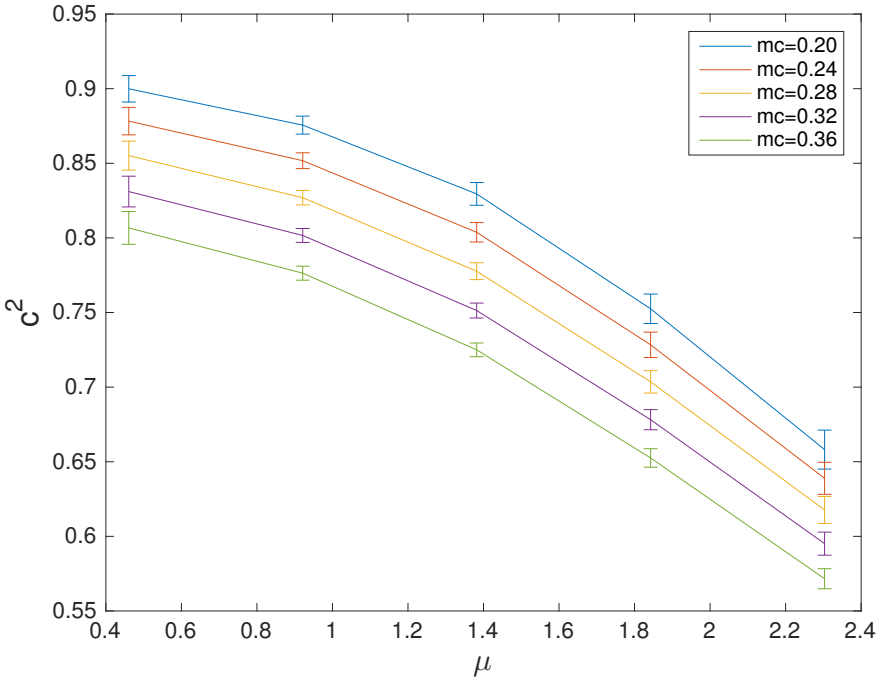

Figure D.2: The dispersion relation for different charm quark masses and momenta. The x axis is the energy scale of the momenta p. This calculation is performed on the 32^3 DSDR lattice with $1/a = 1.36$ GeV. 13 gauge configurations are used.

D.2 Charmed meson masses

In this section, we use the two point function constructed using wall-source point-sink propagators to study the masses of charmed mesons D_s and η_c. We use the $32^3 \times 64$ ensemble with an inverse lattice spacing of 2.38 GeV, very close to the one we used for the physical ΔM_K calculation. We used charm quark masses with lattice values from 0.2 to 0.76 seperated by 0.04, and we also included a point corresponding to the light quark(the D_s will then be the kaon and the η_c will be the pion).

In the following two plots, we show the m_{η_c} and m_{D_s}.

We are especially interested in the point that $m_c = 0.32$, which corresponds to our choice of the physical charm quark mass. We can see this point produces the physical value for the D_s mass and the η_c mass within less than a 5% difference. Here we used the physical value of the D_s mass of 1.96 GeV and physical η_c mass of 2.98 GeV.

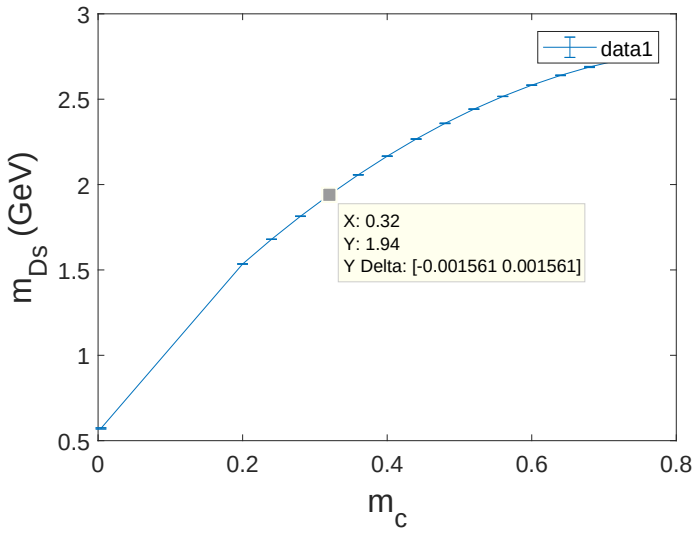

Figure D.3: Results for m_{D_s} for different values of m_c. 18 configurations were used. The first point corresponds to the kaon.

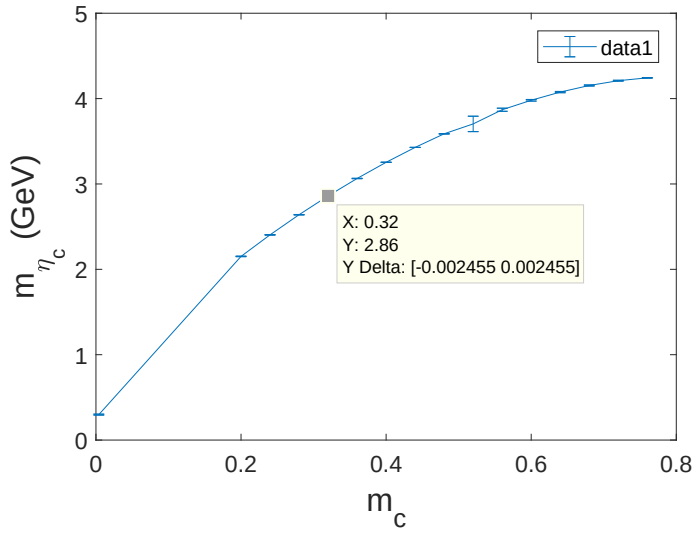

Figure D.4: Results for m_{η_c} for different m_c. 18 configurations were used. The first point corresponds to the pion and we note the pion is unphysically heavy on this ensemble.

D.3 Pseudo-scalar decay constant

We determine the pseudo-scalar decay constant by measuring the wall-source wall-sink two-point correlator and the wall-source point-sink correlator. Using the example of the D_s meson, we can then perform the following fitting which gives us the meson mass, the wall source normalization factor N_W and the matrix element $\langle 0|\bar{c}\gamma_5 s|D_s\rangle$:

$$C^{WW} = \frac{Z^W Z^W}{2m}(e^{-mt} + e^{-m(T-t)}) \tag{D.2}$$

$$C^{WP} = \frac{Z^W \langle 0|\bar{c}\gamma_5 s|D_s\rangle}{2m}(e^{-mt} + e^{-m(T-t)}). \tag{D.3}$$

The pseudo-scalar decay constant can be found using the following formula:

$$f_{D_s} = \frac{\langle 0|\bar{c}\gamma_5 s|D_s\rangle}{m^2\sqrt{V}}(m_s + m_c). \tag{D.4}$$

We work on the $32^3 \times 64$ lattice, with $1/a = 2.38$ GeV. $m_s = 0.03$ and $m_l = 0.004$.

In the following plot, we show the result for f_{D_s} for different values of m_c. The lowest value corresponds to the light quark (kaon).

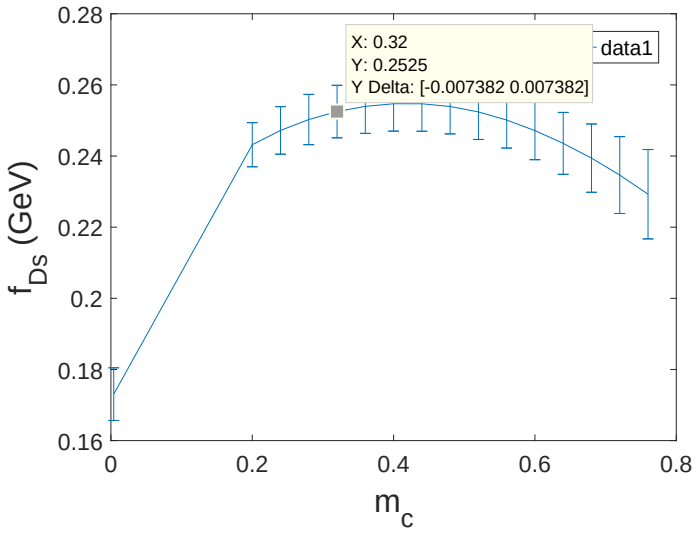

Figure D.5: Results for f_{D_s} for different values of m_c. The first point correspond to the kaon. 18 configurations were used.

We are especially interested in the point $m_c = 0.32$, which corresponds to the physical charm quark mass in our calculation. We can see this produce a $f_{D_s} = 0.252$ GeV, which is within 3% of the experimental value. The experimental value can be found using[38]:

$$|V_{cs}| f_{D_s} = 0.2509(4) \text{ GeV}$$

Using $|V_{cs}| = 0.973$, we find the experimental value to be 0.258 GeV.

In the following plot, we show the quantity $\Phi = f_{D_s} \times \sqrt{m}$ for different values of m_c. For the horizontal axis, we use $1/m_{\eta_c}$. This corresponds to the Figure 7 in [38], where a different method to find the pseudo-scalar decay constant was used.

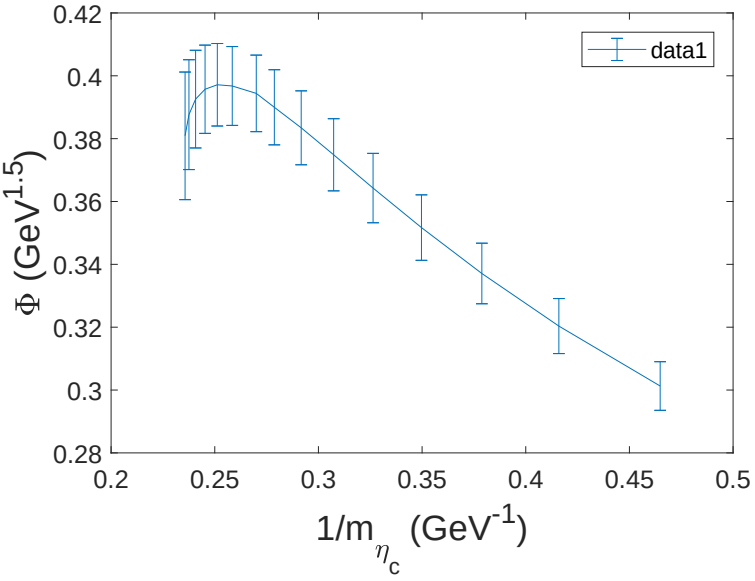

Figure D.6: Φ for different m_c. 18 configuration was used. Note physical, monotonic dependence on $\frac{1}{m_{\eta_c}}$ is seen in the vicinity of the physical value for $\frac{1}{m_{\eta_c}} = 0.336$.